Terahertz Near-Field Microscopy on Resonant Structures and Thin Films

Terahertz Near-Field Microscopy on Resonant Structures and Thin Films

Stan E.T. ter Huurne

The cover shows a measurement of the local density of optical states as a function of frequency and distance from a planar interface made of gold, normalized to a position far away from the interface.

A catalogue record is available from the Eindhoven University of Technology Library.
ISBN 978-90-386-5730-1.
A digital version of this thesis can be downloaded from surfacephotonics.org

Terahertz Near-Field Microscopy on Resonant Structures and Thin Films

PROEFSCHRIFT

ter verkrijging van de graad van doctor aan de Technische Universiteit Eindhoven, op gezag van de rector magnificus prof.dr. S.K. Lenaerts, voor een commissie aangewezen door het College voor Promoties, in het openbaar te verdedigen op 24 mei 2023 om 13:30 uur

door

Stan Erik Theodoor ter Huurne

Geboren te Udenhout

voorzitter:	prof.dr. H.J.H. Clercx	
1^{e} promotor:	prof.dr. J. Gómez Rivas	
2^{e} promotor:	dr. J.L.M. van Mechelen	
leden:	prof.dr. L.D.A. Siebbeles	(Technische Universiteit Delft)
	prof.dr. H. Roskos	(Goethe University)
	prof.dr. M. Vitiello	(Scuola Normale Superiore)
	prof.dr. M. Matters-Kammerer	
	dr. K.J. Tielrooij	

Het onderzoek dat in dit proefschrift wordt beschreven is uitgevoerd in overeenstemming met de TU/e Gedragscode Wetenschapsbeoefening.

This work was supported by the Netherlands Organization for Scientific Research (NWO).

Contents

Chapter 1

Introduction

Terahertz near-field microscopy is a relatively new measurement technique with many potential applications. This thesis discusses experimental results on resonant structures and thin films obtained by a near-field terahertz microscope. In this chapter, the physics that is relevant throughout this thesis is briefly described. The chapter ends with an outline of the thesis.

1.1 Light: from a Historical Perspective

Light is one of the most studied research areas in the history of mankind. Even though it is a vital part of our life, the nature of light was very elusive and took centuries to understand. The earliest theories were developed in ancient Greece (5th century BC), Empedocles postulated that the human eye was made out of the four elements (fire, air, earth, and water) and a fire shone from the eye allowing for sight. Of course, this theory would not differentiate between day and night, so an interaction with the rays from a source like the sun was needed. This interpretation of vision, called extramission theory, dominated for 1000 years. Around 300 BC, Euclid studied the properties of light from a geometrical point of view and wrote *Optica*. In his work, he postulated that light travels in straight lines and described observations such as perspective and the rounding of objects at a distance. Continuation of the work done by Euclid led to the formulation of 'the principle of the shortest path' by Hero of Alexandria (1st century AD), who described the reflection from a smooth surface with an equal angle of incidence and angle of reflection, paving the way of ray optics. It took 1500 years for this formulation to be replaced by the 'principle of least time' by Fermat. Ptolemy extended on Hero's theory by describing the bending of light at interfaces, creating the first table of refraction. However, he was unable to formulate an equation to accurately describe his observations. It took until the end of the millennium when the Arabic scholar Ibn Sahl was able to mathematically describe the law of refraction (currently known as Snell's law), which he used for his work on curved mirrors and lenses [1, 2]. A few decades later Hasan Ibn al-Haytham (known as Alhazen in Europe) described experimental methods to determine reflection and refraction [3]. He was also the first to explain that vision is due to light that reflects from an object and passes to the eyes.

During the scientific revolution, several major contributions to the understanding of light were achieved. Johannes Kepler described the inverse-square law governing the intensity of light, the reflection of flat and curved mirrors, and concepts such as parallax. As well as the reinvention of the law of refraction by Snellius and Descartes and the law of reflection. Using a prism Newton demonstrated dispersion and showed that the color of light was not determined by an object, but was an inherent property of light. During this era two interpretations of the nature of light were introduced: particle and wave theory, respectively. The first was strongly supported by Newton who claimed that light consisted of particles of matter which were emitted omnidirectionally [4]. The 2nd, wave theory, was suggested by Huygens and proposes that light waves propagate through the *ether* like sound waves [5]. Due to Newton's status, particle theory was dominant until the start of the 19th century. During that time the main argument against wave theory was the observation that light propagates along a straight line and does not bend around corners, like regular waves. However, to explain diffraction a light particle had to create a localized wave due to an interaction with the *ether*.

In 1802, Young performed the famous double-slit experiment which conclusively demonstrated the wave nature of light [6]. Here, light propagates through two small slits, where diffraction occurs and two wavefronts are created. These wavefronts interfere with each other, creating an interference pattern behind the slits with maxima and

minima due to the difference in path length. From this experiment, Young also related color to wavelength and could approximate the wavelength of several colors of light. Fresnel extended the understanding of the wave nature of light by experimenting with diffraction [7]. The final obstacle of the wave theory of light was the explanation of polarization. It took several years until Fresnel and Young both realized independently that light had to be a transverse wave. This was proven by Fresnel by explaining the double refraction from birefringent materials [7].

It took several decades until a complete mathematical description of light was formulated. Faraday linked light to electromagnetism by noticing a rotation of polarization in the presence of a magnetic field along the direction of propagation [8]. Several years later he proposed that light was a high-frequency electromagnetic vibration. Maxwell, inspired by Faraday, discovered that electromagnetic waves travel through space with a constant speed, which was equal to the speed of light. In 1865, a full mathematical description of light was formulated by Maxwell using 20 equations [8, 9]. These were later synthesized by Heaviside into the well-known 4 Maxwell(-Heaviside) equations [10]

$$\nabla \cdot \mathbf{E} = \frac{\rho}{\epsilon_0}, \tag{1.1a}$$

$$\nabla \cdot \mathbf{B} = 0, \tag{1.1b}$$

$$\nabla \times \mathbf{E} = -\frac{\partial \mathbf{B}}{\partial t}, \tag{1.1c}$$

$$\nabla \times \mathbf{B} = \mu_0 \left(\mathbf{J} + \epsilon_0 \frac{\partial \mathbf{E}}{\partial t} \right), \tag{1.1d}$$

where $\mathbf{E}$ describes the electric field, ρ is the charge density, ϵ_0 is the vacuum permittivity, $\mathbf{B}$ describes the magnetic field, μ_0 is magnetic permeability and $\mathbf{J}$ is the current density. From which the wave equation of light in a vacuum can be deduced

$$\nabla^2 \mathbf{E} = \frac{1}{c^2} \frac{\partial^2 \mathbf{E}}{\partial t^2}, \tag{1.2a}$$

$$\nabla^2 \mathbf{B} = \frac{1}{c^2} \frac{\partial^2 \mathbf{B}}{\partial t^2}, \tag{1.2b}$$

with the speed of light $c = \sqrt{1/\mu_0 \epsilon_0} \approx 300.000$ km/s. Hertz confirmed the theory experimentally soon after by generating and detecting radio waves in a laboratory using an antenna [11]. He demonstrated that these waves behave identically to visible light, exhibiting properties such as reflection, refraction, diffraction, and interference. The experimental verification of this theory revolutionized the world. Not only was it discovered that visible light was just a small portion of the entire electromagnetic spectrum, but the usage of antennas to transmit and receive electromagnetic radiation set off the research area related to electromagnetism. Within a decade the first wireless telegraphy radio communications systems were operational. Since then, antennas for emission, detection, and manipulation of electromagnetic radiation with artificial structures had tremendous development. Nowadays, we can control electromagnetic radiation in

almost any desired form. The complete control of propagation direction, phase, and polarization allows for many possibilities, including spatial and temporal confinement. These artificial structures scale with the wavelength of radiation, therefore many antenna designs and techniques can be carried over, but only if the fabrication technique allows for it.

1.2 Electromagnetic Spectrum, Spectroscopy, and Terahertz Radiation

The use of prisms to disperse light has enabled the investigation of the visible spectrum, leading to the development of spectroscopy, the study of the interaction between electromagnetic waves and matter as a function of wavelength. By analyzing the "missing" wavelengths in the solar spectrum, known as Fraunhofer lines, researchers were able to make discoveries [12]. By replacing prisms with diffraction gratings, it was possible to significantly increase the spectral resolution and quantify the dispersed wavelengths. After James Clerk Maxwell proposed that visible light is a high-frequency electromagnetic wave, the study of light-matter interactions at different wavelengths was extended across the entire electromagnetic spectrum.

The interaction between electromagnetic radiation and matter varies depending on the wavelength of the radiation. At short wavelengths or high frequencies, radiation has a strong and ionizing interaction with matter, leading to applications in fields such as medicine, lithography, crystallography, and forensics. The near-infrared range (800 nm-2500 nm) has a wide range of applications, including agriculture and fiber-optic communication. At low frequencies or long wavelengths, radio waves (3 kHz-300 GHz) are found. The earth's lower atmosphere is mostly transparent to radio waves, making them useful for long-range communication.

1.2.1 Terahertz Radiation

The region in the electromagnetic spectrum with frequencies between 0.1 and 10 terahertz (THz) is called the THz frequency range. These frequencies correspond to photon energies between 0.4 and 40 meV, and free-space wavelengths between 30 and 3000 μm. THz frequencies are located between microwaves and infrared in the electromagnetic spectrum, as shown in Fig. 1.1. THz radiation is known for its unique ability to penetrate materials that are opaque to other types of electromagnetic radiation, such as infrared and visible light.

There are several interesting applications for spectroscopy in the THz frequency range. Many biomolecules and chemical compounds are generally transparent but have distinct spectral fingerprints in this frequency range. These fingerprints include rotations in molecules, vibrational modes in ionic crystals, intraband transitions in semiconductors, and Cooper pair energies in superconductors [13]. One of the key benefits of THz spectroscopy is its non-ionizing nature, unlike x-rays, making them much safer to use

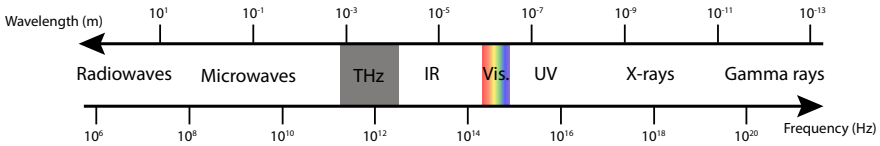

Figure 1.1: The electromagnetic spectrum showing the THz regime between microwaves and infrared frequencies.

on chemical compounds and living tissue and an ideal candidate for sensing and imaging [13–18]. Additionally, THz spectroscopy can be extremely sensitive, allowing for the detection of small changes in the properties of materials.

Despite many advantages and possibilities, THz spectroscopy is still relatively new and in full development. Due to the decrease in the power of high-frequency oscillators for the electrical generation of THz radiation and a lack of sufficiently low band gap semiconductors for the optical generation of THz, it has been a challenge to efficiently generate THz radiation [19–21]. Advancements in the development of ultrafast lasers have allowed for the development of new techniques to generate THz radiation, including THz time-domain spectroscopy (THz-TDS). Among the methods used for the generation and detection of THz radiation are photo-conductive antennas and optical rectification in combination with electro-optic sampling [13].

Measuring of THz pulses in the time domain allows for the determination of both amplitude and phase as a function of frequency, from these quantities the complex permittivity ($\tilde{\epsilon}(\omega)$) of the material under investigation can be directly determined. This capability has been particularly successful in studying semiconductors [22, 23], and has become a common method for examining novel materials such as graphene, nanowires, perovskites, and 2D semiconductors [24–27]. In THz spectroscopy, the electric field of the THz pulse interacts with the free charges in the material, including electrons and holes that can be intrinsically present in the material or are induced temporarily through photoexcitation or electrical biasing. In the study of these materials, the focus is on the interaction of THz waves with free charge carriers. Combining THz spectroscopy with well-known models has allowed for the study of the optoelectrical properties and quality of materials with free-charge carriers, like metals and semiconductors.

1.3 Drude Model

The conductance of a material is an important material property for electrical applications. In metals, the optical properties are dominated by how free electrons can move through the crystal structure. A simple, but surprisingly accurate, model was proposed by Drude in 1900 [28]. The Drude model assumes that the free electrons in the metal behave as a freely moving gas. The movement of the free electrons is randomized by collisions with other electrons and phonons or due to defects in the lattice. In between collisions, the charges can be accelerated in the presence of an externally applied electric field, resulting in an average displacement of electrons, i.e., a current **J**. This current is

proportional to the amplitude of the applied field **E** and the complex conductivity of the material $\tilde{\sigma}$ as $\mathbf{J} = \tilde{\sigma}\mathbf{E}$. In the presence of an AC electric field ($\mathbf{E}(t)=\mathbf{E}(\omega)e^{-i\omega t}$) the frequency-dependent complex conductivity can be approximated as

$$\tilde{\sigma}(\omega) = \frac{ne\mu_e}{1 - i\omega\tau}. \tag{1.3}$$

with n the carrier density, τ the scattering time, $\mu_e = e\tau/m^*$ the electron mobility and m^* the effective electron mass. These parameters are dependent on the intrinsic material properties and the quality of the material's structure. The conductivity scales linearly with the carrier density and the electron mobility, while the complex denominator scales with the time between collisions and the frequency. The frequency dependence of the conductivity can be divided into three regions. The first region is at low frequencies when $\omega\tau \ll 1$ the electrons can easily follow the oscillating electric field and the conductivity is equal to the DC value $\sigma_{DC} = ne\mu_e$. The third region is at high frequencies when $\omega\tau \gg 1$ and the oscillating field is too fast for the electrons to follow resulting in a vanishing conductance. The second region is at intermediate frequencies when $\omega\tau \sim 1$, here the conductance is frequency dependent, and the interaction of the field with the carriers is the largest. The influence of free electrons on the complex dielectric function is related to the conductivity of the material by the expression [29]

$$\tilde{\epsilon}(\omega) = \epsilon_\infty + \frac{i\tilde{\sigma}(\omega)}{\epsilon_0\omega}. \tag{1.4}$$

In the assumption that the electrons are delocalized and can propagate freely, they can be approximated as a plasma. A plasma can be driven by a coherent oscillation with the natural plasma frequency ω_p in bulk being equal to

$$\omega_p^2 = \frac{ne^2}{\epsilon_0 m^*}. \tag{1.5}$$

At frequencies larger than the plasma frequency, the dielectric function changes sign from negative to positive and the real part of the dielectric function drops to zero. For metals, the plasma frequency is usually in the ultraviolet region of the electromagnetic spectrum and the Drude model is quite accurate at lower frequencies. At THz frequencies, the imaginary component of the permittivity dominates, indicating a large conductance. Large Ohmic losses would be expected at these frequencies, however, this is not the case due to the large impedance difference between the metal and the surrounding medium. This results in low losses due to a slim skin depth

$$\delta(\omega) = 1/\alpha = \sqrt{\frac{2}{\omega\sigma\mu}}, \tag{1.6}$$

where μ is the permeability of the metal film. For gold, this is equal to a skin depth of $\lambda/6000$ at 0.5 THz, therefore the radiation does not penetrate metals thicker than this skin depth and absorption losses are minimal.

The Drude model is a good approximation to describe the influence of free electrons on the complex conductivity and the dielectric function. However, in many materials, the electrons cannot propagate freely for example due to boundary conditions. In the next section we will discuss two extensions of the Drude model, the Drude-Smith model which introduces a term that includes preferential backscattering at scattering events, and the Lorentz oscillator model which introduces a local resonance in the frequency range of interest.

1.3.1 Drude-Smith and Lorentz Oscillator Models

The Drude-Smith model is a phenomenological extension of the Drude model and was developed to describe materials where charge transport gets disrupted due to localization and disorder. The extension includes terms that describe scattering in preferential directions, in contrast with the Drude model where the scattering direction is randomized. The expression for the complex conductivity is given by [23, 25, 29]

$$\tilde{\sigma}_{DS}(\omega) = \frac{ne\mu_e}{1 - i\omega\tau_{DS}} \left[1 + \sum_{k=0}^{\infty} \frac{c_k}{(1 - i\omega\tau_{DS})^k} \right], \tag{1.7}$$

where τ_{DS} is the Drude-Smith scattering time and c_k is the fraction of the retained initial velocity after scattering events. When c_k is positive forward scattering is present, when c_k is negative there is backscattering, and when c_k is zero Eq. (1.7) reduces to the regular Drude expression given in Eq. (1.3). Usually, only the first term (k=1) is taken into consideration, assuming a single-scattering approximation. Generally, c_1 is negative and a preferential backscattering term is introduced due to, for example, boundaries or defects. The physical origin of the Drude-Smith model is not well justified [30], however, this model has yielded good agreements with measurements in thin films, nanowires, 2D materials, and perovskites [23, 25–27].

The second extension of the Drude model consists of adding a Lorentz oscillator to the conductivity, which describes a response at a finite frequency. The Lorentz oscillator model can be derived classically by solving the equation of motion of a damped harmonic oscillator. The origin of the resonant response can be rotations, vibrations, electronic transitions, phonons, magnons, etc. The Lorentz oscillator model can explain deviations from the Drude model due to these material resonances, and the complex conductivity is given by [31, 32]

$$\tilde{\sigma}_{DL}(\omega) = \frac{ne\mu_e}{1 - i\omega\tau_D} + \sum_{L=0}^{\infty} \frac{S_L\omega}{i(\omega_0^2 - \omega^2) + \omega\gamma_L}, \tag{1.8}$$

where S_L is the oscillator strength, ω_0 is the resonance frequency, and γ_L is the resonance linewidth. This model has shown good agreement with experiments in thin films, polymers, and 2D materials [31, 32].

1.4 Transition Metal Dichalcogenides

A type of material that has been investigated in this thesis using the Drude-Smith model is transition metal dichalcogenides (TMDs). TMDs are a class of materials that have attracted significant attention in the field of photonics due to their unique optical and electronic properties when reducing the dimensionality from bulk to two-dimensional (2D). TMDs are composed of a transition metal atom (such as Mo or W) sandwiched between two chalcogen atoms (such as S, Se, or Te) as shown in Fig. 1.2. They have a layered structure with strong in-plane covalent bonding and weak van der Waals interactions between the layers, which gives rise to their atomically thin nature and makes them highly flexible and tunable. Until the discovery of graphene, they were not widely studied. However, extensive research since then has led to the discovery of many novel phenomena in these materials. TMDs have several interesting optical properties that make them attractive for photonic applications. For example, they have a direct bandgap that can be tuned by changing the number of layers or the type of transition metal atom, which makes them suitable for optoelectronic devices such as photodetectors and lasers [33, 34]. Additionally, the lack of inversion center symmetry in monolayers and strong spin-orbit coupling results in a new degree of freedom in charge transport, known as valleytronics, which allows for the control of electron spin through the handedness of the excitation light [35, 36]. The quantum confinement of excitons in the monoatomic layer and the strong exciton binding energy lead to enhanced absorption and emission of light. 2D-TMDs have a large refractive index, which leads to strong optical confinement and strong light-matter interactions [37–41].

However, it can be challenging to prepare large, high-quality TMD monolayers. High crystal quality can be achieved by mechanically exfoliating the monolayers from a bulk crystal. However, the size is often limited to tens of microns and how this exfoliation is performed can significantly impact the quality of the resulting material [42]. In chapters 5 and 6 of this thesis, we use THz near-field microscopy to investigate TMD microcrystals prepared from the exfoliation of a bulk crystal.

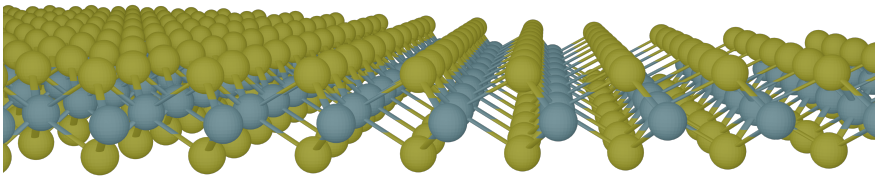

Figure 1.2: Crystal structure of a single atomic layer of a TMD.

1.5 Scattering

Light propagating through a medium can get scattered by perturbations in its path. The degree of perturbation depends on the scattering efficiency, which depends on properties like the shape, size, material, and orientation of the perturbations. Particularly efficient scatterers are small metallic structures, which confine free electrons in the volume determined by the geometry of the structure. These spatially confined free electrons can be driven resonantly by an electromagnetic wave, coupling the electrons and radiation, which forms a localized surface plasmon. The fundamental resonance in the motion of these electrons can be described qualitatively using the Lorentz harmonic oscillator model [43]. This model considers that the motion of electrons in a metallic particle can be driven with an electromagnetic field and will restore to equilibrium according to Hooke's law, with a resonance frequency $\omega_0 = \sqrt{D/m}$, where D and m are the elastic constant of the restoring force and the total effective mass of the electron cloud, respectively [43]. D can be estimated by assuming a cylindrical particle of length d and cross section A with an electron cloud displaced by Δx. This displacement creates a charge of $\pm q$ at both ends of the particle as shown in Fig. 1.3a. The resonance frequency ω_0 gives rise to the fundamental $\lambda/2$ and higher order resonances, these can occur with a resonance wavelength equal to $m\lambda + \lambda/2$, where m is an integer.

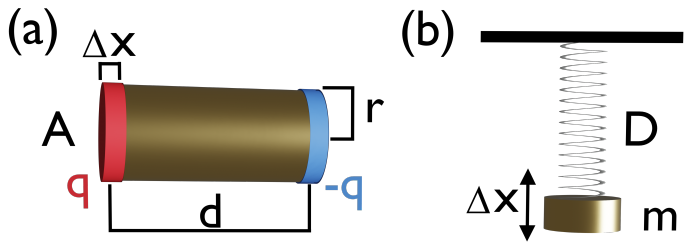

Figure 1.3: A Lorentz harmonic oscillator model. (a) Displacement of the electrons in a rod due to an external driving field is analogous to (b) a simple spring system with spring constant D, effective mass m, and displacement Δx.

The total charge is dependent on the carrier density n, cross-sectional area A, and the displacement Δx, and given as $q = neA\Delta x$. The restoring force can be determined as the derivative of the Coulomb potential energy

$$F(\Delta x) = -\frac{\mathrm{d}W(\Delta x)}{\mathrm{d}\Delta x} = -\frac{(ne)^2}{2\pi\epsilon_0}\frac{A^2}{d}\Delta x = -D\Delta x, \tag{1.9}$$

from which the elastic constant of the restoring force D is obtained. The mass of the electron cloud is given by $m = nm^* Ad$. Therefore, the resonance frequency is given by

$$\omega_0 = \sqrt{\frac{ne^2}{8\epsilon_0 m^*}}\frac{1}{R}, \tag{1.10}$$

where R is the aspect ratio of the particle, i.e., the ratio of the axis radius $d/2$ to the short axis radius r. Note that the resonance frequency of the Lorentz oscillator obtained with

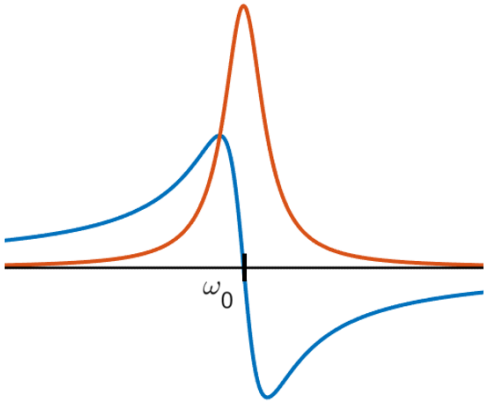

Figure 1.4: The dispersion of the real (blue curve) and imaginary (red curve) components of the polarizability of a particle using a Lorentz oscillator model near the resonance frequency ω_0.

this very simple model depends on the particle dimensions. The particle is polarized with a polarization vector proportional to the applied electric field, which can be determined from the equation of motion of the free electrons

$$\mathbf{P}_0 = \frac{q^2}{m^*} \frac{\mathbf{E}_0}{\omega_0^2 - \omega^2 - \mathrm{i}\gamma\omega} = \alpha \mathbf{E}_0, \tag{1.11}$$

where α is the polarizability of the particle, which describes its capability to get polarized by an external electric field. The polarizability of a particle near the resonance frequency is shown in Fig. 1.4 for the real and imaginary components. The real component of the polarizability becomes negative when the frequency is larger than the resonance frequency. Therefore, the polarization of the particle is out of phase with the incident field. The imaginary component defines the absorption in the particle and is maximum at the resonance frequency with a full width at half maximum equal to the damping rate, γ. This simple model illustrates that the desired resonance frequency can be achieved by shaping the particle appropriately.

However, the polarizability of a particle is more complicated than a simple Lorentz oscillator model. In an experiment, a particle is illuminated with a predetermined intensity after which the total power can be measured to determine the absorption and the scattering of the particle. The ratio between the transmitted power and incident intensity gives an 'extinction cross-section' while measuring only the power that is scattered by the particle gives a 'scattering cross-section' [44]. In the quasi-static limit, i.e., particles much smaller than the wavelength, the extinction and scattering cross sections of a metallic

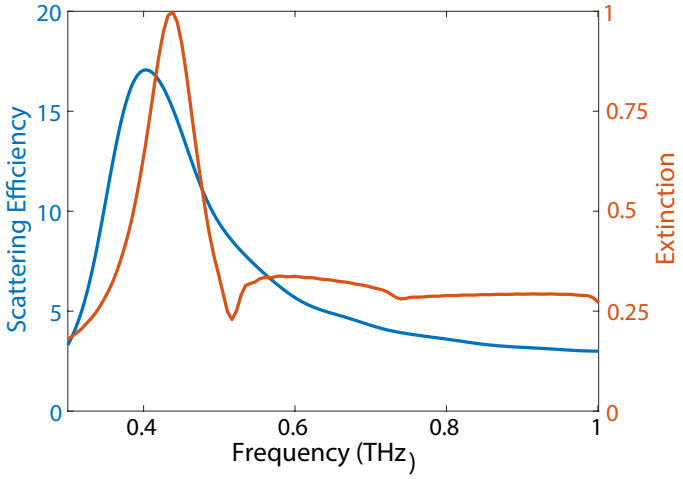

Figure 1.5: Simulated scattering efficiency of a 200×40 μm gold rod showing the $\lambda/2$ resonance near 0.4 THz and a high-frequency tail caused by the frequency dependence of the permittivity of gold (blue curve). Extinction spectrum of the same rod in a 300×300 μm square periodic array (red curve).

sphere are given by [44]

$$\sigma_{\text{ex}} = 4\pi k\, \mathbb{I}\text{m}[\alpha(\omega)], \tag{1.12a}$$

$$\sigma_{\text{sc}} = \frac{k^4}{6\pi\epsilon_0}|\alpha(\omega)|^2, \tag{1.12b}$$

where $k = 2\pi\sqrt{\epsilon_d}/\lambda$ is the wave vector of radiation outside of the particle. The difference between the scattering and extinction cross-sections is equal to the absorption cross-section. At THz frequencies, the scattering cross-section is considerably larger than the absorption cross-section, due to the slim skin depth caused by the large negative permittivity of the metal. Normalizing σ_{sc} to the geometrical cross-section gives the scattering efficiency Q_{sc}. The scattering efficiency can be simulated using a finite-difference time-domain method with a total field scattered field source and is shown for a gold rod of 200×40 μm on a quartz substrate as the blue curve in Fig. 1.5. The scattering efficiency becomes almost 17 times larger than the geometrical cross-section near the resonance of the rod, centered at 0.4 THz. The scattering of a single particle is already significant, however, the effect can be enhanced by coupling particles together and creating a coherent effect through lattice coupling, as will be discussed in the next section.

1.6 Rayleigh Anomalies and Surface Lattice Resonances

Rayleigh anomalies (RAs) are a phenomenon that occurs in periodic structures, such as photonic crystals and metamaterials. RAs were described for the first time by Wood

in 1902 and further analyzed by Rayleigh in 1907 [45–48]. They are characterized by their diffractive nature and narrow linewidth, making them interesting for applications in photonics such as waveguiding and enhanced light-matter interaction. The diffraction of radiation incident on a periodic array can be described by the conservation of the parallel component of the wave vector of the radiation relative to the surface of the array

$$\mathbf{k}_{\text{out},\parallel} = \mathbf{k}_{\text{in},\parallel} \pm \mathbf{G}, \tag{1.13}$$

where $\mathbf{k}_{\text{in},\parallel}$ and $\mathbf{k}_{\text{out},\parallel}$ are the in-plane components of the incident and diffracted wave vectors, respectively, and $\mathbf{G}$ is the lattice momentum or the reciprocal lattice vector. The reciprocal lattice vector is defined as $\mathbf{G} = (2\pi m_1/a_1)\hat{i} + (2\pi m_2/a_2)\hat{j}$, where (a_1, a_2) are the lattice constant in the $x-$ and $y-$directions and (m_1, m_2) are integers defining the order of diffraction. The angle of diffraction (θ_d) can be derived using Eq. (1.13), which for a square lattice ($a_1 = a_2 = a$) is given by [49]

$$\sin^2\theta_\text{d} = \left(\frac{\lambda_0 m_1}{n_2 a}\right)^2 + \left(\frac{n_1 sin\theta}{n_2} + \frac{\lambda_0 m_2}{n_2 a}\right)^2, \tag{1.14}$$

where n_1 and n_2 are the refractive indices of the incident and diffracted media, respectively, θ is the angle of incidence, and λ_0 is the incident wavelength. When the incident field arrives normal to the surface, $\sin\theta$ equals zero, resulting in the following condition for the diffracted wave

$$\sin^2\theta_\text{d} = \left(\frac{\lambda_0}{n_2 a}\right)^2 (m_1^2 + m_2^2). \tag{1.15}$$

When the diffracted angle, θ_d, is 90°, such that $\sin^2\theta_\text{d} = 1$, the wavelength at which the Rayleigh anomaly is diffracted in the plane of the array is equal to

$$\lambda_0 = \frac{n_2 a}{\sqrt{m_1^2 + m_2^2}}. \tag{1.16}$$

The RA can be combined with a localized resonance on a single particle by placing the single particle in a periodic array. This combination yields an enhanced radiative coupling of the localized resonances in the particles of the array due to diffractive coupling between them in the plane of the array. This coherent coupling of the RA and the localized resonance forms a collective resonance,i.e., surface lattice resonance (SLR) which is schematically shown in Fig. 1.6 [49, 50]. The extinction spectrum of a square array with a lattice constant of 300 μm with 200×40 μm^2 rods of gold on quartz with a height of 100 nm is simulated and shown as the red curve in Fig. 1.5. A remarkable extinction close to unity can be observed at 0.43 THz, caused by this coherent coupling between localized and diffracted modes [51, 52].

One of the main features of RAs is that they are highly sensitive to the properties of their surrounding medium, such as the refractive index. This sensitivity is due to the delocalized nature of the diffracted wave, resulting in electric field enhancements in the medium. SLRs maintain this delocalized nature but have a stronger resonant response due to the coupling with the localized resonance of the scatterers. This strong delocalized

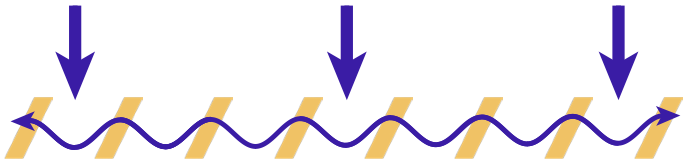

Figure 1.6: Schematic representation of the coherent diffractive coupling between gold rods in a period array, forming an SLR.

response makes them highly suitable for sensing applications, as small variations in the surrounding medium can lead to large changes in the resonance frequency and intensity of the SLR.

1.6.1 Bound States in the Continuum

Bound states in the continuum (BICs) are a special type of states that coexist with a continuum of radiating waves but do not couple with them. They were predicted in 1929 by von Neumann and Wigner in quantum mechanics [53]. However, the concept is a general wave phenomenon and has been identified in electromagnetic, acoustic, and water waves [54]. Conventionally, the confinement of a wave is determined by its frequency: if it exists inside the light cone it leaks radiation away, if it exists outside the light cone it is in a regular bound state. Bound states in the continuum are thus an exception to this general rule. This means that, unlike regular leaky resonances, a BIC cannot be excited by plane waves and is in this sense invisible. BICs are generally realized in extended structures, like photonic crystals and metasurfaces, and are embedded in a continuous spectrum of other modes. There are two different types of BICs, accidental and symmetry-protected BICs. Accidental BICs exist due to the perfect cancellation of two separate resonances which have equal amplitude, but opposite phases at a certain energy and wavevector. Due to this perfect destructive interference, the radiation cancels and the mode cannot radiate. Symmetry-protected BICs exist due to a rotational or reflection symmetry, which does not allow for radiation coupling at normal incidence. In a square lattice of particles, the BIC exists due to π-rotational symmetry. Since the particles are identical, the neighboring particles cannot be excited out-of-phase to each other with plane wave excitation because they are indistinguishable [55–57]. The electric field distribution at the surface of such a symmetry-protected BIC is shown in Fig. 1.7. One of the main features of BICs is that, due to their delocalized nature, they are robust against perturbations, such as changes in the shape of the structure. This makes them highly resistant to scattering losses. Their naturally high Q-factor and potential ease of fabrication make them interesting for applications such as lasers, sensors, waveguides, and filters. In chapter 4 of this thesis, we use a double THz near-field probe microscope to investigate for the first time the field confinement of symmetry-protected BICs.

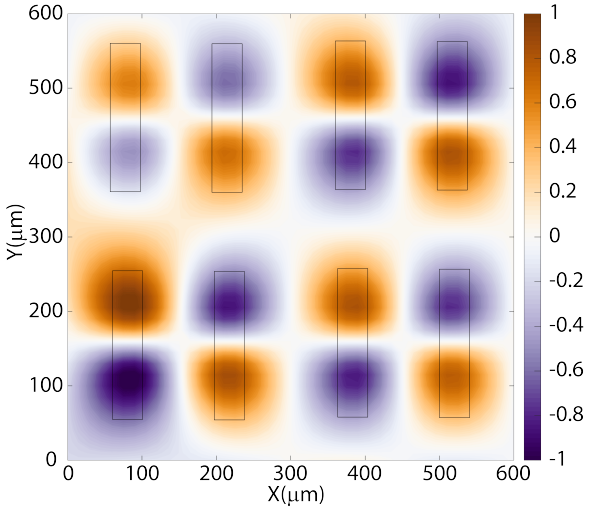

Figure 1.7: Simulated electric field distribution of a symmetry-protected BIC at the surface of a metasurface consisting of gold rod resonators.

1.7 Local Density of Optical States

The presence of resonant structures alters the photonic environment, changing how efficiently a point dipole can interact with its surrounding. There are three levels at which we can quantify the number of allowed electromagnetic modes per unit volume at a given frequency: the density of optical states (DOS), the local density of states (LDOS), and the partial local density of states (PLDOS). These quantities are number densities that describe the number of available states for optical transitions per unit volume and per unit frequency. The DOS is the most general level of description, and it does not account for the spatial distribution of the modes. It is typically used to describe the optical states in infinite free space, and it is useful for calculating the blackbody spectrum and the free-space decay rate of emitters within a certain volume. The LDOS is a more detailed level of description that includes a contribution from each mode in proportion to its electric field intensity at a given point in space. It accounts for the local availability of modes for emission and is appropriate when the electric field intensity varies in space and the emitter samples all directions in space randomly, and on a time scale that is fast compared with the emission lifetime. The PLDOS is the most detailed level of description, and it includes each mode in proportion to the strength of the electric field projected along a given direction. It is relevant when the emitter is sensitive to both the polarization and intensity of the available modes [58]. These three levels of description form a hierarchy, with the PLDOS being the most detailed and the DOS being the most general.

The LDOS a fundamental quantity that determines the strength of the light-matter interactions at that location, and is therefore an important quantity to consider when

designing photonic devices. It is closely related to Fermi's golden rule and the Purcell enhancement factor, which are both important concepts in the study of light-matter interactions. Fermi's golden rule describes the rate at which a quantum system can absorb or emit energy through interaction with an external field. It states that the transition rate between two energy levels in a quantum system is proportional to the square of the matrix element that describes the strength of the coupling between the system and the external field and is inversely proportional to the density of states of the system. The Purcell enhancement factor is a measure of the enhancement of the LDOS in a photonic system and is defined as the ratio of the LDOS in the photonic system to the LDOS in free space. The Purcell enhancement is a measure of the strength of the light-matter interactions in the system.

When concentrating on a small dipole antenna as a source, which is driven by an oscillating electric current, it is important to consider the response of the radiated field on the antenna itself. This is called radiation reaction, where the radiated field does work on the oscillating current on the antenna, determining the radiated power. Radiation reaction can be thought of as the process by which energy is extracted from an oscillating current and transferred into the available modes of the electromagnetic field, where it can then propagate away. The availability of modes changes the emission of the antenna considerably. If the LDOS is high at a given location, there are a large number of available states for optical transitions at that location. In the case of an antenna, this means that there are a large number of modes available to carry energy away from the antenna. If the LDOS is low at a given point, there are fewer available states for optical transitions and, therefore, less energy can be emitted or absorbed at that location.

One way to calculate the LDOS or PLDOS using dyadic Green functions. The (P)LDOS at a given point r can be calculated from the imaginary part of the Green function at that point [58, 59]:

$$\rho(\mathbf{r},\omega) = \frac{2\omega n^2}{\pi c^2}\mathrm{Im}\left\{\mathrm{Tr}[\overleftrightarrow{\mathbf{G}}(\mathbf{r},\mathbf{r},\omega)]\right\}, \tag{1.17}$$

$$\rho_p(\mathbf{e}_d,\mathbf{r},\omega) = \frac{2\omega n^2}{\pi c^2}\mathbf{e}_d \cdot \mathrm{Im}\left\{\mathrm{Tr}[\overleftrightarrow{\mathbf{G}}(\mathbf{r},\mathbf{r},\omega)]\right\} \cdot \mathbf{e}_d. \tag{1.18}$$

These equations can be used to calculate the (P)LDOS at any point in space and for any frequency of the electromagnetic field. It is important to note that the (P)LDOS only describes the number of available modes, but does not describe into which modes the radiation decays.

The (P)LDOS are critical quantities in photonics that play a key role in determining the performance of photonic sources. They are important quantities to consider when designing and optimizing photonic devices for a wide range of applications. In chapter 3 of this thesis, we show the first measurements of the imaginary Green function at the position of the source, thus of the PLDOS, with a double THz near-field probe microscope.

1.8 Terahertz Near-Field Microscopy

The determination of the LDOS and the properties of individual scatterers and particle arrays cannot be determined using only conventional far-field spectroscopy techniques. The electric field localization on resonant structures is generally smaller than their free-space wavelength. Therefore, it is important to be able to resolve features on smaller length scales to accurately determine the interaction between the radiation and the scatterer. The maximum resolution that can be obtained with a certain wavelength using far-field optics is called the Abbe diffraction limit [60],

$$\Delta L = \frac{\lambda}{2n\sin(\theta)} \tag{1.19}$$

with n the refractive index of the medium and θ half of the opening angle of the focused light beam. In the air, the maximum obtainable resolution is equal to half the wavelength of light. For resonant structures, this resolution is insufficient to resolve the relevant electric field enhancements. For example, the gold rods of 200x40 μm^2 discussed earlier have a resonance wavelength of 750 μm. The limited spatial resolution of THz spectroscopic techniques means that local variations in material properties and phenomena caused by evanescent waves like surface waves, surface plasmon polaritons, and edge effects, cannot be detected using conventional far-field techniques. As a result, THz spectroscopy is not able to provide detailed information about these phenomena, which can be important in a variety of applications, including surface analysis and imaging.

To overcome this limitation, a different approach is needed in the form of near-field imaging. The emitted electric field at position $\mathbf{r}$ of a dipole located on the origin can be modeled as a small charge displacement $ds(t)$ oscillating in time and expressed using the retarded time $t_r = t-(r/c)$, with c the speed of the electromagnetic wave in the medium. This charge displacement causes a time-dependent dipole moment equal to $\mathbf{p}(t) = q \cdot ds(t) \cdot \hat{\mathbf{z}}$. Using the retarded potential formulation, the electric field is calculated with [10]

$$\mathbf{E} = \frac{1}{4\pi\epsilon_0}\left[\frac{1}{c^2 r}\mathbf{n}\times\left(\mathbf{n}\times\frac{\partial^2\mathbf{p}(t_r)}{\partial t^2}\right)+\left(\frac{1}{r^3}+\frac{1}{cr^2}\frac{\partial}{\partial t}\right)\left(3\mathbf{n}\left[\mathbf{n}\cdot\mathbf{p}(t_r)\right]-\mathbf{p}(t_r)\right)\right]. \tag{1.20}$$

From Eq. (1.20) it is apparent that the electric field amplitude decays with two different rates, $1/r$ and $1/r^3$. The first component is dominant far away from the source, while the second component is evanescent and dominates close to the source. These contributions are identified by being the far- and near-field, respectively. Measuring the near-field can considerably increase the spatial resolution, because the evanescent waves, which are not limited to the diffraction limit, are detected as well. The first exploration of the near-field was proposed by Synge in 1928, who suggested to use of a small orifice of 100 nm in a thin metal film to surpass the diffraction limit and to subsequently raster scan the object of interest [61]. It would take decades before the diffraction limit was surpassed by near-field techniques, first in the microwave range and later in the optical regime [62, 63].

THz near-field microscopy techniques are used to probe the local properties of materials and structures at THz frequencies and, therefore, they are an important tool for understanding the fundamental properties of materials and their interaction with electromagnetic fields. Several near-field techniques have been developed such as apertures, near-field scatterers, and near-field sources or detectors, such as photoconductive antennas and non-linear crystals.

Apertures are commonly used in THz microscopy to control the size and shape of the THz beam incident on the sample, as well as to block out unwanted radiation [64–66]. Apertures can be used as both the source and detection of the THz microscope and their choice depend on the specific application and requirements. As a source, apertures can be used to shape the THz beam, which can be useful in cases where the sample has a non-uniform response, or when the sample size is smaller than the beam size. Apertures can also be used to block out unwanted radiation, such as noise or stray radiation, which can improve the signal-to-noise ratio and the overall performance of the THz microscope. Apertures can be used as a detector to block out unwanted radiation and improve the spatial resolution of the THz microscope. By using a small aperture, it is possible to achieve higher spatial resolution, but at the expense of lower signal intensity and the concomitant reduction of the signal-to-noise ratio. On the other hand, using a larger aperture can improve the signal intensity but at the expense of a lower spatial resolution. Ultimately, the usage of apertures has resulted in spatial resolutions smaller than $3\mu m$ [67].

Metal tips can be used in THz spectroscopy as probes for near-field measurements, achieving spatial resolutions down to tens of nanometers [66, 68–72]. In this context, a metal tip acts as a local antenna that can be used to probe the electromagnetic fields at the surface of a sample. These tips guide radiation, creating a large field enhancement at the tip apex. When the tip is brought close to the surface the scattering at the surface is enhanced very close to the tip apex and is collected in the far field. By scanning the sample the local properties can be determined.

In this thesis, THz radiation is detected directly in the near-field close to the object of interest using photoconductive antennas. Improved resolution and near-field detection can be achieved by shrinking the detector area and bringing it close to the sample by reducing the size of the gap in a photoconductive antenna, which will be described in detail in chapter 2 [66, 73–76]. This technique has some advantages over methods that use a pinhole aperture or metal tip to enhance the field. Since no pinhole or metal tip is used, the near-field is less distorted and the technique is non-invasive. By changing the shape of the photoconductive antenna, it is possible to independently measure the three components of the electric near field [76]. This will be discussed in more detail in Chapter 2.

1.9 Outline of this Thesis

This thesis discusses the properties of gold resonant structures and semiconductor thin films investigated in the time domain with near-field THz microscopy. The current chap-

ter contains a brief description of the basic concepts used throughout this thesis. *Chapter 2* discusses the experimental setups and methods used in this research. The unique experimental setups developed throughout this thesis are a key factor for the obtained results and are described in detail in this chapter. *Chapter 3* shows how the LDOS is influenced by changes in the photonic environment. Here, the PLDOS is measured in the time domain at a varying distance from a planar interface, as well as surrounding a gold resonator. *Chapter 4* describes how a BIC is tightly confined to the surface of an array of gold dimers. This confinement is strong due to the complete suppression of radiation leakage away from the BIC. This resonance is measured in the time domain by locally breaking the symmetry of the system using a local excitation and detection (near-field) method. In *Chapter 5*, the carrier lifetime of an exfoliated TMD microcrystal is measured in the near-field with sub-diffraction resolution. The material characterization demonstrates the importance of accurately measuring properties on small-length scales. The discrepancy between the carrier lifetimes in the bulk and on the surface of the microcrystal, which is caused by defect-assisted Auger recombination, emphasizes the need for non-invasive measurement techniques on micron-sized samples. *Chapter 6* shows how a breathing phonon mode influences the frequency dependence of the photo-induced conductance of an exfoliated TMD microcrystal. *Chapter 7* provides a summary and a future perspective on near-field THz microscopy. The photoinduced changes in semiconductors and the fundamental properties of resonators can be combined to influence the properties of materials at THz frequencies. For example, a resonant structure can be designed to couple with the breathing phonon mode in the TMD microcrystal. Changes in this phonon mode due to the coupling with a resonant structure could improve the electrical properties of the microcrystal.

CHAPTER 2

EXPERIMENTAL SETUPS AND METHODS

THz time-domain spectroscopy (THz-TDS) techniques are powerful for determining the properties of materials over a broad range of frequencies and on ultrashort timescales. In this chapter, the basics of THz-TDS will be explained, as well as the unique experimental setups used throughout this thesis. We will focus on two near-field techniques that utilize THz radiation to determine charge carrier properties and characterize resonant structures.

2.1 Generation and Detection of Terahertz Radiation

Throughout this thesis, several techniques are used to generate THz radiation. These include photo-conductive antennas, optical rectification, and the photo-Dember effect. All THz radiation is detected by photo-conductive antennas. These techniques are described in this section.

2.1.1 Photo-Conductive Antennas

THz pulses can be generated using photo-conductive (PC) antennas and optical femtosecond laser pulses. The photons in these laser pulses have an energy higher than the band gap energy of a semiconductor material, which allows them to generate charge carriers. These carriers have a very short lifetime of less than one picosecond, which is necessary for the efficient emission or detection of THz radiation. This is generally achieved by increasing the defect density in the semiconductor material, for example growing gallium arsenide at low temperatures (LT-GaAs). The semiconductor has two Au electrodes deposited on top that define the PC gap of the antenna. Between these two electrodes a DC bias is applied, accelerating the photo-excited carriers before they get trapped, and resulting in a short pulse of electromagnetic radiation in the THz frequency range. If the THz radiation source is much smaller in size than its wavelength, it can be treated as a THz dipole with an electric far field that can be expressed as follows [13]

$$\mathbf{E}_{\mathrm{THz}}(t) = \frac{\mu_0 w_0 \sin\theta}{4\pi r} \frac{\mathrm{d}}{\mathrm{d}t_r}[I_{PC}(t_r)]\hat{\theta} \propto \frac{\mathrm{d}I_{PC}(t)}{\mathrm{d}t}, \tag{2.1}$$

where μ_0 is the vacuum permeability, w_0 is the size of the optical beam, θ is the angle to the orientation of the dipole, r is the distance from the source, and $I_{PC}(t)$ is the photo-current in the photo-conductive gap of the antenna. The time-dependent photo-current is a convolution of the optical pulse envelope and the impulse response of the photo-current, which depends on the properties of the semiconductor. Furthermore, the time-dependent photo-current has a linear dependence on the applied bias voltage and the optical intensity [13, 29].

The detection of THz pulses is performed using the same PC antenna but in a different configuration. In the case of detection, the free carriers generated by femtosecond laser pulses are not accelerated by an applied bias voltage. Instead, the electric field amplitude of the THz pulse acts as a time-dependent bias that accelerates the free carriers, resulting in a current proportional to the amplitude and the polarization of the THz electric field [13, 29]. Since the lifetime of the carriers is considerably shorter than the duration of the THz pulse, small portions of the THz pulse can be measured. By changing the arrival time of the optical femtosecond pulses to the THz pulse, the entire pulse can be scanned in the time domain. The use of a photo-conductive antenna for generating and detecting THz pulses is schematically shown in Figs. 2.1a and 2.1b, respectively.

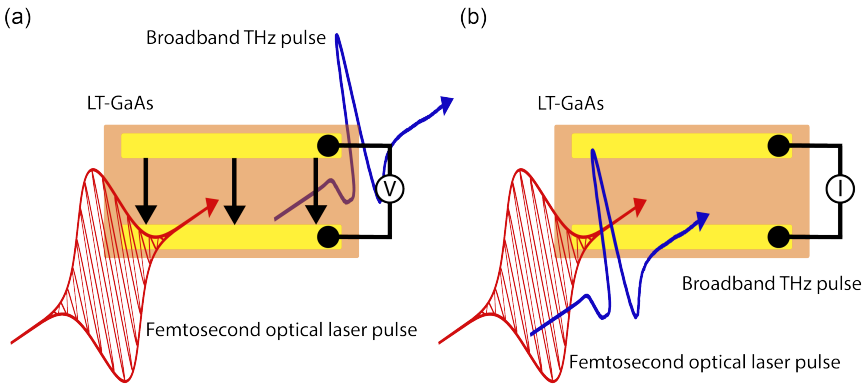

Figure 2.1: Schematic representation of (a) the generation of THz pulses using a photo-conductive antenna, where a DC electric field is applied between two electrodes on a piece of defect-rich semiconductor material. When this semiconductor material is photo-excited by a femtosecond laser pulse, the generated electrons get accelerated by the electric field in the semiconductor, emitting broadband THz radiation. (b) Detection of THz pulses using a photo-conductive antenna, where the AC electric field is provided by the THz pulse, resulting in a current proportional to the amplitude and polarization of the pulse.

Microstructured Photo-Conductive Antennas

In this thesis, the diffraction limit is overcome using a small detector positioned at the sample surface. This scaled-down detector is a commercially available (Protemics GmbH) microstructured photo-conductive antenna (MPCA). The small size of the detector enables measuring the THz response of materials with a spatial resolution of ~10 μm which is considerably smaller than a diffraction-limited resolution of ~ 300 μm at 0.5 THz. Furthermore, since the near-field probe is close to the sample, it enables the detection of evanescent waves which can not be detected using far-field methods.

Since the antennas are sensitive to only one polarization of the electric field, depending on the orientation of the gap between the electrodes. Using different designs for the electrodes all three vector components of the electric field can be measured independently [76]. Microscope images of the two types of MPCAs are shown in Fig. 2.2

2.1.2 Optical Rectification

Another method used for THz generation is based on optical rectification, which is a second-order non-linear optical process. Optical rectification consists of a high-power laser pulse propagating through a non-linear medium, resulting in an anisotropic response from the electronic cloud with a second-order susceptibility that causes an average DC polarization. When a broadband femtosecond laser pulse is used for optical

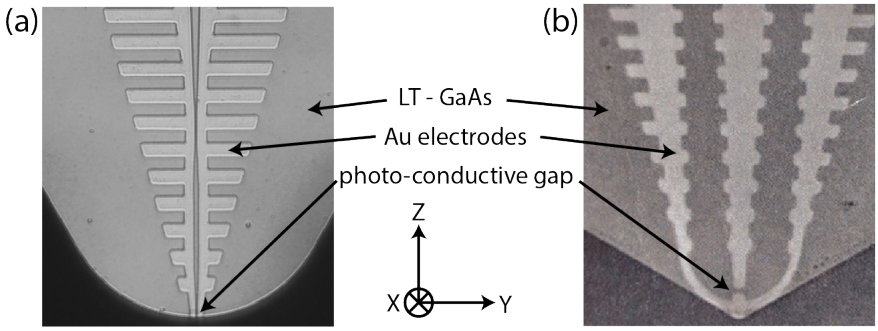

Figure 2.2: Microscope images of two types of microstructured photo-conductive antennas used throughout this thesis. (a) polarized along the X-direction or Y-direction and (b) polarized along the Z-direction.

rectification a beating polarization is produced because of the mixing of the many different frequency components in the pulse. The difference in these frequencies results in the emission of an electromagnetic pulse in the THz frequency range [13]. The generation of THz pulses with optical rectification is schematically shown in Fig. 2.3. One important parameter for the efficiency of optical rectification is the matching of the group refractive indices at optical and THz frequencies for efficient frequency conversion. When these two indices are perfectly matched the THz pulse amplitude increases for the entire propagation length in the material. Destructive interference occurs in the case of a mismatch in group indices, reducing the conversion efficiency. Non-linear materials used for the generation of these THz pulses are zinc telluride (ZnTe), lithium niobate (LiNbO3), GaAs, and GaP [13, 29].

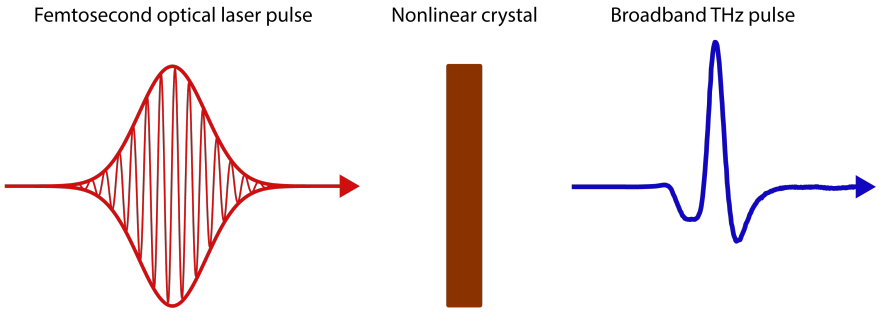

Figure 2.3: Schematic representation of the generation of THz pulses using optical rectification, where a femtosecond laser pulse propagates through a non-linear medium with a second-order susceptibility, causing a low-frequency polarization. The mixing of the frequencies in the femtosecond pulse results in the emission of a broadband THz pulse.

Due to a high nonlinear coefficient, which allows for an efficient generation of THz radiation ZnTe is chosen as THz emitter using an amplified laser setup, which is discussed

in detail in section 2.4.

2.1.3 Photo-Dember Effect

Another method used in this thesis to generate pulsed broadband THz radiation is the photo-Dember effect, which occurs in some semiconductors with a large difference in electron and hole mobilities [77]. The photo-Dember effect does not require electrodes or external fields to be applied on the semiconductor and relies on the difference between the electron and hole mobilities. When an ultrashort optical laser beam with an energy higher than the bandgap is incident on a semiconductor, electrons, and holes are generated at the surface. These charge carriers will diffuse away from the surface, the electrons having a larger diffusion constant due to their larger mobility. Therefore, a net dipole moment will form between the centers of negative and positive charge. This dipole moment will emit a broadband pulse of electromagnetic radiation polarized along the Z-direction. The generation is generally less efficient than one of the photoconductive antennas, but the generated THz field is polarized perpendicular making it a complementary technique. The photo-Dember effect is schematically shown in Fig. 2.4.

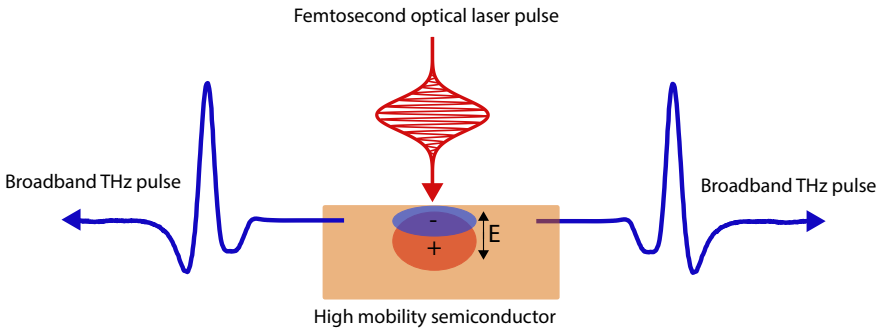

Figure 2.4: Schematic representation of the generation of THz pulses using the photo-Dember effect, where a femtosecond laser pulse generates charge carriers with different mobilities. The diffusion of these carriers will result in charge separation and a net dipole moment, emitting THz radiation.

In this thesis, a 1 μm thick slab of InGAs is used to generate Z-polarized THz radiation using the photo-Dember effect and placed flat on the surface to efficiently couple to resonant structures and to investigate the local density of optical states as shown in Fig. 2.5. All the techniques to generate and detect THz radiation described in this thesis are incorporated into measurement setups that are discussed in the following sections.

2.2 Terahertz Time-Domain Spectroscopy

Terahertz time-domain spectroscopy (THz-TDS) is a measurement technique that utilizes short broadband THz pulses to measure the interaction with samples in both amplitude and relative phase. With a sensitivity to both amplitude and relative phase, the

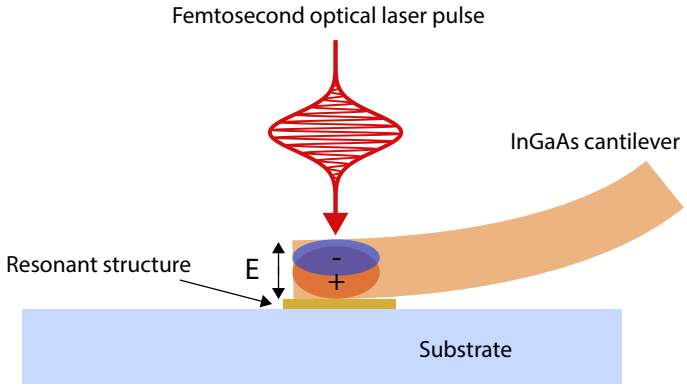

Figure 2.5: Schematic representation of the generation of THz pulses using the photo-Dember effect on a resonant structure.

changes in the THz pulses can be used to determine the optical constants or the complex conductivity of materials in the THz frequency range directly.

THz-TDS makes use of synchronized femtosecond laser pulses which are split in two to generate and detect THz pulses in the time domain using one of the methods mentioned in the previous section. The generated THz radiation propagates through a sample and arrives at the detector. THz pulses can be measured as a function of time by varying the optical path length between the emitter and detector using an optical delay line. A typical THz-TDS setup is schematically shown in Fig. 2.6.

A wide range of semiconductor materials has a metal-to-dielectric transition in their response near the THz or infrared frequency ranges. The ability to probe this transition with THz-TDS, where THz-TDS can span from 0.1-30 THz, is useful for studying the frequency-dependent properties of materials [78, 79]. THz-TDS has been used extensively for the study of semiconductors, molecules, and structured materials [29, 80–82]. Relatively new materials like perovskites, graphene, and other thin-film semiconductors are being investigated thoroughly for various applications, where THz-TDS is used as a contact-less, non-invasive probing technique [32, 83–90].

2.2.1 Experimental Configuration

The THz-TDS setup used in this thesis is a Tera K15 (Menlosystems GmbH) with a bandwidth from approximately 0.1 to 4 THz. The setup consists of an Erbium-doped fiber laser that produces 100 fs laser pulses at a repetition rate of 80 MHz at 1560 nm that excite PC antennas to generate and detect THz radiation. The laser pulses are split and sent to the emitter and the detector through optical fibers. Varying one of the path lengths enables the detection of the THz amplitude as a function of time, i.e., THz transients. The bias voltage on the emitter is modulated at a frequency of 5 kHz to be able to use lock-in detection for eliminating the dark current and achieving a higher signal to noise. After generation, the THz pulses are focused on a sample, and the transmitted field is

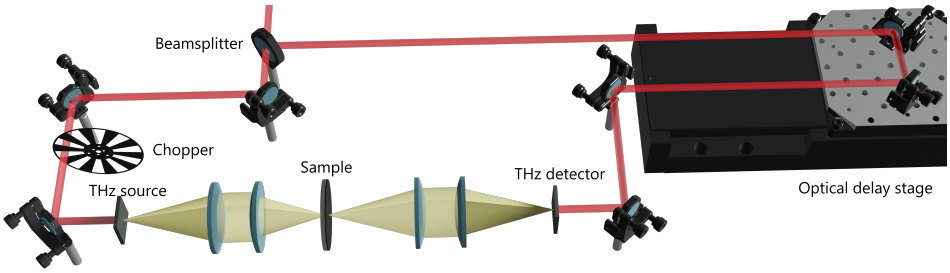

Figure 2.6: Schematic representation of a THz-TDS setup in a 4f configuration. The THz pulses are collimated by the first lens and subsequently focused at the sample position, then it gets collimated again and focused at the detector. An optical delay path is used to scan the THz pulse in time by the ultrashort optical laser pulse.

collected by the detector. Typical THz measurements are shown in Fig. 2.7b, where two THz transients are shown. The reference (blue curve) is propagating entirely through the air, while the second transient (red curve) propagates through 1 mm thick quartz. The THz pulse is delayed by approximately 3.2 ps after propagating through quartz and the amplitude decreased due to reflection at the interfaces and absorption (in the case of quartz only reflection is relevant). The quartz transient also shows the first echo at 12.8 ps after the main pulse. This echo arrives later due to internal reflections in the quartz substrate, as illustrated in Fig. 2.8. When these THz transients, without the first reflection, are Fourier transformed, both the intensity and relative phase can be retrieved, as shown in Figs. 2.7c and 2.7d. From these measurements the fundamental properties such as complex refractive index, absorption coefficient, complex dielectric constant, or complex conductivity can be retrieved over the range of frequencies, given by the bandwidth of the short THz pulses.

This thesis addresses the study of material dynamics as well, by using time-resolved measurement techniques, as explained next.

2.3 Time-Resolved Terahertz Spectroscopy

Time-resolved terahertz spectroscopy (TRTS) is an extension of THz-TDS used to study carrier dynamics in photo-excited materials with femtosecond temporal resolution. TRTS utilizes an additional optical pump beam to generate charge carriers in the sample [22, 29, 91]. The additional free charge carriers in the sample will absorb some of the THz pulse reducing its amplitude. From the frequency-dependent differential transmissivity $\tilde{t}(\omega)$, i.e., the ratio of the THz signal transmitted through the sample with and without the optical pump, the photo-induced conductivity of thin samples (d$\ll\lambda$), $\tilde{\sigma}(\omega)$, can be determined using the following equation [24, 92–94]

$$\tilde{\sigma}(\omega) = \frac{n_{ref}+1}{Z_0 d}\left(\frac{1}{\tilde{t}(\omega)} - 1\right), \tag{2.2}$$

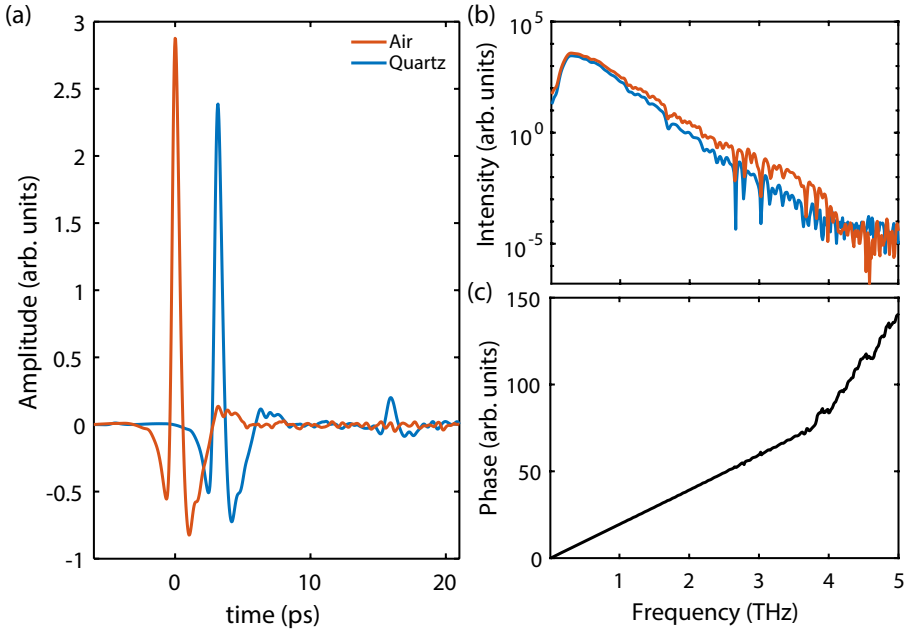

Figure 2.7: (a) THz transients measured with either air at the position of the sample (red curve), or a 1 mm thick quartz substrate (blue curve). The Fourier transform of these transients shows (b) the intensity and (c) the relative phase.

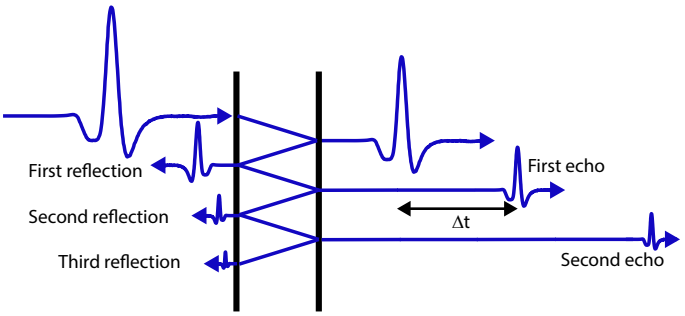

Figure 2.8: Illustration of the echoes of the THz pulse when passing through a substrate.

where $Z_0 \approx 377\Omega$ is the impedance of free space, n_{ref} is the refractive index of the unexcited material, d is the thickness of the sample and $\tilde{t}(\omega) = \tilde{E}_{\text{pump}}(\omega)/\tilde{E}_{\text{ref}}(\omega)$ is the frequency-dependent differential transmissivity between the pumped and the unpumped sample. This equation can be fitted to the measurements to extract the complex conductivity. The change in intensity of the transmitted radiation will be equal to the absolute value of the differential transmissivity squared, i.e., differential transmittance $T(\omega)$.

A pulsed femtosecond laser beam can be used in combination with an optical delay line to measure the time-resolved carrier dynamics. The photo-excited free carriers can relax, form excitons or trions, get trapped, or diffuse before they recombine. The timescale of this recombination is an important material property and a good indication of its quality. For example, a longer recombination time can mean fewer carrier trapping defects resulting in better electrical properties. Varying the time delay between the optical pump and the THz probe pulse yields a time-dependent differential transmittance with a characteristic free-carrier decay time. This is a non-intrusive technique for measuring carrier dynamics since the energy of the electromagnetic wave is too low to alter material properties. Photo-excited free carriers will respond to the electric field of THz radiation, reducing the transmitted THz amplitude while it propagates through the excited sample. An increase in the delay time between the optical pump and THz probe gives the photo-excited free carriers more time to recombine, resulting in a smaller differential transmittance. Measuring THz transients at various delay times enables the determination of the frequency-dependent transient conductivity using Eq. (2.2). This conductivity can be fitted to a physical model, for example, the Drude model explained in section 1.3, to obtain the carrier properties of the photo-excited material like carrier density or scattering time for these different delay times. Furthermore, the pump laser fluence can be changed to measure the photo-conductive behavior as a function of incident laser power, or carrier density, which can be useful to obtain power-dependent absorption and lifetime information. A scheme of the deployed TRTS setup is shown in Fig. 2.9.

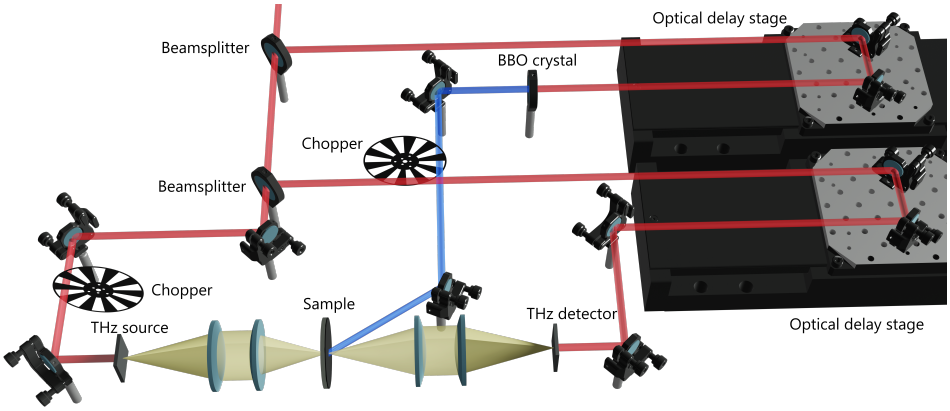

Figure 2.9: Schematic representation of the implementation of an additional pump path to photo-excite the sample in a TRTS setup. The sample is photo-excited with a frequency-doubled synchronized femtosecond laser beam that is chopped to enable simultaneous measurements of the pumped and unpumped signal. There is an additional delay line to change the time between photo-excitation and THz generation, resulting in different arrival times at the sample.

2.4 Time-Resolved Terahertz Near-Field Spectroscopy

The first near-field setup described in this chapter is a microscopic version of a TRTS setup, utilizing an MPCA for THz detection with an increased spatial resolution. In this setup, a regular far-field configuration is used to generate THz radiation via optical rectification, and the THz beam waist is focused on the sample. Instead of collecting the transmitted THz radiation in the far field, the THz radiation is locally detected with an MPCA at the surface of the sample with sub-diffraction resolution. For TRTS a third optical beam is needed for the photo-excitation of charge carriers in the sample. However, at the position of the sample, the MPCA is present to measure the local THz radiation, and this small device is very sensitive to optical radiation. Therefore, a regular optical beam cannot be used to excite carriers because the response of the MPCA will be altered or the MPCA might even be damaged.

To circumvent this issue, an excitation by total internal reflection has been developed. This configuration, shown in Fig. 2.10 together with a zoom of the MPCA at the surface of the sample, uses a Dove prism to ensure that the radiation used to excite the sample does not influence the MPCA measurement. The optical beam enters the Dove prism from the side facet resulting in an angle larger than the critical angle at the sample air interface. Therefore all radiation gets reflected into the Dove prism and the MPCA does not get influenced by the optical beam. Because the front facet of the Dove prism is flat, the THz radiation can pass through and still get focused on the sample without any complications. The Dove prism is brought in optical contact with the substrate using an optical index-matching liquid to ensure that the pump radiation reaches the sample. By using index-matching liquid to ensure optical contact we allow for the sample to be scanned in two dimensions without moving the Dove prism, optical pump beam, THz probe beam, or MPCA. The entire schematic configuration of the setup is shown in Fig. 2.11.

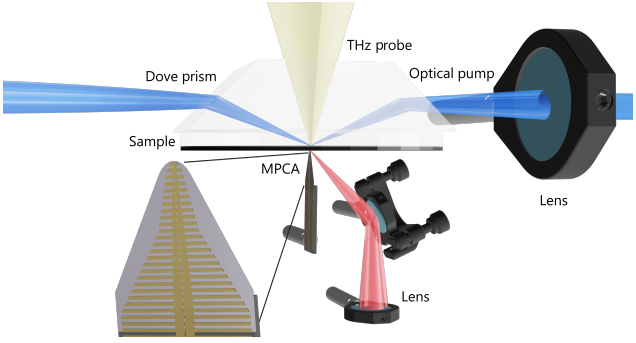

Figure 2.10: Schematic representation of the placement of the Dove prism in combination with the MPCA at the position of the sample, showing the THz radiation incident along the flat surface of the Dove prism and the pump beam being guided along the side facet, resulting in an excitation of the sample with an angle larger than the critical angle. A zoomed schematic of the MPCA is also shown.

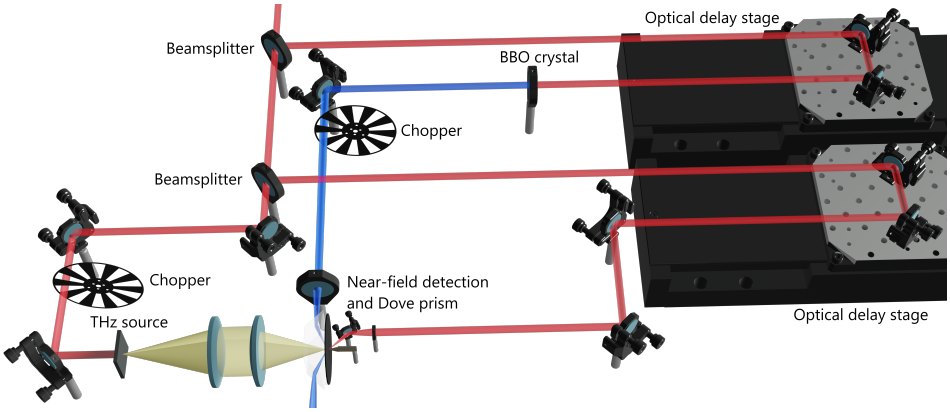

Figure 2.11: Schematic representation of the time-resolved terahertz near-field spectroscopy setup, with the Dove prism, the MPCA, and two pump delay stages.

2.4.1 Experimental Configuration

A Coherent Astrella amplified laser system is used for performing time-resolved THz near-field spectroscopy. The laser generates $\lambda = 800$ nm pulses with a duration of 100 fs and an intensity of 1.2 mJ per pulse at a repetition rate of 5 kHz. The pulse is split into three beams, for THz generation, THz detection, and optical excitation. The THz generation and optical excitation beams are modulated at different frequencies for data acquisition, the details of the scheme are explained at the end of this section. An intensity of 0.5 mJ per pulse is used for generating the THz radiation in a ZnTe crystal by optical rectification. The THz radiation is sent through the sample and its transmission is detected at a distance of 1 μm from the surface of the sample with an MPCA (TeraSpike TD-800-X-WT, Protemics GmbH). The THz pulse is measured in the time domain by delaying the optical probe beam to the THz pulse. The sample can be excited by a $\lambda = 800$ nm pulse or by a frequency-doubled pulse of $\lambda = 400$ nm. The arrival time of the probe beam for THz detection and the pump beam for optical excitation can be varied to the THz pulse with the probe and pump delay stages, respectively. To ensure that every measured portion of the THz pulse encounters the same pump delay time, the pump delay stage can be moved in identical steps as the probe delay stage.

An example of the measurements that can be performed using this setup is shown in Fig. 2.12. These measurements were performed on an epitaxially grown layer of 3 μm thick GaAs wafer bonded to a quartz substrate. Two different measurements are shown, the first measurement is a scan of the THz pulse with and without photoexcitation at a fixed time after the optical excitation of the sample. The second measurement is the retrieval of the carrier lifetime by changing the pump arrival time to the THz probe pulse. During this measurement the peak amplitude of the THz field is measured by the MPCA to achieve the maximum signal-to-noise ratio, as shown in the inset of Fig. 2.12a. The result is a single exponential decay that has been fitted, indicating that the carriers have a characteristic recombination time of $\tau = 155$ ps.

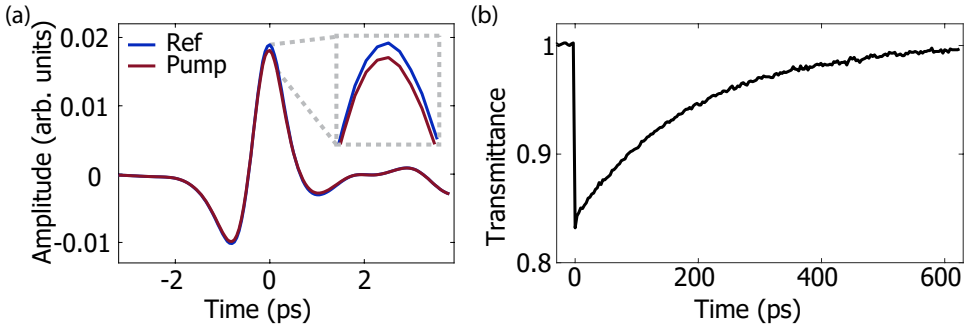

Figure 2.12: (a) THz transient signals obtained using the TRTS microscope with and without an optical pump. The difference between the pumped and unpumped signal is maximum at the peak THz amplitude, shown in the inset. (b) Differential transmittance as a function of the delay time of the optical pump, measured at the peak THz amplitude.

We can perform scans of the pump delay time, as shown in Fig.2.12b, as a function of the position. The scan will give us a map that shows the spatial dependence of the recombination time in the GaAs wafer. Such a map is shown in Fig. 2.13, where the carrier lifetime is fitted and displayed for every position. In this figure, it is clear that the lifetime varies greatly on length scales considerably smaller than the diffraction limit of THz radiation. Therefore, when measuring this sample with a regular TRTS system these spatial differences would be averaged. These differences in small-length scales show the benefit of performing the more complex near-field measurements shown in this section.

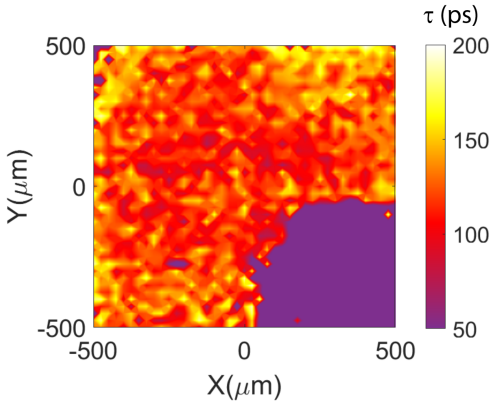

Figure 2.13: Spatial map of the lifetime of photoinduced free carriers of an epitaxially grown layer of GaAs on quartz with a corner cut away for reference. The map shows vast differences in the lifetime on sub-diffraction length scales.

To simultaneously retrieve the THz transmission, as well as the influence of the photoexcitation on the THz transmission, a dual modulation scheme with lock-in detection is used [95]. This scheme is achieved by chopping the THz generation and optical pump

excitation pulses at different frequencies and demodulating the signal in a dual lock-in amplifier at these two frequencies. The THz generation is chopped at a 50% duty cycle, i.e., at 2.5 kHz, while the pump excitation pulse is chopped at a 33% duty cycle, i.e., at 1.667 kHz. These frequencies are chosen because they are not sub-harmonics of each other such that there is no interference between the two channels. By choosing these two frequencies to chop the generation and pump excitation beams the measured data is a mix between the non-pumped (reference) and pumped signals. The reference signal is retrieved by adding the data of both channels, the pumped signal is retrieved by subtracting the data of both channels [95, 96]. Simultaneous data acquisition is not only faster, but also significantly reduces the noise of the measurement by having identical environmental conditions between consecutive measurements. Therefore, the external noise between the pumped and reference signal is correlated and can be filtered out of the measurement. An example of the correlated pumped and reference signals is shown in Fig. 2.14a and the correlated transmittance is shown in Fig. 2.14b. The correlation of the two signals significantly reduces the noise in the transmittance.

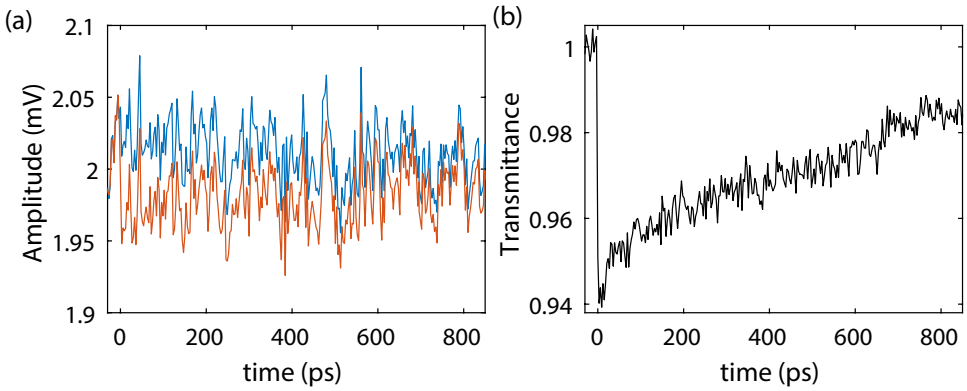

Figure 2.14: (a) Measurement of the pumped (red) and reference (blue) signals as a function of pump delay time. (b) Differential transmittance of the pumped and reference signals. Due to the simultaneous acquisition of the pumped and reference data, most system noise is correlated increasing the signal-to-noise ratio considerably.

Certain considerations need to be taken into account regarding the applicability of this measurement technique. Most importantly, to achieve efficient back excitation of the sample of interest, the substrate needs to be transparent for both the THz and optical pump frequencies. Furthermore, the temporal resolution of the setup is limited by the rise time of the optical pump beam which is stretched in time due to the large angle of excitation and dispersion in quartz to 600 fs.

2.5 Near-Field Generation and Detection

The second near-field setup described in this chapter utilizes MPCAs for both the generation and the detection of broadband THz pulses. This setup allows for a local source to be placed close to an area of interest and for the radiation to be mapped in the near field as a function of space and time. The setup operates in the same manner as a general THz-TDS setup, already described in section 2.2, but the MPCAs size allows for an arbitrary positioning on the sample to scan in the near-field. The radiation pattern emitted by the MPCA is calculated and measured to determine the electric field propagation as a function of time. Since the MPCA is much smaller than the wavelength of THz radiation it can be approximated as a Hertzian dipole, which was discussed in Chapter 1. From Eq. (1.20) the time-dependent emission of a Hertzian dipole can be calculated [57]. The calculated time-dependent emission of a dipole oriented in the z-direction (out of the page) is shown in Fig. 2.15a for three different times. The map shows a single oscillation of the electric field amplitude and a spherical wavefront. This map can be recreated using the near-field generation and detection setup, which is explained in more detail in the next section and is shown in Fig. 2.16, by using MPCAs that emit and detect the z-oriented electric field amplitude. The measured map of the MPCA emission is shown in Fig. 2.15b and closely resembles the calculated electric field amplitude. The possibility to arbitrarily place a dipole source on a sample and scan the coupling of the emission to the sample in space and time using MPCAs becomes very useful in samples with inhomogeneous field distributions, such as resonant structures.

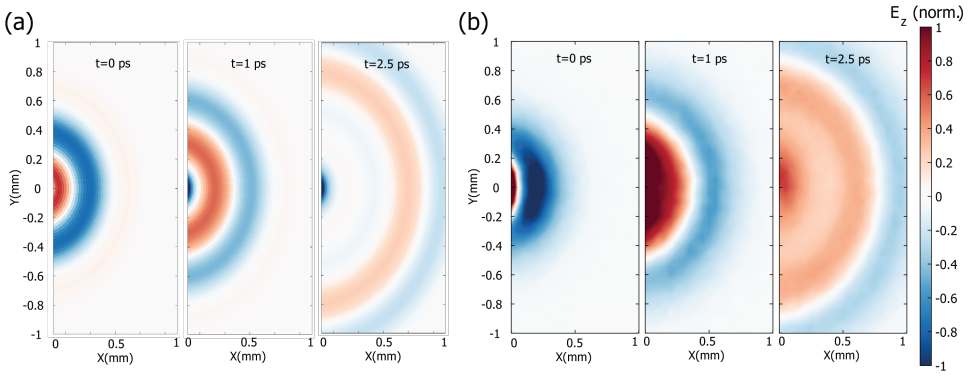

Figure 2.15: Maps of the calculated (a) and measured (b) electric field amplitude emitted by a dipole polarized along the z-direction for different times.

2.5.1 Experimental Configuration

Two separate 3D computer-controlled motorized stages are used for the precise positioning between the source, sample, and detector. On the first 3D stage the sample can be mounted, while the emitter is positioned on the second 3D stage. Since the

MPCAs need to be excited with free space radiation with great accuracy, the incident radiation is coupled into a short optical fiber that couples out on a mount on the same 3D stage, such that the laser beam moves along with the detector. To allow the most flexible configuration possible, the emitter is positioned almost parallel to the sample and perpendicular to the detector. In this configuration, the small angle between the emitter and the sample allows accurate positioning of the emitter along the sample. Two optical beams are used near each other, one for excitation and the other for detection, which needs to be focused independently and without reflections interfering with the other MPCA. Therefore, the signal of the setup depends significantly on the MPCAs used, the distance between them, and the surrounding environment. A schematic of the setup is shown in Fig. 2.16. Both emitter and detector were switched with a focused 100 fs laser pulse from a Menlo TeraK15 at 780 nm. The excitation pulse was approximately 3 mW in power after an optical chopper with a 50% duty cycle with a spot size of approximately 30 microns. The detection pulse was approximately 3 mW in power with a spot size of approximately 20 microns. The measured photocurrent from the detector was sent to a current amplifier (Femto DLPCA-200) and amplified 10^7 times, after which the signal was sent to a lock-in amplifier (Signal Recovery DSP 7270) which was operating at the optical chopper frequency (2 kHz). A time-domain measurement and a spectrum in free space with a distance of several microns between the source and detector are shown in Fig. 2.17, showing a short-lived oscillation in time and a broadband spectrum of approximately 0.2 to 1.5 THz.

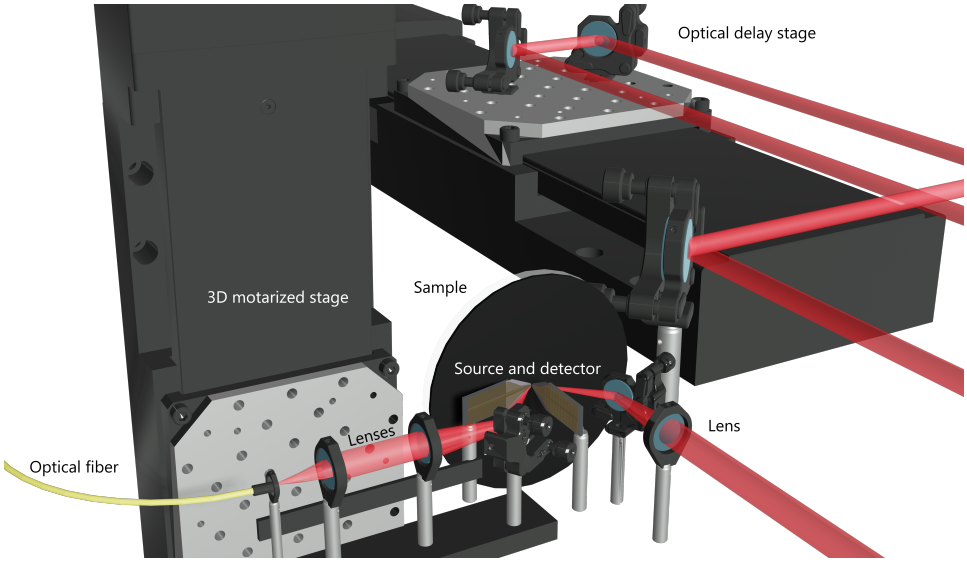

Figure 2.16: Schematic representation of the near-field excitation and detection setup. The source and detector are both MPCAs. To precisely position the source it is placed on a motorized 3D stage. The laser is fiber coupled to the 3D stage to ensure a stable excitation of the THz source.

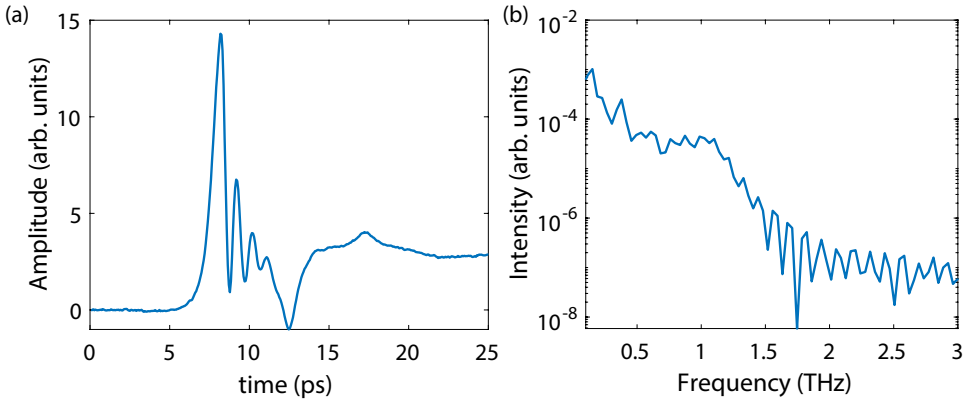

Figure 2.17: (a) Time-domain signal of the near-field near-field setup when the source and detector are positioned a few microns apart in free space. (b) Fourier transform spectrum of the time-domain signal shown in (a).

CHAPTER 3

DIRECT MEASUREMENT OF THE LOCAL DENSITY OF OPTICAL STATES IN THE TIME-DOMAIN

The local density of optical states (LDOS) is one of the most important quantities in photonics, but its direct determination is challenging. An experimental setup is introduced in this chapter which is capable of measuring the THz electric field amplitude in the time domain. From the measured amplitude, the frequency-dependent imaginary component of the electric field can be determined, and the LDOS retrieved. As a proof of concept, this setup has been used to measure the LDOS as a function of the distance to planar interfaces made of gold, InSb, and quartz. Furthermore, the spatially dependent LDOS of a resonant gold rod has been investigated. These results have been compared with analytical results and simulations. The excellent agreement between measurements and theory demonstrates the applicability of this setup for the determination of the LDOS in complex photonic systems.

3.1 Introduction

Changes in the photonic environment are governed by the local density of optical states (LDOS), which is a measure of the number of optical modes per unit volume in a particular region of space. The amount of available optical modes defines how efficiently a source can emit radiation. The LDOS is a key quantity in determining the strength of the interactions between light and matter. Therefore, it is a fundamental quantity in the design of photonic devices [58]. Large LDOS results in many available modes for radiation to be emitted, while a small LDOS means a reduction of the available modes. The LDOS is closely related to the concepts of Fermi's golden rule and the Purcell enhancement factor. Fermi's golden rule describes the rate at which a quantum system can absorb or emit energy through its interaction with an external field. It is based on the strength of the coupling between the system and the field, as well as the density of states of the system. Fermi's golden rule is applied in atomic, nuclear, and solid-state physics [59, 97–99]. The Purcell enhancement factor, on the other hand, is a measure of the enhancement of the LDOS in a photonic system. It describes the enhancement of the spontaneous emission rate of a source due to its photonic surrounding and is equal to the ratio of the LDOS in the medium to the LDOS in free space [100, 101].

The presence of resonant structures changes how efficiently light sources can interact with their surrounding, altering the photonic environment and the LDOS. The spatially dependent strength of the interactions between light and matter is governed by the LDOS and can be engineered by altering the surrounding of a source with resonant structures, increasing or decreasing the number of available modes. It is therefore a fundamentally relevant quantity for energy transfers, [102–106] solid-state lighting, single-photon emitters, solar cells, lasers, and optical sensors. [107–113] The LDOS is not only important in the field of photonics but also has implications for any wave phenomena such as sound waves or in nuclear physics. [114, 115] Generally, the LDOS is determined by investigating the decay and lifetime of a source, which is altered by the LDOS, but measuring the LDOS directly remains challenging.

In this chapter, we use a local excitation and detection double near-field setup capable of measuring broadband terahertz (THz) pulses in the time domain. Measuring the electric field amplitude in the time domain allows for the determination of the imaginary component of the electric field amplitude. The LDOS for a single dipole orientation is called the partial LDOS (PLDOS) and can be directly obtained from such measurements if the distance between the source and the emitter is considerably smaller than the wavelength. Proof-of-concept measurements are performed by measuring the electric field in the time domain as a function of distance from several planar interfaces, reproducing the Drexhage experiment. Using this method, we also map the PLDOS close to a gold rod resonator. These measurements are supported by calculations and simulations, showing an excellent agreement. This new method allows the first direct measurement of the spatial-dependent PLDOS in complex photonic media and will help to design resonant systems that improve light-matter interaction.

3.1.1 Local Density of Optical States

The LDOS ($\rho(\mathbf{r}_0,\omega)$) at position $\mathbf{r}_0$ and frequency ω , can be calculated with the electromagnetic Green function $\overleftrightarrow{\mathbf{G}}$ [58, 59]

$$\rho(\mathbf{r}_0,\omega) = \frac{2\omega n^2}{\pi c_0^2}\mathrm{Tr}[\,\mathrm{Im}[\,\overleftrightarrow{\mathbf{G}}(\mathbf{r}_0,\mathbf{r}_0,\omega)]], \tag{3.1}$$

where n is the refractive index of the medium and c_0 is the speed of light in a vacuum. The Green function is a 3×3 matrix with components i,j where i,j=x,y,z, which defines the electric field at $\mathbf{r}$ due to a point dipole at $\mathbf{r}_0$. In Eq. (3.1), the LDOS is given by the trace of the imaginary component of the Green function at $\mathbf{r}_0$ from a source located at $\mathbf{r}_0$ as well. The columns of the Green function indicate the three orientations, x, y, and z, respectively. Assuming that the electric field is produced by a point dipole, the Green function is related to the electric field $\mathbf{E}(\mathbf{r})$ of an electric dipole $\mathbf{p}$ at $\mathbf{r}_0$ by [59]

$$\mathbf{E}(\mathbf{r}) = \omega^2\mu_0\mu_1\overleftrightarrow{\mathbf{G}}(\mathbf{r},\mathbf{r}_0)\mathbf{p}, \tag{3.2}$$

where μ_0 is the vacuum permeability and μ_1 is the permeability of the medium. Therefore, the LDOS can be determined directly by measuring the imaginary component of the electric field amplitude at $\mathbf{r}_0$. In an inhomogeneous environment, the emitted electric field amplitude of a point dipole is defined by the intrinsic emission as well as the amplitude scattered from the surrounding and is given as [59]

$$\mathbf{E}(\mathbf{r}) = \mathbf{E}_0(\mathbf{r}) + \mathbf{E}_s(\mathbf{r}) = \omega^2\mu_0\mu_1[\overleftrightarrow{\mathbf{G}_0}(\mathbf{r},\mathbf{r}_0) + \overleftrightarrow{\mathbf{G}_s}(\mathbf{r},\mathbf{r}_0)]\mathbf{p}. \tag{3.3}$$

The rate of energy dissipation of the dipole can be determined from both the intrinsic and scattered electric field amplitudes

$$\frac{dW}{dt} = P = \frac{\omega}{2}\mathrm{Im}\{\mathbf{p}^*\cdot\mathbf{E}(\mathbf{r}_0)\} = \frac{\omega}{2}(\mathrm{Im}\{\mathbf{p}^*\cdot\mathbf{E}_0(\mathbf{r}_0)\} + \mathrm{Im}\{\mathbf{p}^*\cdot\mathbf{E}_s(\mathbf{r}_0)\}). \tag{3.4}$$

By dividing both by the intrinsic electric field amplitude, which is equal to P_0, the change in the energy dissipation rate is determined by the ratio of the imaginary components of the scattered and intrinsic electric field amplitudes

$$\frac{P}{P_0} = 1 + \frac{\mathrm{Im}\{\mathbf{p}^*\cdot\mathbf{E}_s(\mathbf{r}_0)\}}{\mathrm{Im}\{\mathbf{p}^*\cdot\mathbf{E}_0(\mathbf{r}_0)\}}. \tag{3.5}$$

Therefore, we can directly measure the change in the LDOS by referencing the imaginary component of the scattered field on the electric field amplitude without the presence of the scattered radiation.

3.2 Methods

3.2.1 Experimental Setup

The setup consists of two microstructured photoconductive antennas (MPCAs) that act as the local source and detector (see Chapter 2 for a full description). Ultrashort optical

laser pulses are split and subsequently used for the generation and detection of the THz pulses. A broadband THz pulse with a frequency ranging from 0.3 to 1 THz is generated by the emitter with an optical laser pulse. The generated electric field is oriented along the gap between the Au electrodes. This THz pulse is detected by the second MPCA using the other part of the split laser pulse. Since this optical probe pulse is much shorter than the THz pulse, the THz pulse can be measured in small temporal steps of 100 fs which is approximately $1/30^{\text{th}}$ of the temporal width of the THz pulse. By varying the time delay between the two optical laser pulses with a mechanical delay stage, the THz pulse can be measured in the time domain, retrieving the electric field amplitude as a function of time. A more detailed description of the technique is given in Chapter 2. By positioning the emitter and detector very close to each together, at much smaller distances than the wavelength of the radiation, the influence of the photonic surrounding of the source can be measured directly. Due to the general non-invasive character of the MPCAs and the fact that the measurements are referenced to themselves, the influence of the detector on the source is modest. Both the emitter and detector are excited by laser pulses in free space and crosstalk should be avoided. Therefore, the emitter and detector have a slight offset (10 μm) in one dimension to avoid the crosstalk due to scattering. The positioning of the two MPCAs in the configuration to measure the LDOS is shown schematically in Fig. 3.1.

Note that in Eq. (3.5) the sum of the scattered fields using all three dipole orientations has to be taken into account. Since we only measure along a single dipole orientation, defined by the gap of the MPCA, we determine the partial LDOS (PLDOS) along the Y-direction ($\rho_y(\mathbf{r}_0,\omega)$). To determine the LDOS a sample should be measured three times, two times with the setup shown in Fig. 3.1 with a 90-degree rotation of the sample between measurements to determine $\rho_x(\mathbf{r}_0,\omega)$ and $\rho_y(\mathbf{r}_0,\omega)$, and one time with a different set of MPCAs with their dipole moment oriented along the Z direction for both emission and detection.

3.2.2 Simulations

Simulations of the PLDOS are performed with two different methods. The first method is finite difference time domain (FDTD) simulations using Lumerical. With FDTD, the behavior of a system is analyzed by discretizing the domain in both space and time and approximating Maxwell's equations using finite differences. The solution to the equations at each discrete point in space and time is found by iteratively updating the values at each point based on the values at nearby points. This process is repeated until the solution has converged or until the simulation has run for a specified time. Using this method an interface separating two mediums or a gold rod is simulated with a local dipole source. The change of the emitted radiation from the dipole source is calculated and referenced to the emission from the dipole source without the change in the photonic surrounding.

The second simulation method is a boundary-element method of electromagnetic scattering using SCUFF [116, 117]. SCUFF is an open-source CAD tool for Photonic Design Modeling that calculates the LDOS by solving for the electromagnetic fields in the presence of a point source using the dyadic Green function. The dyadic Green

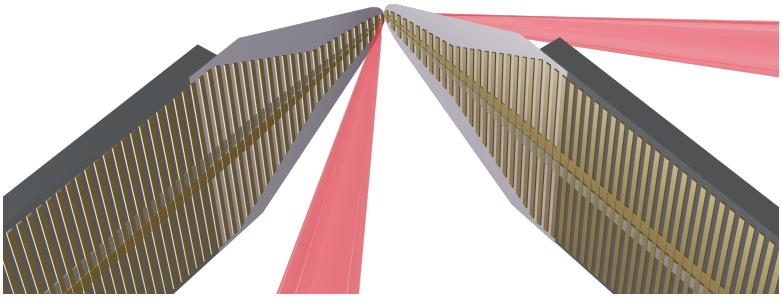

Figure 3.1: Schematic representation of the placement of the two MPCAs for excitation and detection of THz pulses and the measurement of the PLDOS. The MPCAs are placed as close as possible to each other with a minor offset in the Y-direction to minimize the crosstalk.

function provides a general solution for the electromagnetic fields in a homogeneous, isotropic medium in the presence of a source. SCUFF computes the scattering part of the dyadic Green functions of a certain geometry for a given angular frequency and position. The fields generated by a point source are then obtained by evaluating the dyadic Green function at each point in space and summing over all source points. To obtain the LDOS, the traces of the imaginary component of the dyadic Green functions are calculated. This information can then be used to visualize the electromagnetic energy distribution and to obtain insights into the electromagnetic properties of the materials and the interactions between different components.

3.3 PLDOS of a Planar Interface

The first performed experiments are similar to the seminal work by Drexhage, where the fluorescence lifetime of a fluorophore was measured as a function of the distance to a mirror [118]. However, instead of measuring the decay rate of a point dipole, we measure the electric field from a broadband microstructured THz source in the time domain at the position of the source. In this experiment, the field is measured as a function of the distance from a planar interface, whose reflection influences the PLDOS. This influence can increase or decrease the PLDOS, depending on the distance to the interface and the wavelength of the radiation. These experiments have been performed with different planar interfaces consisting of a gold mirror, an InSb wafer, and a quartz substrate.

3.3.1 Analytical Calculation of the PLDOS

The change in the PLDOS from a point dipole at a distance from a planar interface can be solved analytically [59]. The scattered electric field $\mathbf{E}_s(\mathbf{r}_0)$ needs to be evaluated at the position of the dipole $\mathbf{r}_0$. The reflected field is equal to [59]

$$\mathbf{E}_s(\mathbf{r}_0) = \omega^2 \mu_0 \mu_1 \overleftrightarrow{\mathbf{G}}_s(\mathbf{r}_0, \mathbf{r}_0)\mathbf{p}. \tag{3.6}$$

Using cylindrical coordinates, $\overleftrightarrow{\mathbf{G}}_s(\mathbf{r}_0, \mathbf{r}_0)$ is given by

$$\overleftrightarrow{\mathbf{G}}_s(\mathbf{r}_0, \mathbf{r}_0) = \frac{\mathrm{i}}{8\pi k_1^2} \int_0^\infty \frac{k_\rho}{k_{z1}} \begin{bmatrix} k_1^2 r^{\mathrm{s}} - k_{z1}^2 r^{\mathrm{p}} & 0 & 0 \\ 0 & k_1^2 r^{\mathrm{s}} - k_{z1}^2 r^{\mathrm{p}} & 0 \\ 0 & 0 & 2k_\rho^2 r^{\mathrm{p}} \end{bmatrix} \mathrm{e}^{2\mathrm{i}k_{z1}z_0} \mathrm{d}k_\rho, \tag{3.7}$$

where k_ρ and k_z are the wavevectors along the radial and z directions, and r^{s} and r^{p} are the Fresnel reflection amplitude coefficients for S- and P- polarized radiation, respectively. Using the following substitutions $s = k_\rho / k_1$ and $s_z \equiv \sqrt{1-s^2} = k_{z1}/k_1$, the normalized rate of energy dissipation can be obtained [59]

$$\begin{aligned} \frac{P}{P_0} =& 1 + \frac{p_x^2 + p_y^2}{|\mathbf{p}|^2} \frac{3}{4} \int_0^\infty \mathrm{Re}\left\{ \frac{s}{s_z} \left[r^{\mathrm{s}} - s_z^2 r^{\mathrm{p}} \right] \mathrm{e}^{2\mathrm{i}k_{z1}z_0 s_z} \right\} \mathrm{d}s \\ &+ \frac{p_z^2}{|\mathbf{p}|^2} \frac{3}{2} \int_0^\infty \mathrm{Re}\left\{ \frac{s^3}{s_z} r^{\mathrm{p}} \mathrm{e}^{2\mathrm{i}k_{z1}z_0 s_z} \right\} \mathrm{d}s. \end{aligned} \tag{3.8}$$

This equation describes the PLDOS modification by the presence of a planar interface (see Eq. (3.5)). It can be solved for interfaces separating gold, InSb, and quartz from a vacuum, as shown in Fig. 3.2, where the dipole is parallel along the interface (y-direction) and radiates with a frequency of 0.8 THz. The permittivity of the materials at this frequency are: $\epsilon_{\mathrm{gold}} = -1.54 \cdot 10^5 + 8 \cdot 10^5 \mathrm{i}$, $\epsilon_{\mathrm{InSb}} = -77 + 23\mathrm{i}$, and $\epsilon_{\mathrm{quartz}} = 4$ [119, 120]. The response for quartz is very different compared to InSb and gold, due to a much weaker reflection resulting in oscillations with a smaller amplitude. InSb and gold give an almost identical response due to their high reflectivity at 0.8 THz until the dipole gets very close to the surface (h<0.05λ). At short distances, the InSb diverges due to the coupling of the radiation to surface plasmon polaritons [121].

3.3.2 Simulations of the PLDOS

In the simulations of the PLDOS using Lumerical, a dipole is placed above a surface with its orientation parallel to the surface. The distance between the dipole and the surface is varied from 10 μm to 500 μm in increments of 10 μm to study the effect on the PLDOS. The output of the simulations includes the total radiated power of the dipole and the electric field at specific positions. The total radiated power is measured using a monitor box placed around the dipole, while the electric field is measured using a point monitor placed at different distances from the dipole. All these positions are in the same plane as the dipole and parallel to the surface. This setup can simulate the finite distance

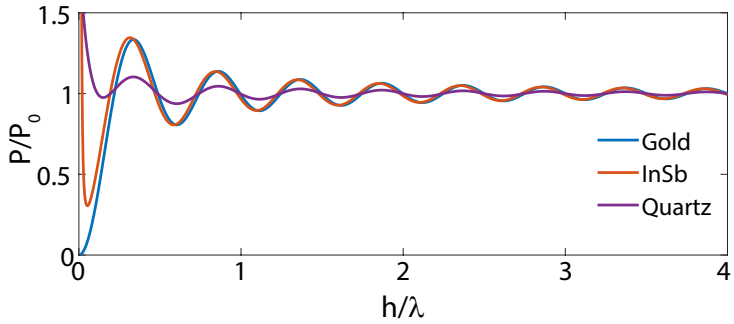

Figure 3.2: Analytical calculation of the rate of energy dissipation of a dipole as a function of the distance from a planar interface for a dipole orientation along the y-direction and for several interfaces separating different mediums from a vacuum. The rate is normalized to the rate of the dipole in a vacuum.

between the emitter and detector of THz radiation in an experimental setup, where the emitter and detector are positioned independently. The simulated radiated power as a function of distance from the planar interface for gold, InSb, and quartz is shown in Fig. 3.3, together with the analytical results from Fig. 3.2 shown as black dashed curves to illustrate that the results are almost identical.

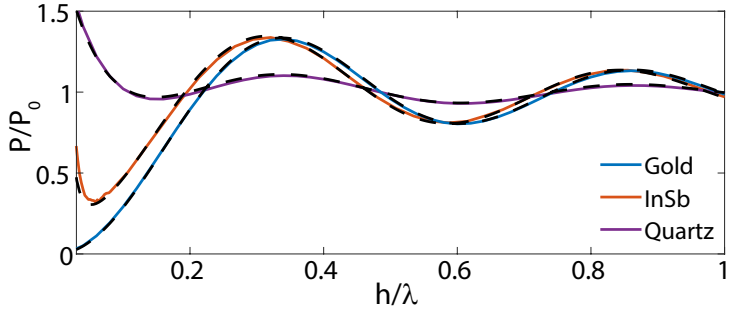

Figure 3.3: Simulated radiated power of a point dipole as a function of the distance from a planar interface for different interfaces. The dipole is oriented along the surface. The black dashed curves are the analytical solutions.

3.3.3 Measurements of the PLDOS

The experimental configuration is shown in Fig. 3.4a, where the colored arrows indicate several distances from the interface and the polarization direction. The source is polarized parallel to the interface. The measured transients at three distances are shown in Fig. 3.4b for the case of the gold mirror. At a distance of 10 μm (blue transient), the source is very close to the mirror (relative to the wavelength), and the electric field amplitude

is considerably quenched. Due to the reduction of the PLDOS close to the mirror, there are fewer optical states allowed and the THz pulse is stretched in time, increasing the time it takes for the source to decay. At a distance of 200 μm (red transient), the electric field amplitude is much larger and the pulse is shorter in time. The reflection from the mirror arrives back at the source 1.33 ps after emission, causing the reflection to interfere with the radiation still being emitted by the source. This results in the observation of several oscillations which are absent at a larger distance (green transient). At the farthest distance of 1500 μm, the source emits all its radiation before the reflection reaches the emitter again, which takes 10 ps. This reflection can be seen as a small oscillation at 15 ps in the green transient of Fig. 3.4b.

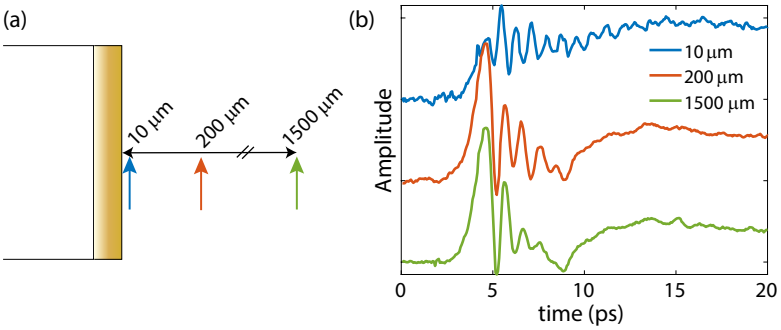

Figure 3.4: (a) Schematic representation of the performed experiment. The distance between the interface and the source is varied, the source is polarized parallel with the surface. (b) Transient signals were measured at 3 distances from an Au mirror.

The three measurements of Fig. 3.4 belong to a large scan at distances varying from 0 to 4000 μm, which has been repeated several times. The average measurements as a function of time and distance to the interface are shown in Fig. 3.5a. At large distances away from the mirror, the electric field amplitude oscillates a few times as a function of time. Starting at 2.7 mm away from the mirror, the reflection becomes apparent as a diagonal, arriving earlier when moving closer to the mirror. At approximately 500 μm, the reflection starts to interfere with the emitted radiation, becoming a single convoluted pulse. At distances closer than 50 μm the entire pulse gets quenched and stretched in time, which is more clearly seen in the zoomed-in map shown in Fig. 3.5b. The PLDOS is determined by the phase relation and the relative amplitude between the emitted signal and the reflection.

To signify the influence of the reflected radiation from the mirror, we can focus on that signal in the time domain. This reflection can be stressed by subtracting the transient signal at a long distance from the interface where the reflection arrives at later times than the measured time window (larger than 2.7 mm). The resulting map reveals the influence of the mirror on the emitted radiation as a function of time and distance and is shown in Figs. 3.5c and 3.5d at two different ranges of the distance from the interface and with different colormap amplitudes. In this figure, the reflection from the mirror is more visible, as well as the increase in the amplitude of this reflection when moving closer to

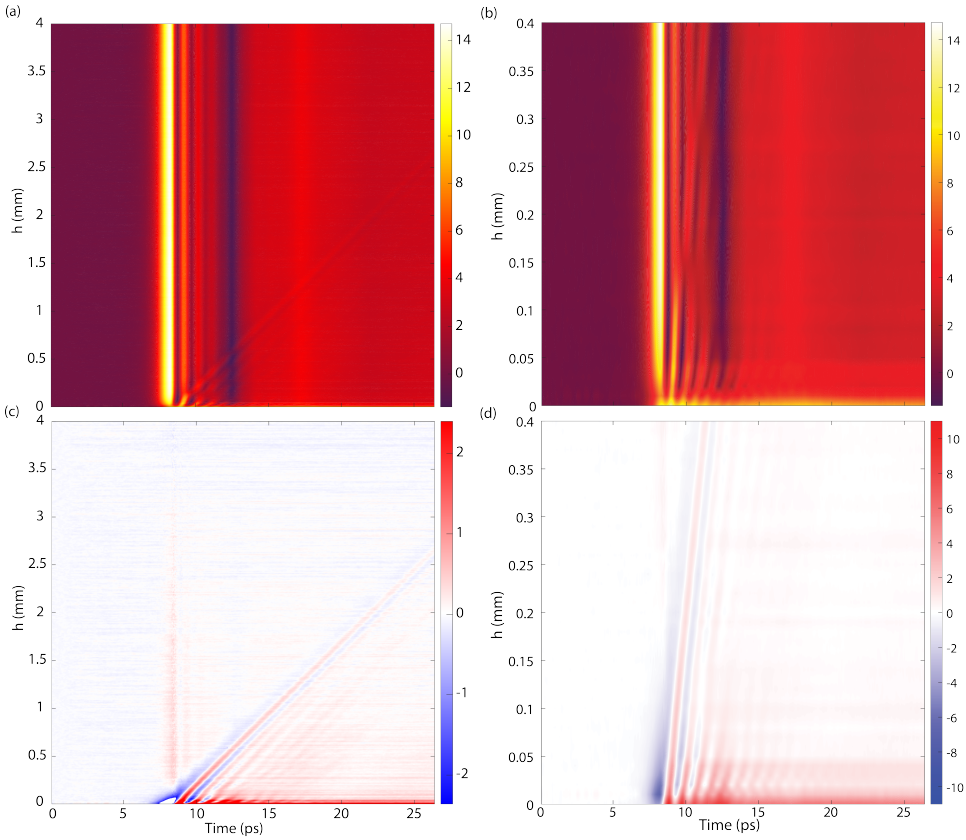

Figure 3.5: (a) Map of the electric field amplitude as a function of time and distance to the mirror. The diagonal signal is the reflection getting delayed by increasing the distance to the mirror. (b) Zoom in on the map of (a). (c) Map of the electric field amplitude difference as a function of time and distance to the mirror. The electric field amplitude at 4 mm is subtracted from each position at every time to clearly illustrate the reflection from the mirror. At distances smaller than 70 μm, the plot is saturated to ensure a clear visualization of the reflection. (d) Zoom in on the map of (c). Note the change in the range of the colormap.

the mirror. It is clear from Figs. 3.5c and 3.5d that the interference with the direct dipole emission (which occurs from 50 to 500 μm and is visible in Fig. 3.5a) does not change the shape of the reflected signal, but is only the sum of the two electric field amplitudes at the respective timing. For distances smaller than 70 μm, the plot in Fig. 3.5c is saturated. Otherwise, the quenching of the electric field amplitude at longer distances would not be apparent.

By Fourier transforming the transient signals, the electric field amplitude can be determined for every frequency at each distance. Since we measure in the time domain, we extract the complex electric field amplitude and investigate the imaginary component.

To ensure that the relative phase in each measurement is the same, an offset is multiplied by the Fourier-transformed complex amplitude. This offset is given by $e^{i\omega t_{peak}}$, where ω is the angular frequency and t_{peak} is the time from the start of the measurement to the peak THz amplitude (approximately 8 ps in Fig. 3.5a). This offset ensures that the phase becomes relative to the time of the THz peak amplitude, instead of the chosen starting time of the measurement. By normalizing this amplitude to measurements where the reflection is not relevant (at distances longer than 2.7 mm away from the interface), we can investigate how the radiative power is enhanced or suppressed by the modified PLDOS at different distances from the interface (see Eq. 3). A map of the imaginary component of the electric field amplitude as a function of frequency and distance to the interface is shown in Fig. 3.6. In this figure clear oscillations of the PLDOS are visible. However, for every frequency these maxima and minima are at a different distance from the interface, showing that the variation of the PLDOS is dependent on the frequency of the source.

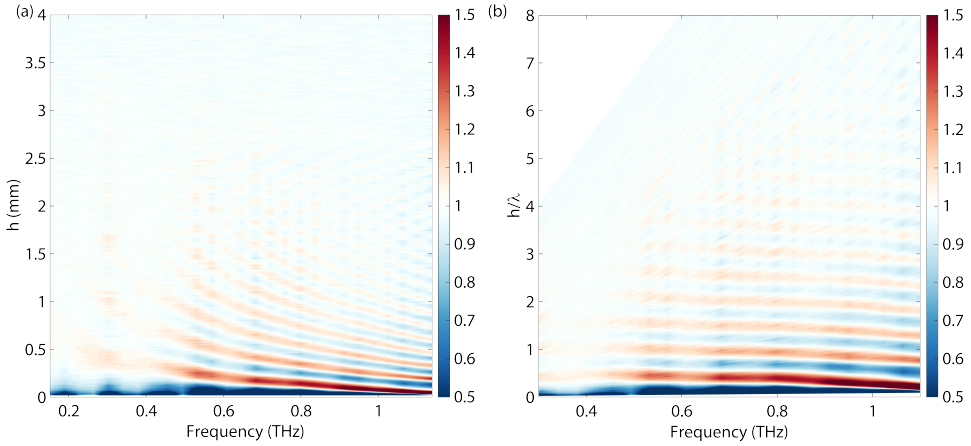

Figure 3.6: Imaginary component of the normalized Fourier transform of the electric field amplitude as a function of frequency and distance to the mirror (a), or distance to the mirror relative to the wavelength (b). There are clear oscillations in the map due to the constructive and destructive interference with the reflection from the mirror. These oscillations occur at the same distance relative to the wavelength when an offset of 25μm is added.

By calculating the distance from the mirror relative to the wavelength, we can see whether the oscillations change relative to the frequency or not. Such a map is shown in Fig. 3.6b, note that an offset of 25 microns is added to flatten oscillations. This offset is due to current limitations in the setup, which is due to the finite distance the source and detector can reach the interface. In Fig. 3.6b, we see that the oscillations are indeed flattened when normalizing the distance from the mirror by the respective wavelength.

The measurements are compared with the analytical results as shown in Fig. 3.7a at 0.76 THz. There is an excellent agreement between measurements and calculations until the emitter gets too close to the gold interface. Close to this interface, the measured

electric field amplitude gets quenched due to the reduced PLDOS. Fourier transforming this small signal results in a small complex electric field amplitude with noise in the phase. This noise disrupts the distribution of the complex electric field amplitude in the real and imaginary components and yields an inaccurate result on the PLDOS, which is solely dependent on the imaginary component.

Similar experiments have been performed at interfaces made of InSb and quartz. After performing the same analysis as for the gold interface, the PLDOS enhancement as a function of distance is determined and shown in Figs. 3.7b and 3.7c at a frequency of 0.76 THz, together with the analytical results. The measurements start at a distance of 20 μm from the interface. The agreement between measurements and theory is exceptional, both for InSb and quartz. Due to this agreement, we are confident that our measurement technique accurately determines the change of the PLDOS due to the photonic surroundings of the source. In the next section, we investigate how the PLDOS is modified by a resonant structure.

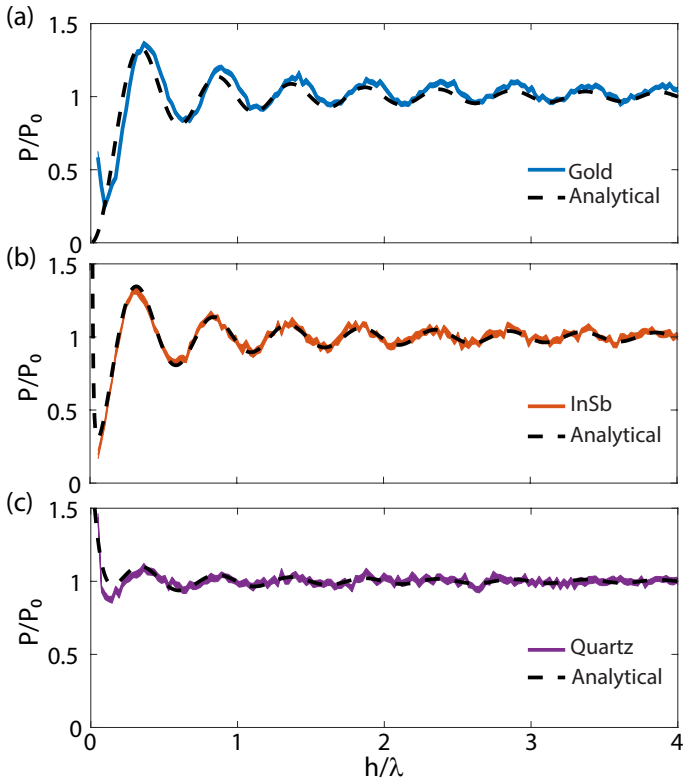

Figure 3.7: Comparison between the measured PLDOS enhancement and the analytical result at 0.76 THz as a function of distance from an interface of (a) gold, (b) InSb, and (c) quartz. The linewidths of the measurement curves are equal to the standard deviation of the mean.

3.4 PLDOS of a Gold Rod Resonator

The structure that will be investigated in this section is a gold rod on a quartz substrate with a $\lambda/2$ resonance in the THz frequency range. By mapping the emission from the source at different positions close to the resonator, the interaction between the source and resonant structure can be determined in terms of the PLDOS. First, the resonant response of the resonator is simulated. After which, it is spatially mapped in the time domain to measure the time-dependent emission of the source as a function of position. The time-domain signal is Fourier transformed to obtain the spatially dependent complex frequency-dependent electric field amplitude, which can be used to determine the PLDOS enhancement. These measurements are compared with simulations of the radiated power from a dipole next to a gold resonator.

3.4.1 Simulations

We have obtained the resonant response of a single gold rod of 200 by 40 μm in size, and with a height of 100 nm on a quartz substrate using FDTD simulations. A total field scattered field simulation was performed, and the simulated scattering efficiency for radiation polarized along the long axis of the gold rod is shown in Fig. 3.8. The scattering efficiency is defined as the scattering cross-section normalized to the geometrical cross-section. The rod shows a broad resonant response centered at 0.4 THz which corresponds to the $\lambda/2$ resonance in the gold rod.

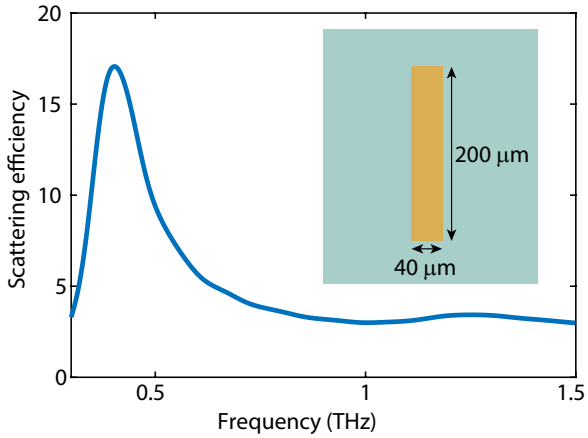

Figure 3.8: Scattering efficiency of a single gold rod of 200x40 μm with a height of 100 nm on a quartz substrate (schematically shown in the inset), obtained by total-field scattered-field simulations.

Similar to the simulations on the planar interfaces, the spatially dependent radiated power of the source and the PLDOS can be calculated close to the gold rod resonator using FDTD simulations. For the gold rod resonator, calculations have been performed

using SCUFF as well. However, instead of a substrate with a refractive index of 2.1 and a superstrate consisting of air, the rod is embedded in a homogeneous surrounding with a refractive index of 1.55. The simulations have been performed at a height of 50 μm from the rod. This height has been chosen based on the comparison made to the experimental results which will be discussed in detail in the next section.

3.4.2 Measurements

The first measurement consists of a linescan of transients close to the surface (a height of approximately 50 μm) along the long axis of the gold rod. The source and detector are polarized along this axis, such that they can couple to the $\lambda/2$ resonance. We will focus the analysis on the data from the top half of the rod. Due to symmetry, we expect the same response for both halves. However, due to a slight misalignment between the source and detector, there is an asymmetry in the measurements. This misalignment is required to minimize the influence of reflected and scattered laser light used for the excitation and detection of the THz pulses. A map of the linescan measurement is shown in Fig. 3.9, where three distinct regions are visible. The first region is far away from the rod, where the transient signal is detected without the influence of the rod. In Fig. 3.9, this region is close to the edges of the measurement (at Y=0-50 μm and Y=450-500 μm). The second region is at the edges of the rod, where an enhanced electric field amplitude is visible, as well as additional time oscillations due to coupling with the rod. The third region is on the rod, here the electric field amplitude is quenched due to the presence of the gold which severely reduces the emission from the source. This region behaves similarly to the case where the source is very close to a gold interface, which has been discussed in section 3.3.

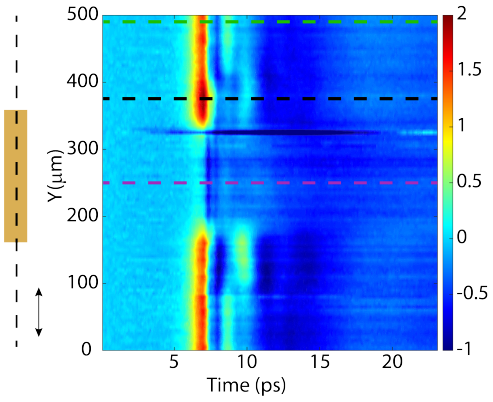

Figure 3.9: Electric field amplitude as a function of time along the long axis of the rod. Three regions are visible: away from the rod, the field is not influenced by the rod; close to the edges, the electric field gets enhanced and more oscillations are visible; and on the rod, the electric field gets quenched due to the reduced PLDOS. The dashed horizontal lines indicate the three distinct regions.

We focus now on the three regions by looking at the transient signals in more detail. The transients of three measurements are shown in Fig. 3.10a, with the positions of the measurements indicated by colored dashed lines in Fig. 3.9. The first transient is the reference measurement far from the rod, the second transient is at the edge of the gold rod and the third transient is at the center of the gold rod. At the edge of the rod, the transient amplitude gets enhanced considerably, indicating that the source modifies its emission due to the change in the PLDOS by the resonant rod. A significant quenching of the emitted radiation is visible on the center of the rod. The spectra of the emitted radiation are very interesting since these spectra should map the resonant response of the gold rod. The intensities of the Fourier transform of the three transients are shown in Fig. 3.10b. At the edge of the gold rod, the emitted radiation is enhanced considerably at frequencies from 0.2 to 0.4 THz. On the rod, the emitted radiation gets quenched for all frequencies. These spectra illustrate that the in-plane Y-field component is enhanced at the edge of the rod due to the excitation of the $\lambda/2$ resonance.

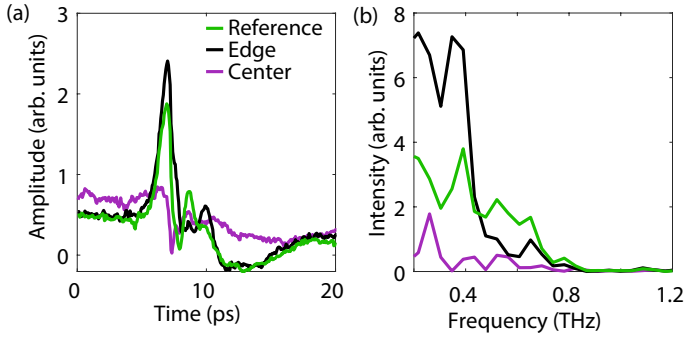

Figure 3.10: (a) Electric field amplitude close to the gold rod resonator as a function of time at three different positions. (b) The intensity of the Fourier transform of the three transients from (a), shows an enhancement for the edge of the rod at 0.4 THz and quenching at the center of the rod.

We are interested in the PLDOS. Therefore, we investigate the normalized imaginary component of the electric field amplitude with and without the influence of the gold resonator. A map of the frequency-dependent normalized PLDOS along the long axis of the rod is shown in Fig. 3.11a. These measurements are normalized to the average value far away from the rod (at Y=500 μm) to isolate the influence of the rod from the quartz substrate. On the rod, the PLDOS is close to 0 and is even negative for some frequencies/positions. Negative values of the PLDOS are attributed to a too-low signal, resulting in a large noise. In Fig 3.11a, the negative values have been set to 0. At the edges of the rod, a PLDOS enhancement is detected close to the resonance frequency, indicating that the source can couple to the resonator from its edges and emit its radiation more efficiently. The two edges show an enhancement with a shifted frequency: the bottom edge shows a peak close to 0.4 THz, while the top edge shows a peak close to 0.3 THz. This resonance shift is most likely caused by the vertical misalignment between the source and detector. Away from the resonance frequency, for example, at 0.5-0.6 THz,

the PLDOS at the edges becomes smaller than one. Far away from the rod, the PLDOS enhancement converges to the expected value of one.

These experimental results are compared with simulations of the radiated power of a dipole source obtained using FDTD at a height of 50 μm from the rod resonator. A similar linescan as the experiment is shown in Fig. 3.11b. Here, the simulation is normalized to the value at Y=0 μm to reference the influence of the quartz substrate. The simulation shows a similar enhancement of the PLDOS at the edges of the rod and a quenching of the PLDOS on the rod. The frequency of the enhancement at the edges is centered at 0.31 THz, which is a considerable redshift compared to the resonance frequency of 0.4 THz, which was obtained with a total field scattered field simulation. This discrepancy is attributed to the different fields measured by the two methods. The total field scattered field simulation determines the scattered field resulting from an incident plane wave into consideration, while the PLDOS simulation only takes the local field along a single polarization into consideration [122].

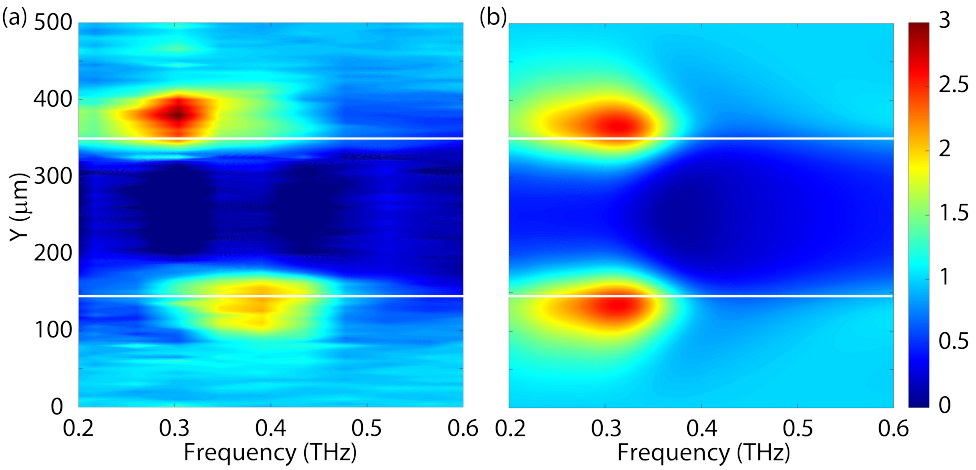

Figure 3.11: Map of the (a) measured and (b) simulated PLDOS normalized by the PLDOS of the quartz substrate as a function of frequency along the direction of the long axis of the rod. The edges of the rod are indicated by white lines.

We have measured a spatial map surrounding the top half of the gold rod resonator as well to visualize the enhancement and reduction of the PLDOS more clearly. A spatial map of the PLDOS at the resonance frequency of 0.31 THz is shown in Fig. 3.12a. Similarly to the linescan measurement, the PLDOS has been normalized to the average value far away from the rod (at Y=250 μm). The PLDOS is quenched on the gold rod and at the sides of the long axis of the gold rod as well. At the edges the PLDOS is enhanced by approximately a factor of three, this enhancement is shaped as a semi-circle and reaches approximately 50 μm away from the edges of the rod. About 100 μm away from the edges, the PLDOS is constant at a value of one.

The measurements are compared with FDTD simulations at the same frequency and

at a height of 50 μm from the gold rod. A map of the simulated PLDOS is shown in Fig. 3.12b. The simulations match well with the experiments, the PLDOS is quenched on the rod and at the sides of the long axis and shows a similar enhancement on the edges.

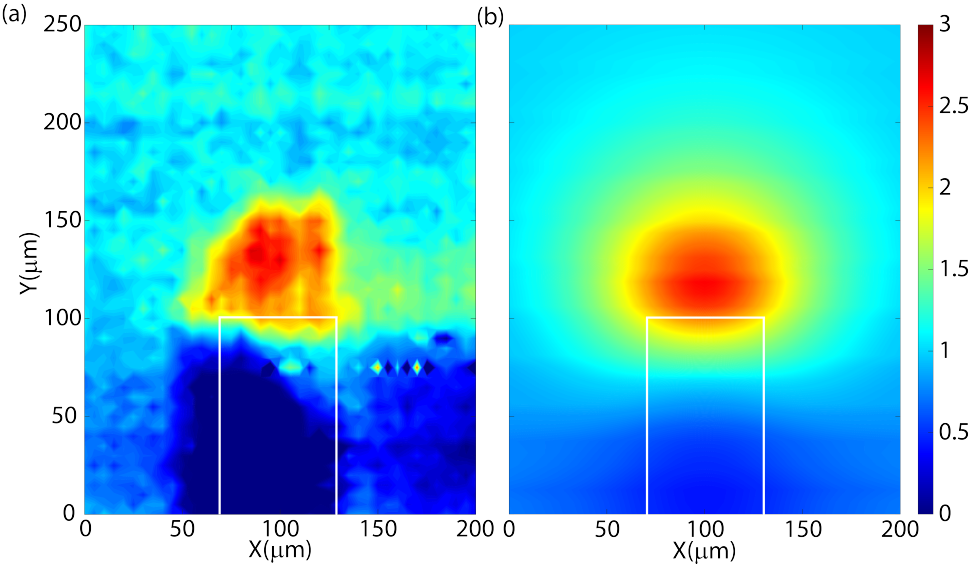

Figure 3.12: Spatial map of the (a) measured, and (b) simulated PLDOS at 0.31 THz of the top half of an Au rod on a quartz substrate normalized by the PLDOS measured on the quartz substrate. The edges of the rod are indicated by white lines.

The PLDOS of the gold rod resonator has been calculated with SCUFF as well at a distance of 50 μm from the rod. The linescan as a function of frequency is shown in Fig. 3.13a and the spatial map at the frequency of maximum enhancement at 0.35 THz is shown in Fig. 3.13b. The calculations obtained with SCUFF are shifted in frequency but similar to the measurements and simulations, showing a distinct enhancement of the PLDOS at the edges at 0.35 THz and quenching on the rod and the sides of the long axis.

3.5 Conclusion and Outlook

In conclusion, we have shown for the first time that we can accurately measure the PLDOS of photonic systems by measuring the complex electric field at the position of a dipole source. Results of the PLDOS are shown as a function of the distance to three different planar interfaces, gold, InSb, and quartz, as well as for a gold rod resonator. The measurements on the planar interfaces have been compared with analytical solutions and FDTD simulations, showing an excellent agreement between the results. The measurements on the gold rod resonator have been compared with FDTD simulations and SCUFF calculations at a height of 50 μm and show a good agreement as well.

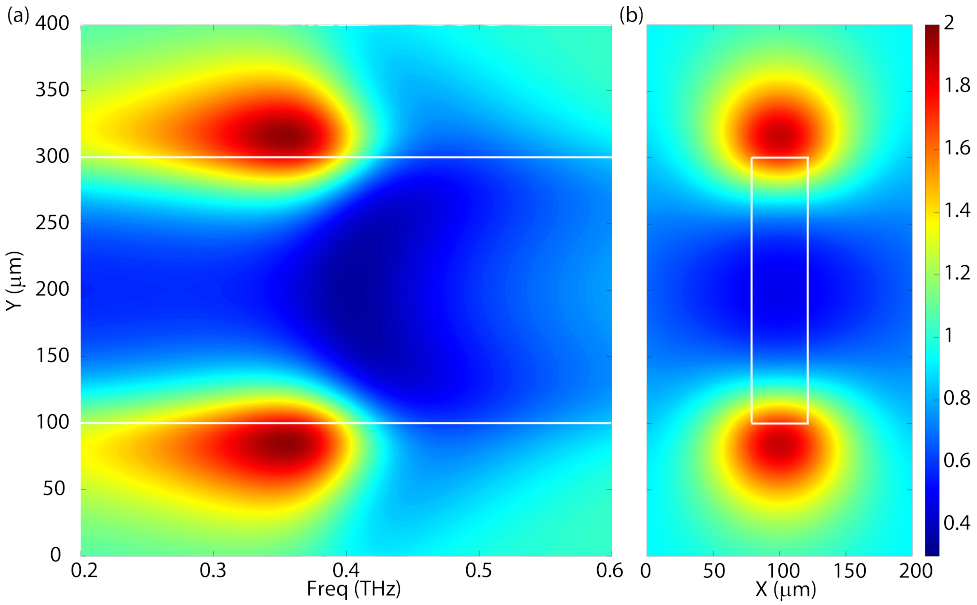

Figure 3.13: PLDOS calculated with SCUFF for the gold rod resonator. (a) Linescan as a function of frequency along the direction of the long axis of the rod. (b) The spatial map at 0.35 THz. The edges of the rod are indicated by white lines.

As follow-up experiments, the PLDOS can be measured using a different polarization direction by changing the local source and detector in the experimental setup. Changing the source and detector would allow for the experimental determination of the LDOS by measuring the PLDOS for all three polarization directions.

Chapter 4

Direct Observation of Lateral Field Confinement in Symmetry-Protected THz Bound States in the Continuum

Electromagnetic field confinement on sub-wavelength scales is possible at the expense of increasing optical losses. Examples are surface plasmon polaritons and resonant structures, which suffer from absorption losses and radiative outcoupling, respectively. Here, we show the first experimental evidence of strong electromagnetic field confinement along the lateral (out-of-plane) direction in a near lossless metasurface that supports a symmetry-protected bound state in the continuum, which fully suppresses the radiative losses of resonant scatterers. This experimental demonstration, supported by coupled dipole calculations, is measured by a double near-field probe technique to locally excite and detect the time evolution and confinement of the electric field onto the surface, achieving an amplitude decay length from the metasurface of $\lambda/38$ at 0.39 THz.

4.1 Introduction

Surface waves at the interface between different media have guided many advancements in photonics, opening new directions in other disciplines enabled by the interesting associated phenomena and potential applications [123, 124]. Examples are Zenneck waves [125], or low-frequency electromagnetic waves at the interfaces between metals and dielectrics, and spoof surface plasmons in perforated thick perfect metal layers with sub-diffraction hole arrays that enhance the field confinement to the surface by mimicking surface plasmon polaritons in real metals [126, 127]. Electromagnetic wave scattering by resonators is an effective way of localizing radiation on sub-wavelength scales at the surface and increasing the interaction strength with matter [120, 128–131]. The resonant response of scatterers at defined frequencies leads to the strong localization of the field [132–135]. However, these resonances are spectrally broad, thus with very short lifetimes due to large radiation losses. This can be improved by combining resonant scattering with surface waves in metasurfaces. The coherent coupling of the scatterers with in-plane diffraction leads to the reduction of radiation losses by destructive interference. In this respect, surface lattice resonances in periodic arrays of resonant scatterers represent a great advancement [52, 136–140]. On the other hand, bound states in the continuum (BICs) are eigenstates of resonant systems that exist inside the continuum of states but do not interact with them [54, 141]. Therefore, resonant metasurfaces supporting BICs offer a unique opportunity to achieve strong field confinements by the full suppression of the radiation leakage, while still having the localized resonant response of the scatterers. The extraordinary properties of BICs have led to significant interest in recent years, including research in nonlinear optics, ultrastrong coupling, optical sensing, low threshold lasing, or polarization filtering [142–147]. However, the direct investigation of BICs has remained elusive since they do not interact with the far-field [57, 148], and most of the research has focused on quasi-BICs where radiative losses are still significant.

In this chapter, we use a unique near-field microscope capable of locally exciting and detecting terahertz radiation in the time domain to investigate the lateral field confinement of a symmetry-protected BIC on a metasurface of resonant gold rods at THz frequencies. Noble metals have very large permittivities in the THz range, leading to slim skin depths and negligible material losses. The near-field microscope allows us to locally break the symmetry by exciting a single resonator and measure the field confinement associated with the BIC on the metasurface as a function of position, height, and time. We demonstrate that the confinement of the BIC in the lateral direction is strong ($\lambda/38$ in amplitude) for high Q resonances with very long lifetimes of over 50 ps. This confinement is experimentally compared with other resonances in similar structures, such as quasi-BICs and surface lattice resonances, showing a significantly larger field enhancement and confinement for BICs. This first investigation and demonstration of the field enhancement enabled by BICs show great promise in applications where strong confinement is needed without sacrificing the Q-factor of the resonance.

4.2 BIC Sample Description

The sample supporting a symmetry-protected BIC consists of an array of gold dimer resonant rods of rectangular shape on a quartz substrate. The gold rods have the lateral dimension l = 200 μm and w = 40 μm, a thickness of h = 100 nm, and are placed in a 300x300 μm^2 lattice. The distance between the two rods in a dimer is 120 μm. An optical microscope image of the sample is shown in Fig. 4.1.

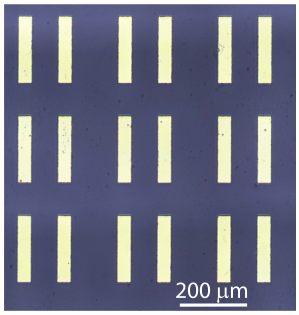

Figure 4.1: Optical microscope image of the sample supporting a symmetry-protected BIC.

To investigate the nature of the BIC, theoretical calculations have been carried out through a quasi-analytical coupled electric and magnetic dipole model (CEMD) for an infinite planar array embedded in a homogeneous environment [56, 149–151]. The response of the metal scatterers is accounted for from their in-plane polarizabilities along the rod axis, which were numerically calculated through the free software SCUFF based on the method of moments [116, 117]. By changing the size of one of the rods in the unit cell, the symmetry in the system is broken. Thus two sub-lattices are created and the resonance can be investigated from the far field. This is reproduced in the CEMD model by changing the polarizability of one of the scatterers in the unit cell. The linewidth of the resonances is given by the imaginary component of the eigenvalues which satisfies the following equation [56]

$$\mathrm{Im}\left[\frac{1}{\alpha_y} - G_{byy} + G_{yy}^{(1-2)}\right] = 0, \tag{4.1}$$

where G_{byy} describes the self-interaction of each sublattice of scatterers, $G_{yy}^{(1-2)}$ describes the interaction between the two sublattices and the polarizability has the following definitions

$$\frac{2}{\alpha_y} = \frac{1}{k^2}\left(\frac{1}{\alpha_y^{(1)}} + \frac{1}{\alpha_y^{(2)}}\right), \qquad \Delta\alpha_y = \frac{1}{k^2}\left(\frac{1}{\alpha_y^{(1)}} - \frac{1}{\alpha_y^{(2)}}\right). \tag{4.2}$$

$\Delta\alpha_y$ represents the detuning between the two resonators. If the detuning is small, the imaginary components of the eigenvalues (the linewidth of the resonance) can be ap-

proximated by [56]

$$\mathrm{Im}[\Lambda^{+}] = \mathrm{Im}\left[\frac{(\Delta\alpha_y)^2}{8G_{yy}^{(1-2)}}\right], \qquad \mathrm{Im}[\Lambda^{-}] = \mathrm{Im}\left[2\left(\frac{1}{\alpha_y} - G_{byy}\right) - \frac{(\Delta\alpha_y)^2}{8G_{yy}^{(1-2)}}\right]. \tag{4.3}$$

So by decreasing the detuning the antisymmetric resonance will narrow until it vanishes when the rods become identical. As stated before, this can be measured by changing the length of one of the rods in the unit cell, while also changing the width to keep the total surface area of the gold rod equal. The far-field THz transmittance spectra have been measured and simulated for several degrees of detuning and the results are shown in Fig. 4.2. It is visible that by decreasing the detuning the antisymmetric resonance narrows and it vanishes for the identical rods (purple curve), due to the full suppression of the radiative losses.

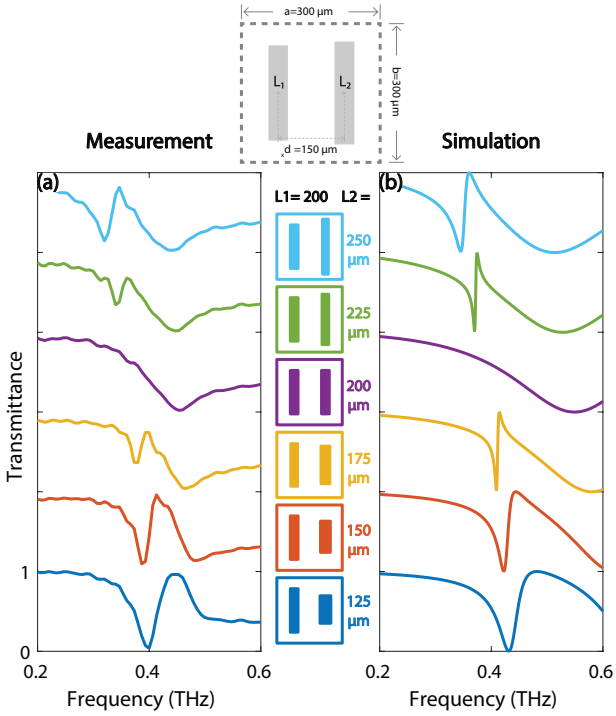

Figure 4.2: (a) Measured transmittance spectra of two gold rods per unit cell, deposited on a quartz substrate. One of the rods has fixed dimensions of L1 = 200 μm and W1 = 40 μm, while the other varies as shown in the center insets, with L2 (μm) = 125, 150, 175, 200, 225, 250, while keeping the surface area fixed: L2W2 = L1W1. All rod thicknesses are t = 0.1 μm. (b) Transmittance spectra numerically calculated through SCUFF [116] for the same geometrical parameters but considering gold rods as planar perfectly conducting rectangles embedded in a uniform medium. Curves are offset by 1 for each different L2. Figure reproduced from [56].

4.3 Setup Description

The setup used to investigate the field confinement of the metasurface consists of a THz time-domain spectrometer (THz-TDS) in which the THz source and detector are near-field microprobes (see Chapter 2 for a full description) [57, 76]. These microprobes are schematically represented in Fig. 4.3 on top of the sample. Short (100 fs) laser pulses (λ = 780 nm) are used in THz-TDS to generate broadband THz pulses. In our case, the THz radiation is generated by the built-in field at the surface of a thin semiconductor layer. The laser excitation spot size defines the size of the THz source ($\simeq 20\mu$m), which we approximate as a point dipole with dipole moment oriented along the z-direction. This source is located on the edge of a gold rod in a dimer. Time-delayed laser pulses are used to gate a microstructured microprobe that locally detects the electric field amplitude as a function of time along the z-direction between the gold electrodes and with a spatial resolution of 10 μm. This microstructured THz detector can be scanned along the surface and in the vertical direction to measure the spatial dependence and decay of the THz-field amplitude. The THz field confinement to the surface associated with the BIC is measured on a rod that is placed one to several unit cells away from the excitation to ensure that only the field associated with the BIC is detected and not direct emission from the source. The detector is moved away from the sample surface in the z-direction in steps of 1 μm. The THz transient (electric field amplitude as a function of time) is measured at each height. The detection is done at the opposite end of the rod compared to the excitation rod to minimize the noise that may arise from the specular reflection of the laser on the emitter reaching the detector.

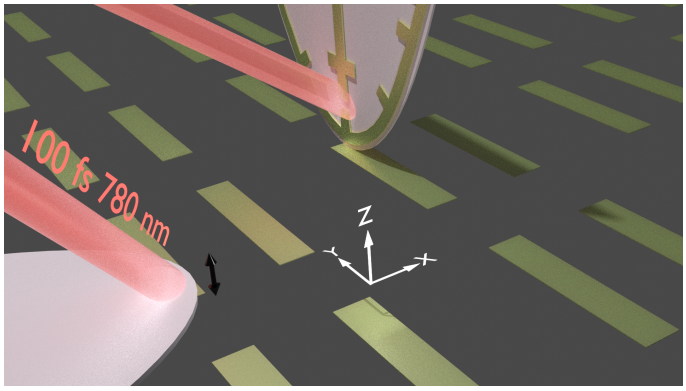

Figure 4.3: Schematic of the setup with the local emitter and detector.

4.4 Results

4.4.1 BIC Field Enhancement and Confinement

To illustrate the coupling of the local excitation and detection setup to the BIC on the surface of the rods, the electric field amplitude at the surface is measured both on the top of the rod, as indicated by the illustration in Fig. 4.3, and between the unit cells (90 μm in the negative X-direction), as shown in Fig. 4.4a. The oscillations, which are characteristic of the long lifetime resonance of the BIC, are visible on the rod and absent between the rods, while the initial pulse at t=0 ps is larger since the measurement taken between the rods is almost 100 μm closer to the THz source [57]. By Fourier transforming the time-domain signals we obtain the frequency-dependent electric field intensity, which is shown in Fig. 4.4b. Here, it is revealed that the oscillations on the rod are at the BIC frequency of 0.4 THz since the intensity at this frequency is considerably larger compared to the electric field intensity measured between the rods.

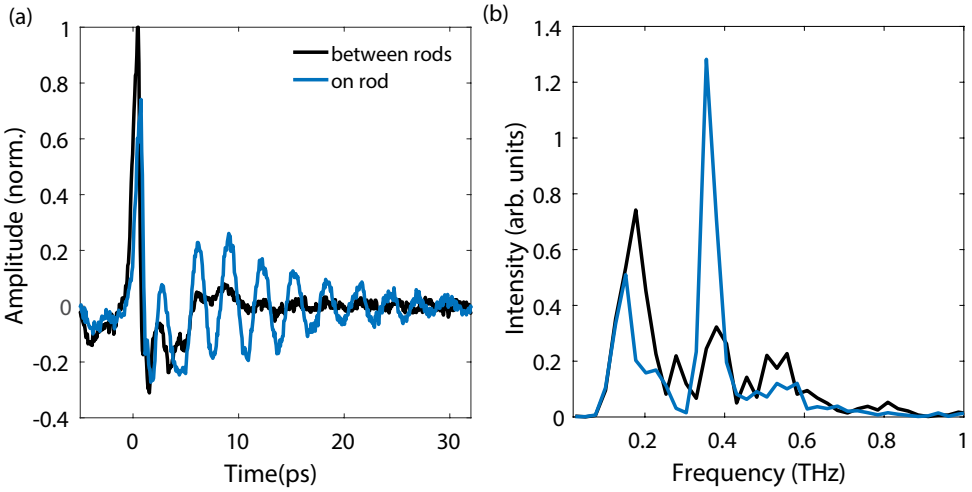

Figure 4.4: (a) Electric field amplitude as a function of time measured on the edge of a rod and between the rods. (b) Electric field intensity of the Fourier transform of the measurements shown in (a).

The electric field amplitude measured as a function of time and height is shown in Fig. 4.5a (upper panel). We also plot in this figure the THz transients measured at height intervals of 10 μm from the surface (lower panel). At 0 ps there is the initial pulse that almost does not change with height. This pulse corresponds to the direct emission from the emitter. After this pulse, there are long-lasting oscillations that originate from the BIC. These oscillations are damped rapidly when increasing the distance between the surface and the detector. This rapid reduction of the BIC amplitude indicates that it is tightly bounded to the surface. The strength of the confinement can be quantified by Fourier transforming the time-domain transients. The frequency-dependent amplitude

enhancement due to the metasurface is determined as a function of height by normalizing the frequency-dependent electric field amplitude to the measured average field at a height of 200 μm from the surface, i.e., a height at which the emission is detected without any influence from the metasurface. This enhancement is shown at height intervals of 10 μm from the surface in Fig. 4.5b. In contrast to the far-field measurements (Fig. 4.2), the near-field spectra show a very narrow resonance at 0.39 THz, which is consistent with the amplitude oscillation in the time domain. These oscillations and resonance are thus unambiguously attributed to the symmetry-protected BIC in the resonant metasurface that can be only probed in the near-field [57]. The electric field amplitude at the BIC frequency is significantly enhanced close to the surface, reaching a 25-fold enhancement at the surface. This amplitude enhancement corresponds to a 625 times intensity enhancement. The enhancement decays swiftly as a function of height, being completely suppressed at a height of 90 μm above the surface.

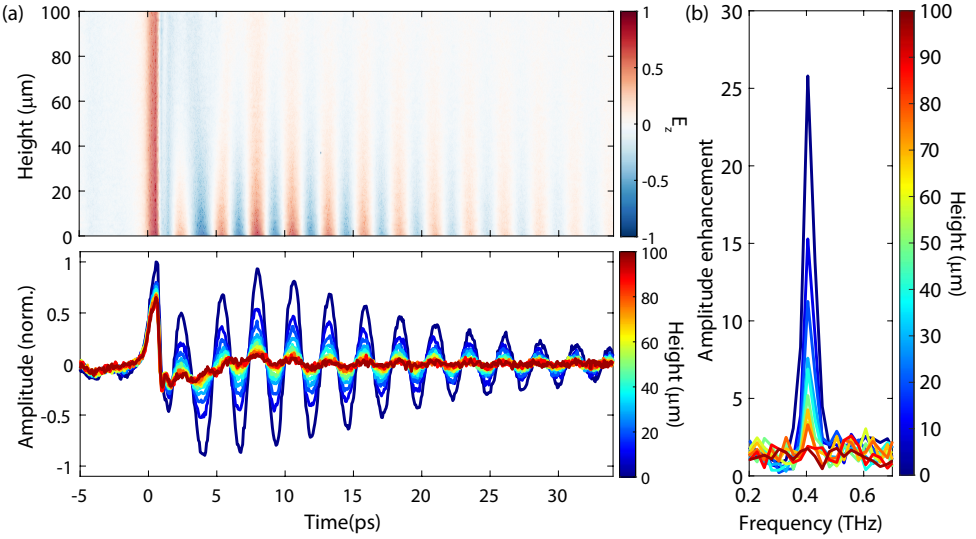

Figure 4.5: (a) Electric near-field amplitude as a function of time and height from the surface of the sample. The upper panel shows the map of the field amplitude, while the lower panel shows the field amplitude transients measured at intervals of 10 μm from the surface. (b) Fourier transforms of the measured transients at 10 μm height intervals, normalized to the averaged field amplitude measured at a height of 200 μm.

Since the symmetry protection leading to the strong field confinement at the surface is a direct consequence of the BIC extending over the entire array, it is relevant to measure this lateral field confinement at positions further away from the THz source. For that purpose, the detector is positioned at a distance from one up to four unit cells away from the emitter, as schematically depicted in Fig. 4.6a. The emitter is shown in this figure, while the colored beams indicate the positions of the detector in subsequent unit cells. The transient signals measured at the surface of the rod resonator for each unit cell are shown in Fig. 4.6b, normalized to the maximum field amplitude measured at

the first unit cell. The initial amplitude peak, before the electric field starts to oscillate, corresponds to the broadband THz pulse reaching the detector without interacting with the metasurface, i.e., the direct emission. The amplitude originating from this direct emission gets reduced by positioning the detector farther away and is negligible at the fourth unit cell. Furthermore, we see that it takes a longer time interval for the BIC oscillations to start after the arrival of the direct emission when the field is probed at longer distances from the emitter. This time interval illustrates the mechanism that leads to the formation of the BIC, consisting of the diffractive coupling of the scattered waves by individual rods in the array [56, 57]. Since the BIC is a mode that covers the entire array, the electromagnetic field originating from the source that couples to the BIC is spreading over the array with time. This is neatly observed away from the source in Fig. 4.6b (at U4), where oscillations remain constant in time once the BIC is excited at t>10 ps. Due to the local excitation and detection scheme, it is not possible to accurately determine the experimental Q-factor of the BIC. Since only a single resonator is excited, which couples with all the other resonators in the array, the radiation is spreading over the array while the BIC is manifesting itself. Therefore, the radiation at the measured positions decreases with time, which does not mean that the radiation is leaking or absorbed. The decrease of the amplitude as a function of time is observed more clearly in the resonators closer to the source.

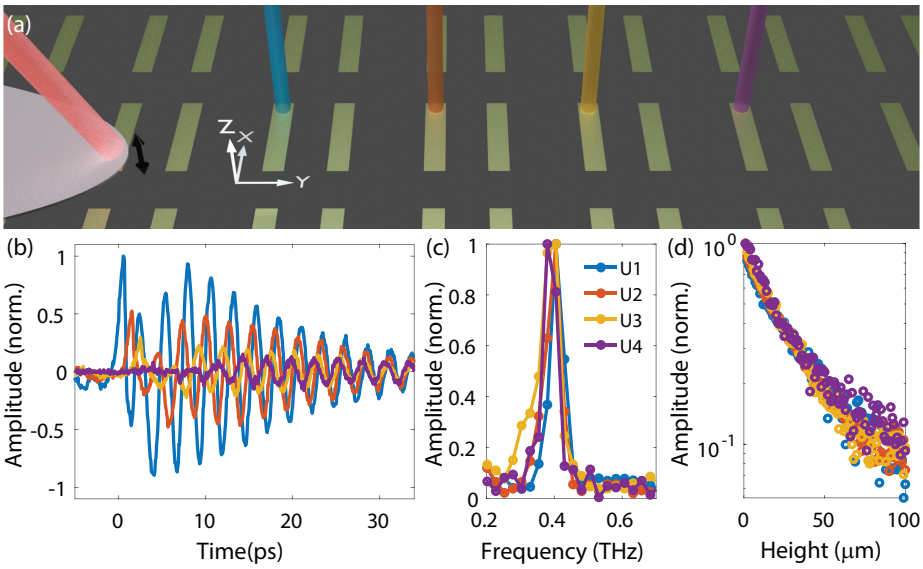

Figure 4.6: (a) Schematic of the local emitter and the various detection locations separated by one unit cell. (b) Electric field amplitude as a function of time measured at the surface and at four consecutive unit cells from the emitter. The color of the measurements illustrates the position at which the measurements are taken as indicated by the same colors as in (a). (c) Normalized amplitude spectra of the electric field for the four unit cells measured at the surface. (d) Normalized amplitude of the electric field at the BIC frequency as a function of height for the four measured unit cells.

The normalized Fourier transforms of the electric field amplitude measured at the different positions are shown in Fig. 4.6c. The field amplitude shows a similar peak at the BIC frequency for each position. There is, however, a small red shift of the peak amplitude when moving farther away from the emitter. The reason for this small shift, which is less than 20 GHz, is unclear but does not influence the interpretation of the results. The normalized electric field amplitude at the BIC frequency as a function of the height is shown in Fig. 4.6d for the measurements at different positions. The amplitude decay is very similar and can be reasonably well fitted with a single exponential, leading to values of the amplitude decay length of 22 ± 3 μm. The measured THz amplitude decay corresponds to extreme electromagnetic field confinement to the surface of the metasurface of $\lambda/38$ at 0.39 THz in an almost lossless system. To the best of our knowledge, this is the strongest electromagnetic field confinement reported on an extended surface at THz frequencies.

These results have been also compared with calculations using the CEMD model. Rather than a plane wave scattering problem, a spatial Green function calculation is carried out [151], placing the dipole source at one of the (fixed) arguments and scanning the other one on a line above the resonators of adjacent unit cells. The calculated electric field decay of the E_z component and the total field, which show a decay length of 50-60 μm for all positions at a height larger than 60 μm are shown in Fig. 4.7. Multipolar contributions are more important closer to the particles and the point dipole approximation becomes invalid, which results in a strong deviation from the measurements. These deviations are apparent, especially in the E_z component of the field which becomes zero in the metasurface plane for a theoretical array of in-plane dipoles. This is in stark contrast with the electric field on gold rod resonators [76].

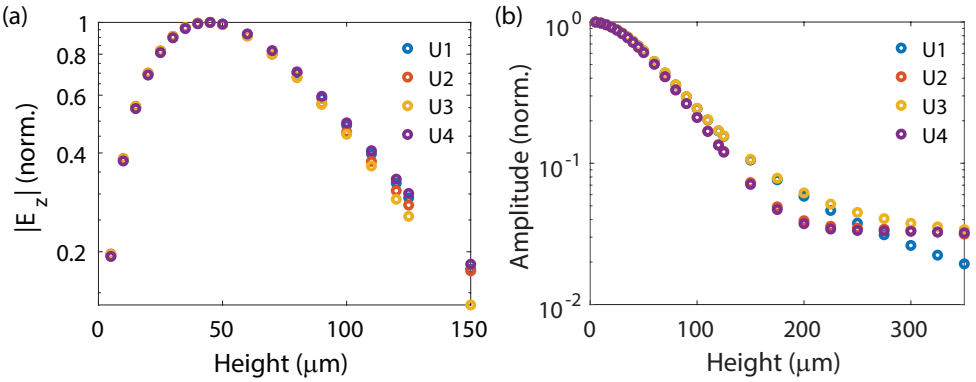

Figure 4.7: Calculated normalized amplitude of the (a) E_z component and the (b) total electric field magnitude as a function of height for 4 adjacent unit cells in the BIC sample.

In the next section, we compare this result to similar systems, demonstrating that the mechanism leading to the extreme field confinement is the combination of resonant scattering by the rods and the suppression of the radiation leakage.

4.4.2 Field Confinement Comparison of BICs, Quasi-BICs, and Surface Lattice Resonances

It is interesting to compare the measured field confinement of BICs with similar structures. Zenneck waves are surface waves at low frequencies at the interface between a semi-infinite metal and a dielectric. The decay length of Zenneck waves into the dielectric is given by $L_z = 1/\Im(k_z)$, where $k_z \simeq \frac{\omega}{c_0}\left[\frac{1}{1+\epsilon_m(\omega)}\right]^{1/2}$ is the wave vector component perpendicular to the surface of the dielectric is air, $\epsilon_m(\omega)$ is the permittivity of the metal at frequency ω, and c_0 is the speed of light in vacuum. The complex permittivities of metals at low frequencies have very large values, given by the high free carrier densities, which lead to a high optical impedance at the surface, the concomitant small skin depth in the metal, very low optical losses, and weak confinement of Zenneck waves to the surface. In the case of Au at 0.4 THz we obtain $L_z = 41$ cm.[125] Therefore, the confinement of the BIC on the metasurface of gold rods is 15000 times stronger than the confinement of Zenneck waves on a continuous Au interface.

The field confinement can be improved significantly by perforating the semi-infinite metal with subwavelength holes such that the electromagnetic field effectively penetrates the perforated metal. This system sustains the so-called spoof surface plasmons in (nearly) perfect conductors that mimic the dispersion and properties of surface plasmon polaritons.[126] Using this concept, Williams et al. have demonstrated an impressive improvement of the confinement of THz waves to the surface:[127] At 0.4 THz, $L_z = 2.5$ mm for spoof plasmons in a metal layer with a thickness of 58 μm. The field confinement of the BIC at the same frequency on a dimer metasurface is thus a factor 90 higher than for spoof plasmons, while the thickness of the Au rods in the BIC sample is only 100 nm, thus a factor 580 thinner than the spoof plasmon sample. We note that the decay length of spoof plasmons in the dielectric can be reduced further at a fixed frequency by tuning the dispersion. However, higher confinement in this system has also higher losses associated with scattering and radiation.

The reason for the exceptionally high electromagnetic field confinement in a BIC formed in an ultra-thin layer of scatterers is the combination of the resonant response of the rods (note that holes in the metasurface supporting spoof plasmons are not resonant) and the full suppression of radiation leakage by symmetry protection. Therefore, we can also compare the amplitude enhancement and field confinement with other resonances in very similar resonant structures. For this purpose two samples have been fabricated: In the first sample, one of the two resonators in the unit cell is slightly reduced in length while keeping its volume constant (from 200x40 μm^2 to 250x32 μm^2, see Fig. 4.8a) to break the π-rotation symmetry in the array and form a quasi-BIC. Quasi-BICs are high-Q resonances that arise upon approaching (in the relevant parameter space) the BIC condition, with reduced but non-negligible radiative losses [55, 56, 152]. In the second sample, one resonator of the dimer is removed to form a sample that supports a surface lattice resonance (SLRs), see Fig. 4.8b [52]. The suppression of one of the two rods in a dimer also cancels the cooperative effect that leads to the vanishing of radiation losses [56]. SLRs are thus surface waves resulting from the enhanced radiative coupling of the individual rods by in-plane diffraction. The far-field transmission measurements

through these samples are shown in Fig. 4.8c.

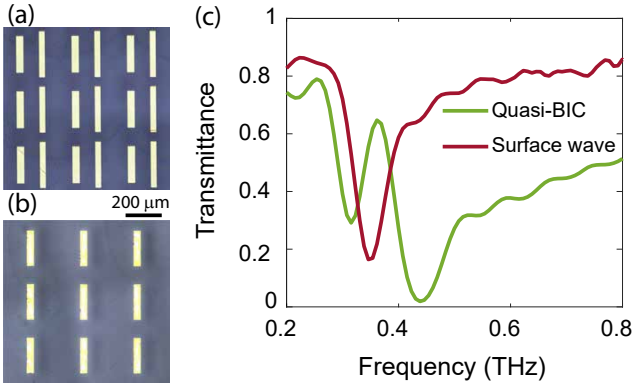

Figure 4.8: Optical microscope image of the quasi-BIC (a) and the surface wave sample (b). (c) Far-field transmittance spectra of the quasi-BIC (green) and surface wave samples (red).

The respective local excitation and detection measurement conditions are schematically shown in Fig 4.9a-c. The resonators on which both the emitter and detector are placed are of identical size for all three samples, while the other resonator in the unit cell is either: identical for the BIC, detuned for the quasi-BIC, or absent for the surface wave sample. The amplitude enhancement and lateral field confinement can be compared by measuring the transient signals, shown in Fig 4.9d for all three samples at the surface, and as a function of height from the surface and Fourier transforming the measurements. The amplitude and lifetime of the oscillations at the surface are different between the three samples, being much stronger and longer for the BIC sample and almost absent for the surface wave sample.

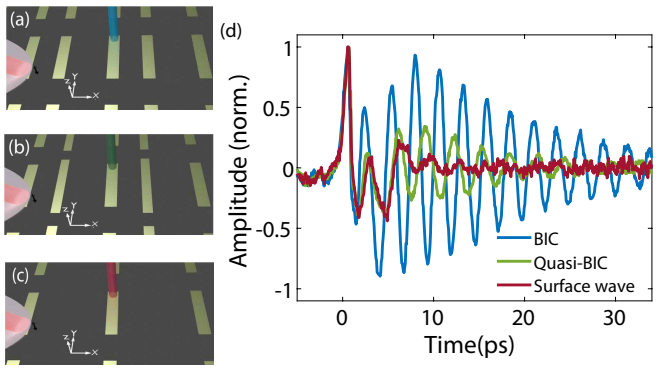

Figure 4.9: Schematic of the local emitter and measurement locations on the BIC (a), quasi-BIC (b), and surface wave samples (c). (d) Time-domain transients of the BIC (blue), quasi-BIC (green), and surface wave samples (red) were measured at the surface.

The amplitude enhancement as a function of height is shown in Fig. 4.10a for the three samples, normalized to their respective measured average field at a height of 200 μm. The BIC enhances the field amplitude at the surface by more than a factor of 25. The quasi-BIC also leads to a relatively large field enhancement, although it is more than a factor 4 lower than the BIC enhancement at the surface. This difference in enhancement, which is also reproduced with the CEMD model as shown in Fig. 4.11, is very remarkable considering that the only difference between the two samples is the lateral dimensions of one of the rods in the dimer. For the SLR, the amplitude enhancement at the surface is further reduced, being 7 times lower than for the BIC. The normalized electric field amplitudes at the resonance frequencies of the BIC, quasi-BIC, and SLR as a function of height are displayed in Fig. 4.10b. These measurements have been fitted to exponential decay functions (solid curves) to retrieve the amplitude decay lengths. The decay lengths are 25 μm for the BIC, 38 μm for the quasi-BIC, and 150 μm for the SLR. The gray dashed line in Fig. 4.10b represents the lateral decay length of a typical spoof plasmon resonance [127]. The reason for the strong reduction of the amplitude enhancement at the surface and the weaker confinement of the electric field in similar samples to that supporting the BIC is the suppression of the radiation losses in the latter.

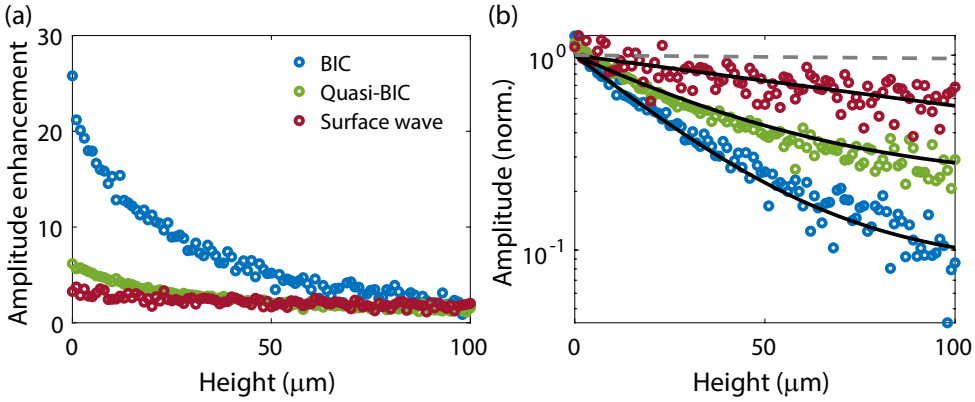

Figure 4.10: (a) Amplitude enhancement as a function of height for the BIC (blue), quasi-BIC (green), and surface wave resonances (red), normalized to their average value at a height of 200 μm.(b) Amplitude enhancement as a function of height normalized to their maximum, fitted with single exponentials (black curves). The gray dashed line indicates the decay of a spoof plasmon polariton for comparison.

4.5 Conclusion

We have experimentally shown that a locally excited BIC on a gold metasurface is extremely well confined to the resonators on the surface of the array with an amplitude decay length of $\lambda/38$. This confinement leads to an enhancement of the amplitude at the BIC frequency of more than 20 times at the surface. We have measured this strong

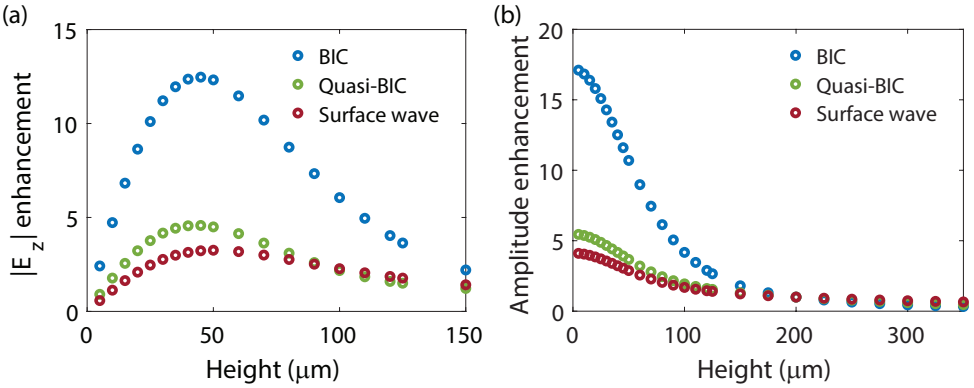

Figure 4.11: Calculated amplitude enhancement of the (a) E_z and the (b) total electric field as a function of height for the 3 different samples one unit cell away from the emitter, normalized at a height of 200 μm.

confinement in one to four unit cells away from the local excitation source and found a similar decay length at all positions. This indicates the efficient manifestation of a BIC with properties that extend all over the planar array. We have compared this result with similar gold structures, supporting a quasi-BIC and a surface wave, whose confinement and enhancement were both considerably weaker. Since the confinement is due to the suppression of radiative losses, these results can be extrapolated to other frequency ranges if the absorption losses in the resonator are negligible. The combination of a long lifetime with a large amplitude enhancement at the surface makes these types of resonances very interesting for applications in sensing, communication, or non-linear optics.

CHAPTER 5

SURFACE ASSISTED AUGER RECOMBINATION IN WS_2 MICROCRYSTALS

Time-resolved terahertz (THz) spectroscopy has been shown as a powerful technique to non-invasively determine the charge carrier properties in photo-excited semiconductors. However, the long wavelengths of terahertz radiation reduce the applicability of this technique to large samples. Using THz near-field microscopy, we show THz measurements of the lifetime of 2D-single exfoliated microcrystals of transition metal dichalcogenides (WS_2). The increased spatial resolution of THz near-field microscopy allows spatial mapping of the evolution of the carrier lifetime, revealing Auger-assisted surface defect recombination as the dominant recombination channel. THz near-field microscopy allows for the non-invasive and high-resolution investigation of material properties of 2D semiconductors relevant to nanoelectronic and optoelectronic applications.

5.1 Introduction

The unique properties of atomically thin layers of semiconductors have led to intensive research over the past years. By reducing the dimensionality of transition metal dichalcogenides (TMDs) from bulk to 2D, the electronic band structure changes from indirect to direct semiconductor [33, 34]. The absence of inversion center symmetry in monolayers and the strong spin-orbit coupling leads to a new degree of freedom in charge transport and gives rise to the so-called valleytronics [36], which allows the control electron spin by the handedness of the excitation light [35]. 2D-TMDs have a very strong exciton binding energy due to the quantum confinement of charges, resulting in an extraordinarily high absorptance [38]. Low-dimensional TMDs are therefore potentially interesting for various applications in nanoelectronics and optoelectronics [37–41]. To achieve a high crystal quality, the material needs to be mechanically exfoliated from a bulk crystal, and how the exfoliation is performed can have a large impact on this quality [42]. The capability to determine the crystal quality before further processing is relevant for the realization of functional devices.

Time-resolved terahertz (THz) spectroscopy is a measurement technique that allows for the non-invasive probing of pump-induced carriers with femtosecond temporal resolution [29, 91]. With this technique a femtosecond optical laser pulse is used to excite the sample, injecting charge carriers. The THz probe pulse propagates through the sample and detects these charge carriers. By changing the delay time between the pump and probe, the carrier lifetime, and thus crystal quality, can be determined. However, the resolution of this technique is limited by the long wavelengths of THz radiation, reducing the applicability to large samples that have inferior crystal quality compared to exfoliated microcrystals [32, 87, 153].

In this chapter, we introduce time-resolved THz near-field microscopy to retrieve the carrier lifetime on single exfoliated WS_2 microcrystals of different thicknesses with sub-diffraction spatial resolution. We show that the carrier dynamics in WS_2 are dominated by defect-assisted Auger scattering on the surface and are dependent on the layer thickness. These results illustrate the relevance of performing contact-free and high-resolution THz measurements in exfoliated TMDs for the non-invasive investigation of carrier dynamics.

5.2 Methods

5.2.1 Time-Resolved THz Near-Field Microscopy

The measurements are performed with the sub-diffraction near-field terahertz microscope schematically shown in Fig. 5.1a (see Chapter 2 for a full description) [96]. An amplified ultrashort laser pulse (100 fs) is split into three beams, for THz generation, THz detection, and optical excitation. THz radiation is generated in a ZnTe crystal via optical rectification [154] and sent through the sample. The transmitted THz radiation is detected with a microscopic-sized photoconductive antenna (Protemics GmbH), which measures the local electric field amplitude with a high spatial resolution ($\simeq$15 μm). The

sample is optically excited (λ = 400 nm) from the back through a Dove prism at an angle larger than the total internal reflection angle for the sample-air interface to prevent influencing the detector with the excitation beam. Due to the total internal reflection at the sample-air interface, the excitation beam travels through the sample twice, doubling the effective pump fluence, after which it propagates back into the Dove prism [96].

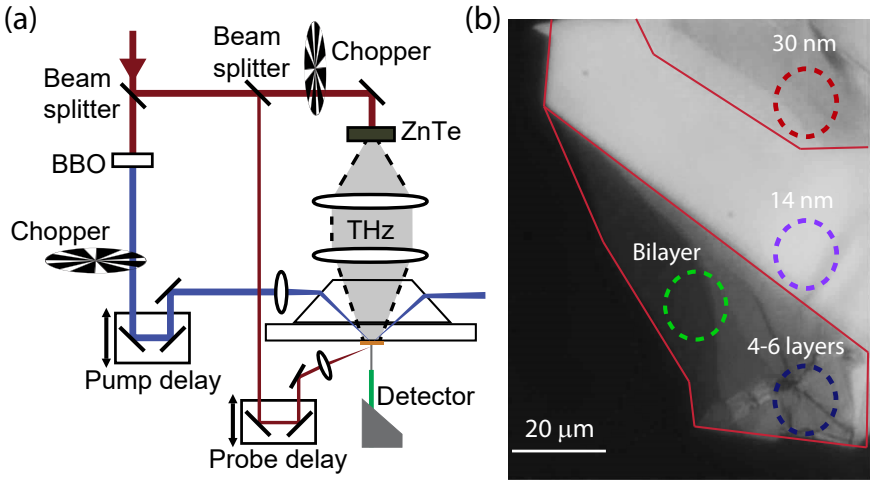

Figure 5.1: (a) Schematic representation of the time-resolved THz near-field microscope. The exfoliated microcrystal is on a thin layer of PDMS on a quartz substrate and it is optically excited from the back through the Dove prism. The microprobe detector is positioned at a distance less than one micrometer from the microcrystal to measure the transmitted THz amplitude with sub-diffraction spatial resolution upon photo-excitation of the microcrystal. The angle of excitation is larger than the critical angle for total internal reflection such that no pump intensity is transmitted and reaches the THz microprobe. (b) Optical microscope image of the exfoliated microcrystal, the red lines indicate the boundaries between regions of different thicknesses, and the dots indicate positions where high-resolution measurements were performed.

5.2.2 Sample Description

A single exfoliated microcrystal of tungsten disulfide WS_2 has been used for the experiments. The microcrystal is mechanically exfoliated using Nitto SPV224 tape from a bulk crystal (2H-WS2 crystal, HQ Graphene). Afterward, it is placed on a polydimethylsiloxane (PDMS) film (Gel Pak, PF-80-X4, 6.5 mil), which is on top of a quartz substrate. An optical microscope image of the exfoliated sample is shown in Fig. 5.1b. The red lines indicate the boundaries between regions of various thicknesses and the colored circles indicate the positions where high-resolution measurements of the carrier recombination time were performed (these measurements are discussed in the next sections). The region at the top right is the thickest region of 30 nm thickness (red circle). Surrounding this region is a thinner region of approximately 14 nm (purple circle). At the edge of the

microcrystal, a larger bilayer region (green circle, 1.4 nm) and some other 4-to-6 layers areas (blue circle) are present. We note that there is a small overlap between some regions due to the limited resolution of the setup, especially close to the bilayer. However, the influence of this overlap is expected to be small because the measurements in Fig. 5.5a show clear distinctions in lifetimes between the different positions. For the THz measurements, the quartz substrate is brought in optical contact with the Dove prism of the THz spectrometer using an optical refractive index matching liquid.

The thickness of the bilayer region has been determined from photoluminescence (PL) spectra, the PL measurements were acquired with a microscope in epi-fluorescence geometry. We excited the bilayer with a 532 nm continuous wave laser through a 40x, 0.6 NA objective with an 8 μW power before the objective lens. The PL signal is filtered from the laser and goes through a 50 μm fiber to an Andor Shamrock 303 spectrometer with an Andor Newton EMCCD camera to obtain the PL spectrum. The spectra of the substrate and the thin WS_2 layer are shown in Fig. 5.2, the indirect peak at 705 nm matches with the emission from a bilayer [155, 156].

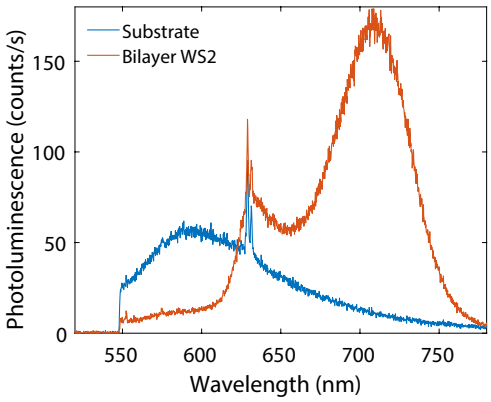

Figure 5.2: Photoluminescence spectra obtained from the substrate (blue) and the WS_2 bilayer (red). From the wavelength and linewidth of the exciton at 630 nm and the indirect peak at 705 nm, the thickness can be determined to be a bilayer.

The thicker regions of the sample were characterized using an atomic force microscope (AFM), Scan Asys Dimension Icon Bruker, to measure the change in relative height (the thickness of the layer) over the sample. The atomic force microscopy measurements were performed in two steps and are shown in Fig. 5.3. The first step is from the bilayer region to the adjacent layer (in blue). The average step size is 12.7 nm, so a thickness of 14 nm is determined. The second step is from the 14 nm region to the thickest region that has been measured (in red). The average step size is 16 nm, so a thickness of 30 nm is determined.

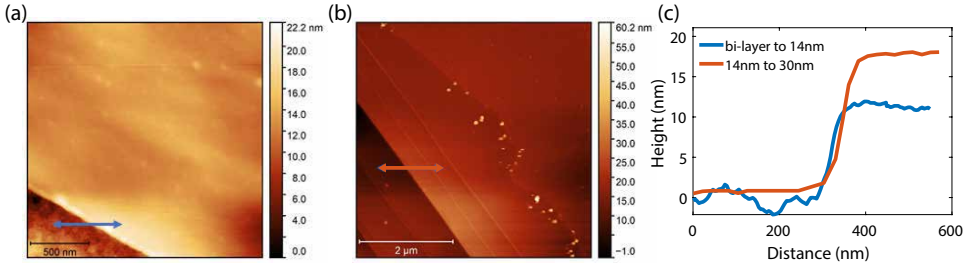

Figure 5.3: Atomic force microscopy measurements of the interface between (a) the bilayer and 14 nm thick region, between (b) the 14 nm to 30 nm thick region, and a (c) linescan of the two interfaces.

5.3 Carrier Lifetime Measurements

Upon photoexcitation, the transmitted THz amplitude will be reduced due to free carrier absorption. By comparing the transmitted radiation with and without photoexcitation the influence of the photoinduced carriers can be investigated. A measurement of the THz transient with and without photo-excitation is shown in Fig. 5.4. The carrier lifetime is measured by the change in the THz transmittance as a function of the arrival time of the optical pump to the THz probe. This differential transmittance is measured at the peak of the THz electric field amplitude shown in the inset in Fig. 5.4, to maximize the signal to noise. At the peak amplitude, all frequencies of the THz signal are present, covering a range from approximately 0.2 to 1 THz.

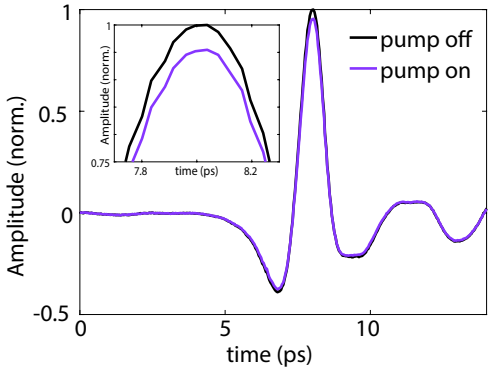

Figure 5.4: THz transient signal of the 14 nm thick WS_2 with and without photo-excitation. The inset shows a zoom-in of the difference between amplitude at the THz peak amplitude.

The differential transmittance as a function of pump delay time with an optical pump fluence of $20\mu J/cm^2$ is shown in Fig. 5.5a for the four positions on the microcrystal indicated by the matching colored dots in Fig. 5.1b. The curves show the average of

five scans and the given uncertainty is the standard deviation. These curves are fitted with a bi-exponential function, whose values are shown in table 5.1. To clearly illustrate the bi-exponential behavior Fig. 5.5b shows 1-Transmittance in a log scale. The carrier recombination dynamics vary greatly between the different thicknesses in the microcrystal. The fast decay time $\tau 1$ increases with the layer thickness from approximately 25±5 ps to 78±18 ps. For the 4-6 layers, 14 nm, and 30 nm thick layers $\tau 2$ is 148±36 ps, 258±32 ps, and 474±38 ps, respectively. The thicker layers show bi-exponential recombination due to the difference in lifetime between carriers on the surface layers compared to carriers in the inner layers. The bilayer shows a long recombination time with a small amplitude, the origin of this recombination channel is unknown.

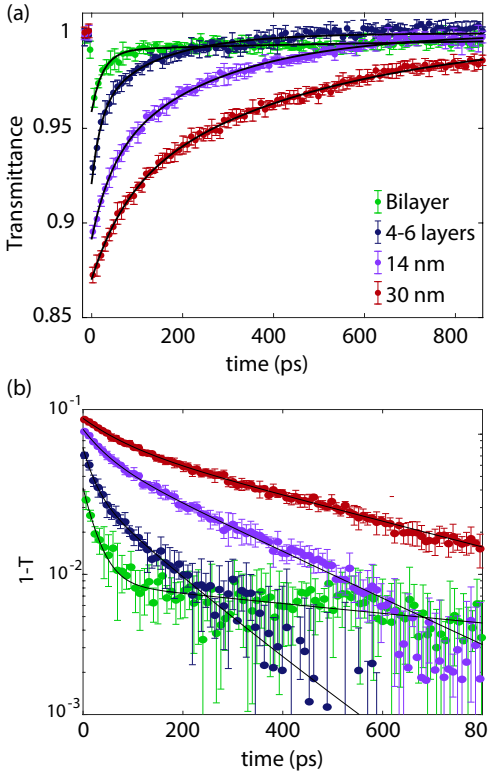

Figure 5.5: (a) Time delay measurements of the transmittance fitted with bi-exponential decays for various thicknesses on the microcrystal. (b) Time delay measurements fitted with bi-exponential decays for various thicknesses on the microcrystal with a log scale.

Carriers in thin TMD microcrystals recombine predominantly via defect-assisted Auger scattering, where electrons and holes get trapped at defects on the surface and recombine non-radiatively [157, 158]. Therefore, there are two decay channels in

the thicker layers: one for carriers generated at the surface and one for carriers that are generated in the inner layers. The decrease of $\tau 1$ in thinner layers is thus caused by a higher defect density at the surface in thinner exfoliated layers [157]. These recombination dynamics are different compared to results published for monolayer MoS2 [32, 159]. There, the lifetimes are invariant to the pump fluence, in contrast to our results as will be discussed in detail in section 4. Furthermore, the lifetime is also considerably longer in multilayers due to the change in the electronic band structure by increasing the film thickness.

Table 5.1: Fitting parameters of the biexponential carrier recombination time in photo-excited WS_2 microcrystals of different thicknesses.

Thickness	$\tau 1$ (ps)	A1 (%)	$\tau 2$ (ps)	A2 (%)
Bilayer	26±5	3.3±0.3	1400±600	0.9±0.2
4-6 layers	21±5	4.1±0.5	148±36	3.9±0.3
14 nm	44±9	3.9±0.6	258±32	7.0±0.5
30 nm	78±18	4.4±0.5	474±38	8.5±0.5

The differential transmittance as a function of pump delay time can be measured for the entire microcrystal, creating a spatial map. The carrier dynamics can be portrayed by the weighted average decay time as shown in Fig. 5.6. This weighted average decay time is defined as the sum of the two decay times normalized to their relative amplitude τ_{avg}=(τ1A1+τ2A2)/(A1+A2). Figure 5.6 clearly shows different regions of average decay times on the microcrystal. The regions coincide with the various thicknesses on the microcrystal, where the thin regions (2 to 6 layers) have a much shorter average decay time than the two thicker regions.

5.4 Power Dependent Measurements

To confirm that Auger scattering at surface defects is the dominant recombination channel of the photoinduced carriers, we perform power-dependent measurements on the three positions shown before. Auger scattering is characterized by a non-linear dependence on carrier density. [86, 157, 159] The rate equation is given by

$$\frac{dn}{dt} \approx \frac{dp}{dt} \approx -\frac{An_d Bn_d}{An_d + Bn_d} np, \tag{5.1}$$

where A and B are rate constants and n_d is the defect density. From this equation, it follows that the inverse carrier lifetime τ^{-1} scales linearly with the carrier density.

For the 14 nm thick region, the differential transmittance as a function of pump delay time is shown in Fig. 5.7a for three pump fluences. The carrier lifetime decreases considerably by increasing the pump fluence. The recombination of the transmittance at 20 μJ/cm^2 even crosses the recombination of the transmittance at 10 μJ/cm^2. The reason for this crossover is currently unknown, but a possible explanation could be the

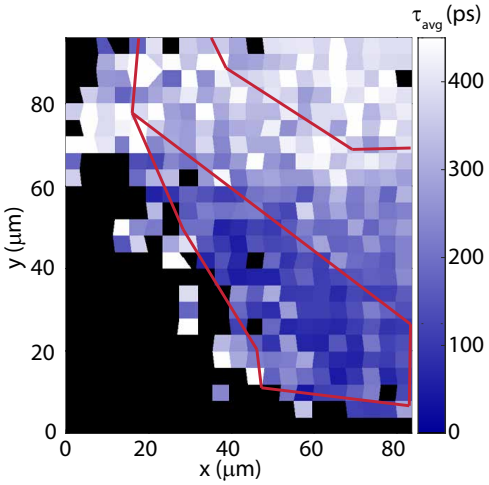

Figure 5.6: Areascan of the average carrier lifetime. The red lines indicate the boundaries of different thicknesses.

heating of the sample with the increased pump fluence. The inverse of the average carrier lifetime as a function of pump fluence is shown at the four different positions on the microcrystal in Fig. 5.7b. The 4-6 layers, 14 nm, and 30 nm positions show a clear linear relationship between the inverse carrier lifetime and the pump fluence. For the bilayer, the long decay channel with unknown origin leads to a reduced fluence dependence. The linear relationship between inverse carrier lifetime and pump fluence shows that the carrier lifetime is indeed governed by surface defect-assisted Auger scattering. We note that the offset at 0 fluence is attributed to a slight n-doping in the sample [157].

5.5 Conclusion

In conclusion, we have shown that carrier recombination in WS_2 microcrystals is dominated by Auger scattering on the surface. The carriers show a bi-exponential decay, originating from the surface and the inner layers. Time-resolved terahertz near-field microscopy is a non-invasive and high-resolution mapping technique of carrier dynamics that can scan large surfaces, opening new possibilities for the investigation of material properties of 2D semiconductors relevant to nanoelectronic and optoelectronic applications.

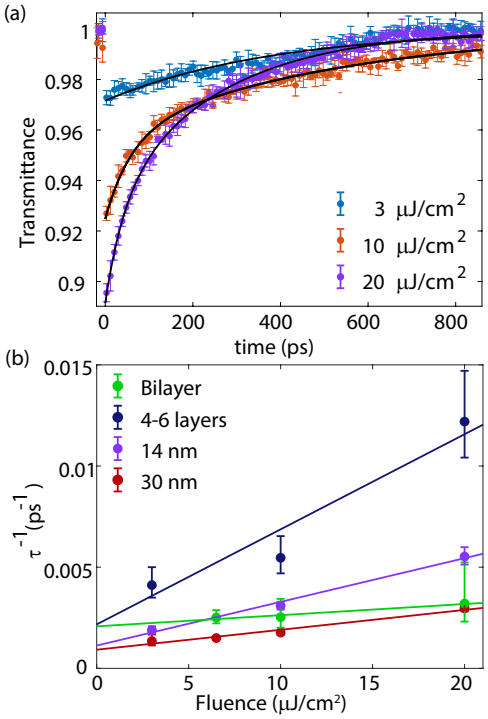

Figure 5.7: (a) Pump fluence dependent recombination dynamics for the 14 nm spot. (b) Inverse carrier lifetime as a function of pump fluence for different positions on the microcrystal.

CHAPTER 6

HIGH-FREQUENCY SHEET CONDUCTANCE OF WS_2 CRYSTALS

Time-resolved terahertz (THz) spectroscopy is a powerful technique for the determination of charge transport properties in photoexcited semiconductors. However, the relatively long wavelengths of THz radiation and the diffraction limit imposed by optical imaging systems reduce the applicability of THz spectroscopy to large samples with dimensions in the mm to cm range. Exploiting THz near-field spectroscopy, we present the first time-resolved THz measurements on a single exfoliated 2D nanolayered crystal of a transition metal dichalcogenide (WS_2). The high spatial resolution of THz near-field spectroscopy enables the mapping of the sheet conductance for an increasing number of atomic layers. The single crystalline structure of the nanolayered crystal allows for the direct observation of low-energy phonon modes, which are present in all thicknesses, coupling with free carriers. Density functional theory calculations show that the phonon mode corresponds to the breathing mode between atomic layers in the weakly bonded van der Waals layers, which can be strongly influenced by substrate-induced strain. The non-invasive and high-resolution mapping technique of carrier dynamics in nanolayered crystals by time-resolved THz time-domain spectroscopy enables possibilities for the investigation of the relation between phonons and charge transport in nanoscale semiconductors for applications in two-dimensional nanodevices.

6.1 Introduction

Transition metal dichalcogenides (TMDs) are a class of materials consisting of van der Waals stacked 2D layers with chemical formula MX_2, with M a transition-metal atom (Mo or W) and X a chalcogen atom (S, Se, or Te). The electronic band structure of TMDs changes from indirect to direct semiconductor as the dimensionality is reduced from bulk to monolayer [33], which has led to intensive research over the past years [34]. For some monolayer and few-layer TMDs the difference in exciton populations in the K- and K'-points of the hexagonal Brillouin zone leads to a new degree of freedom in charge transport and gives rise to so-called valleytronics, [156] which allows the control of electron spin by the handedness of the excitation light [35]. The quantum confinement of charges in low-dimensional TMDs leads to a very strong exciton binding energy as well, which translates into an extraordinarily high absorptance [38]. These properties make low-dimensional TMDs potentially interesting candidates for various applications in nanoelectronics and optoelectronics, such as transistors, optical switches, photodetectors, and light emission [38–41, 160]. So far, the highest quality low-dimensional TMDs are obtained by the mechanical exfoliation of nanolayered crystals from bulk material. The way these nanolayered crystals are transferred to other substrates and how the samples are further prepared have a tremendous impact on the electrical and optical properties of the nanolayered crystals [161]. Therefore, the detailed non-invasive characterization of TMDs to retrieve quantities such as carrier mobility, density or lifetime is of utmost importance for their applicability in two-dimensional nanodevices. Also, the investigation of low-energy phonon modes is of relevance since electron-phonon coupling in crystals could influence the conductance in TMDs, as has been proposed in van der Waals bound organic semiconductors [162].

A powerful technique for the investigation of charge transport in semiconductors is time-resolved terahertz (THz) spectroscopy (TRTS). This time-domain technique is capable of directly probing the frequency-dependent carrier dynamics of TMD layers non-invasively and contact-free [22, 154]. With this technique, the high-frequency conductivity of the material is probed instead of the DC conductivity that is typically retrieved using electrical contacts. However, the long wavelengths of THz radiation limit the applicability of TRTS to large samples that are grown by chemical vapor deposition, molecular beam epitaxy, atomic layer deposition, or spray-coated flakes where microscopic defects are averaged [32, 87, 153]. These grown samples have also lower quality than exfoliated nanolayered crystals, which implies that properties retrieved from the former cannot be extrapolated to the latter.

Here, we introduce time-resolved THz near-field spectroscopy to retrieve the THz sheet conductance with sub-diffraction spatial resolution. This technique allows us to perform the first THz measurements of the frequency-dependent pump-induced sheet conductance of a single exfoliated nanolayered crystal of WS_2 with varying thickness. The sheet conductance drops for all measured thicknesses and shows a specific frequency dependence. Using density functional theory, we have identified that this frequency dependence is caused by the electron-phonon coupling between charge carriers and the fundamental breathing mode in WS_2. The single crystal structure of the

exfoliated nanolayered crystal enabled us to characterize the breathing phonon mode at 0.2 THz. Furthermore, the calculations show the strong effect of strain in the crystal structure on the phonon mode, which can be associated with a substrate on which the nanolayered crystal is deposited. These results represent the first demonstration of contact-free and high-resolution THz measurements of carrier properties in exfoliated nanolayered TMDs. The coupling of low-energy phonon modes to free charges is shown and how this coupling influences the conductance of nanolayered single crystalline WS_2, affecting their applicability for two-dimensional nanodevices.

6.2 Results

6.2.1 Time-Resolved THz Near-Field Microscopy

The measurements are performed with the sub-diffraction time-resolved near-field THz microscope schematically illustrated in Fig. 5.1a (see Chapter 2 for a full description) [96]. The setup measures the local electric field amplitude with a THz near-field photoconductive antenna (microprobe detector), which has a high spatial resolution of ≃15 μm, equal to $\lambda/60$ at the wavelength of maximum amplitude. To inject charge carriers, the sample is optically excited with femtosecond optical pulses from an amplified laser system at a central wavelength of 400 nm through a Dove prism at a large angle, ensuring total internal reflection at the sample-air interface. This configuration prevents the optical pump to reach the microprobe detector. The quartz substrate is brought in optical contact with the Dove prism of the THz spectrometer using a refractive index matching liquid at optical frequencies to allow for optical excitation from the back.

6.2.2 Nanolayered WS_2 Crystal

The sample used for the experiments is the single exfoliated nanolayered crystal of tungsten disulfide, WS_2 shown in Fig. 5.1b. The colored circles indicate the positions where measurements of the photoinduced sheet conductance were performed, as discussed in the next sections. The region at the edge of the nanolayered crystal contains a large bilayer region (1.4 nm thick, green circle). Next to the bilayer, there is a thicker region of 14 nm (purple circle). The thickest region is at the top left and is approximately 30 nm thick (red circle). The thickness of the layers is determined from photoluminescence spectra for the bilayer and atomic force spectroscopy measurements for the 14 and 30 nm thick regions, see Chapter 5 for more details.

6.2.3 Photoinduced Transmittance and Sheet Conductance of Nanolayered WS_2 Crystals

A measurement of the THz transmission in the time domain, i.e., a THz transient, is shown in Fig. 6.1a for the 30-nm-thick layer (black curve). A digital truncation is introduced in the transient after 12 ps to suppress etalons originating from internal reflections in the microprobe detector and to simplify data processing. Upon photoexcitation, the

transmitted THz radiation will be reduced due to additional free-carrier absorption in the excited nanolayered crystal. By comparing the transmitted radiation with and without photo excitation, the properties of the photoinduced carriers can be investigated. The photoinduced change of the THz pulse, 20 ps after photoexcitation (incident pump fluence 20 μJ/cm^2), is presented in Fig. 6.1a for the 30-nm-thick area (red curve, multiplied 15 times for clarity). The photoinduced change in amplitude is similar in shape to the transmitted THz pulse but of the opposite sign, meaning that for the entire pulse the response due to the presence of carriers is similar.

The frequency-dependent complex transmission coefficient can be calculated by Fourier transforming the THz transient signals and normalizing the photoexcited to the non-excited measurements. The photo-induced change in transmittance (squared modulus of the complex transmission coefficient) is plotted in Fig. 6.1b as a function of frequency for the three WS_2 layer thicknesses. The measurements present a clear thickness dependence on the transmittance since in a thicker layer more photoexciting light is absorbed, generating more free carriers that attenuate the THz radiation. A sharp increase in transmittance between 0.2 and 0.4 THz is visible, after which the response becomes less frequency dependent.

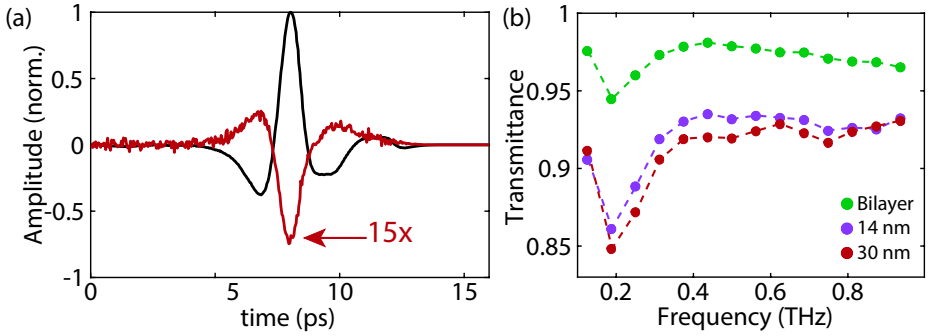

Figure 6.1: (a) Normalized electric field amplitude of a THz transient (black) and the photoinduced change of the transient upon photoexcitation (red, amplified 15 times). (b) Photo-induced change in transmittance as a function of frequency for the three measured thicknesses.

To quantify the photoinduced change on the nanolayered WS_2 crystal, the measurements need to be converted to a material parameter. Since the photoinduced change in transmittance is caused by the increase of free carriers in the material, it contributes directly to the photoinduced conductivity. The photoexcited layer can be approximated by a uniform thin film with a specified photoinduced sheet conductance because the photoexcited layer is thin compared to the THz wavelength ($h/\lambda \ll 1$). The photoinduced sheet conductance can be calculated from the complex transmission coefficient using the thin-film approximation [92, 94]

$$\tilde{\sigma_s}(\omega) = \mathrm{Re}(\sigma_s(\omega)) + \mathrm{iIm}(\sigma_s(\omega)) \simeq \frac{(n_{ref}+1)}{Z_0}\left(\frac{1}{\tilde{T}(\omega)} - 1\right), \tag{6.1}$$

here n_{ref} is the refractive index of the WS_2 layer without photoexcitation (2.28), [163] Z_0 is the impedance of free space (377 Ω) , and $\tilde{T}(\omega)$ is the photoinduced change in the complex transmission coefficient.

The real and imaginary components of the sheet conductance are depicted in Fig. 6.2a and Fig. 6.2b for the bilayer (green dots), the 14-nm (purple dots) and 30-nm (red dots) thick regions of the nanolayered crystal. Upon photoexcitation, free-carrier absorption is the dominant contribution to the reduced transmittance. Since an increased free-carrier absorption leads to a larger sheet conductance there is an inverse relation between the sheet conductance and the transmittance.

The Drude-Smith model with a Lorentzian phonon contribution is used to fit this photoinduced sheet conductance and retrieve the free-carrier properties: [164, 165]

$$\tilde{\sigma}_s(\omega) = \frac{e^2 N_s \tau_s}{m^*} \frac{1}{1 - i\omega\tau_s} \left(1 + \frac{c_1}{1 - i\omega\tau_s}\right) + \frac{S\omega}{i(\omega_0^2 - \omega^2) + \omega\gamma}, \tag{6.2}$$

where N_s is the photoinduced sheet carrier density, τ_s is the carrier scattering time, m^* is the carrier effective mass (0.4 m_e, with m_e the electron mass), [166] c_1 is the Smith contribution describing the degree of backscattering at each scattering event ($c_1 = -1$ corresponds to pure backscattering and $c_1 = 0$ to random scattering events, i.e., Drude).[29] The second term in Eq. (6.2) is a Lorentzian that characterizes a phonon contribution to the sheet conductance. In this term, S is the oscillator strength, ω_0 is the phonon frequency, and γ is the lifetime broadening parameter [29, 164].

The fits, plotted in Fig. 6.2 with dashed curves, are in excellent agreement with the data for both the real and imaginary components. The fitted parameters given in Table 6.1 show a larger photoinduced sheet carrier density with the number of layers due to increased absorption. The carrier scattering times have similar values of 100 fs, which are in agreement with values reported in bulk TMDs [164]. The backscattering contribution is ≃-1 and originates from the van der Waals stacking of WS_2 layers. This stacking suppresses free-carrier scattering between atomic layers. Furthermore, due to mechanical exfoliation, there are more defects on the surface (where the most light is absorbed) leading to an even larger backscattering contribution [157]. The phonon resonance has a frequency of around 0.2 THz, which corresponds to a breathing phonon resonance [167]. This breathing phonon mode, which we confirm with density functional theory (DFT) in the next section, is responsible for the THz sheet conductance peak that we experimentally retrieve with THz near-field microscopy.

Table 6.1: Values of the parameters from the sheet conductance fits. The uncertainty is given by the 95% confidence interval of the fit.

Thickness	N_s (cm^{-2})	τ_s (fs)	c_1	$\omega_0/2\pi$ (THz)	S (s/Ω)	$\gamma/2\pi$ (THz)
Bilayer	(0.48±0.16)10^{13}	110±23	-1±0.12	0.19±0.01	(15±6)10^4	0.16±0.05
14 nm	(1.3±0.5)10^{13}	107±26	-1±0.17	0.18±0.01	(5.5±2.5)10^4	0.19±0.06
30 nm	(2.1±0.9)10^{13}	85±35	-0.98±0.12	0.20±0.01	(3.0±1.2)10^4	0.22±0.06

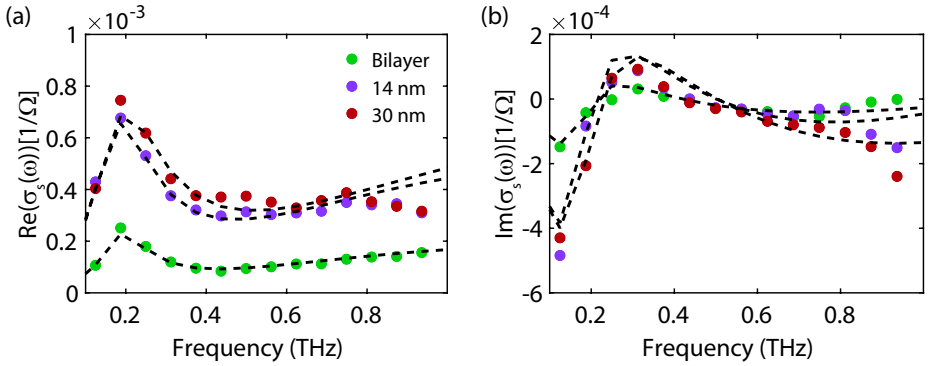

Figure 6.2: Sheet conductance fitted with the Drude-Smith model with a phonon contribution for the three measured thicknesses for the real (a) and imaginary component (b).

6.2.4 Density Functional Theory Calculations of Interlayer Phonons

The phonon modes of WS_2 bilayers were obtained from first principles self-consistent calculations with the Vienna *ab initio* Simulation Package (VASP). [168–170] The phonon energy calculations were performed using the finite displacement method within the harmonic approximation as implemented in the Phonopy package[171]. For our calculations, we adopted Projector Augmented Wave (PAW)-Perdew-Burke-Ernzerhof (PBE) exchange-correlation functionals with a $8 \times 8 \times 1$ k-point mesh in reciprocal space generated according to the Monkhorst-Pack scheme. A conventional unit cell for the 2H-polytype bilayer with two W and four S atoms (Fig. 6.3a) was used in all calculations with a plane-wave energy cutoff of 450 eV and an energy convergence criteria of 10^{-6} eV. Furthermore, we employed a $4 \times 4 \times 1$ supercell of the conventional unit cell with a vacuum spacing of 14 nm along the z axis to perform lattice relaxation and finite displacements.

A conventional unit cell for the 2H-polytype bilayer with two W and four S atoms (Fig. 6.3a) was used in all the calculations. The unit cell of the WS_2 bilayer belongs to the D_{3d} point group [172, 173]. The six atoms of the unit cell generate eighteen vibrational modes that are classified according to the irreducible representations of its point group at the Γ point, $\Gamma^{vib} = 3(A_{1g} + A_{2u} + E_g + E_u)$ where one A_{2u} and one E_u are acoustic modes, the other A_{2u} and E_u are IR active, and the A_{1g} and E_g are Raman-active associated with the out-of-plane breathing mode (blue arrows in Fig. 6.3a) and the in-plane shear mode (red arrows in Fig. 6.3a), respectively. As a consequence of the relatively weak interlayer van der Waals interactions, each layer moves almost rigidly as a whole unit giving rise to low-frequency modes corresponding to the vibrations between layers dominated by interlayer restoring forces [174]. The phonon dispersion around the Γ point for a bilayer WS_2 in a vacuum is shown in Fig. 6.3b, the A_{1g} and E_g phonon modes occur around 0.225 THz and 0.124 THz, respectively.

The calculated breathing phonon frequency of the bilayer is lower than reported in the literature with Raman spectroscopy [167]. This discrepancy can be attributed to a

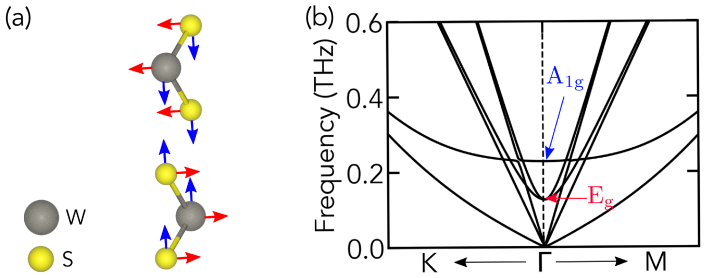

Figure 6.3: (a) Conventional unit cell of bilayer WS_2. Blue arrows indicate the relative movement between layers for the breathing mode (A_{1g}) and red arrows for the shear mode (E_g). (b) Phonon dispersion around the Γ point highlighting low-frequency breathing and shear modes for a WS_2 bilayer.

different substrate, which influences the strain in the WS_2, or to different temperatures. Upon laser excitation the temperature of the WS_2 layer increases, which reduces the phonon frequency. This temperature-dependent frequency shift has been shown for higher frequency phonons, but the reported shifts are relatively small [175]. The effect of the substrate on which the nanolayered WS_2 crystals can be deposited is considered by applying a biaxial strain in the basal xy plane through rescaling the relaxed cell vectors. Both modes increase in energy when under compressive strain (Fig. 6.4) demonstrating that strain-induced effects from a substrate can effectively change the breathing mode energy. The soft transfer technique used, in combination with leaving the WS_2 crystal on the PDMS substrate, has most likely resulted in a very small strain on the crystal and therefore a lower phonon frequency compared to the values reported earlier [161, 167].

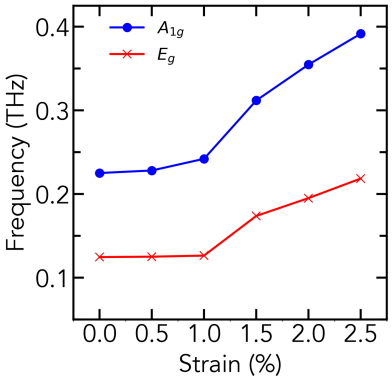

Figure 6.4: Energy of the A_{1g} and E_g phonon modes as a function of biaxial compressive strain at the Γ point.

The origin of the change in the photoinduced sheet conductance at the phonon frequency is unclear. A possible explanation could be the interaction between layers at the phonon frequency, similar to the increase observed in magnetic perovskite struc-

tures [176]. To fully describe this behavior electron-phonon matrix elements calculations would be needed.

6.3 Conclusion

Using microstructured THz photoconductive antennas and photoexcitation of an exfoliated nanolayered WS_2 crystal, we have retrieved the THz sheet conductance of a bilayer and two thicker layers of 14 and 30 nm. The measurements show a Drude-Smith conductance and coupling of the carriers to a phonon mode. DFT calculations reveal that this phonon mode corresponds to the breathing mode in the van der Waals bound semiconductor, showing a strong dependence on the strain. Time-resolved THz spectroscopy represents a viable technique for mapping transient charge transport in photoexcited samples, enabling the non-invasive investigation of nanoscale materials relevant to two-dimensional nanodevices.

CHAPTER 7

SUMMARY AND FUTURE PERSPECTIVE

Summary

Terahertz time-domain spectroscopy (THz-TDS) is a rapidly evolving technique that has gained widespread attention in recent years due to its vast potential for material characterization and for understanding the interaction between electromagnetic radiation and matter. THz-TDS is a non-invasive and contact-free method that can be used to determine the properties of charge carriers in metals and semiconductors, such as their mobility and lifetime. Additionally, THz-TDS can be used to study the time-dependent response of resonant structures, such as gold resonators, when interacting with THz radiation. This powerful method works by generating THz pulses and recording the response of the material under investigation using femtosecond time-resolved techniques. The recorded signal is then analyzed to determine the spectral content and time-domain response of the material, which provides insights into the dynamic properties of the material and the interaction between THz radiation and matter.

Despite the many benefits of THz spectroscopy, its practical application is limited by its inherently low spatial resolution, which is imposed by the diffraction limit. This limit has traditionally prevented the probing of small structures and nanoscale features. To address this limitation, two THz near-field microscopes have been developed during this work, whose spatial resolution is determined by the photo-conductive antenna dimensions. The first microscope exploits microstructured photoconductive antennas as a local source and detector, allowing for local excitation and detection in the time domain. The second microscope combines an optical pump excitation with a microstructured antenna for local detection to determine the carrier dynamics. By utilizing near-field techniques, these microscopes can probe on length scales much smaller than the diffrac-

tion limit, allowing for the investigation of resonant structures and thin films with a spatial resolution of just a few microns.

The first chapter outlines the main ideas used throughout the thesis. Chapter 2 presents the experimental setups and methods employed in the research, including the novel setups crucial for the results. Chapter 3 examines the impact of changes in the photonic surrounding on the local density of optical states near a planar interface and surrounding a gold resonator. These changes are measured in the time domain. Chapter 4 details how the electric field is tightly confined to the surface of a gold dimer array, due to the exploitation of symmetry-protected bound-states in the continuum, which fully suppresses any radiative losses. This resonance is studied in the time domain using the near-field excitation and detection microscope. Chapter 5 measures the carrier lifetime of a 2D semiconductor microcrystal with sub-diffraction resolution in the near-field and highlights the importance of precise measurements on small-length scales. The discrepancy between bulk and surface carrier lifetimes, due to defect-assisted Auger recombination, underscores the need for non-invasive techniques on micron-sized samples. Finally, chapter 6 explores the probing of photoinduced high-frequency conductance at micron-length scales and shows the effect of a breathing phonon mode on the frequency dependence of the photoinduced conductance of a 2D semiconductor microcrystal. By overcoming the limitations imposed by the diffraction limit, these THz near-field microscopes have expanded the capabilities of THz spectroscopy and paved the way for new and exciting avenues of research.

Future Perspective

In this section, we discuss possible directions in which the research could develop.

Local Density of Optical States

The results in this thesis have shown proof-of-concept measurements with a newly developed setup. The obtained measurements have been compared with analytical results as well as with simulations, showing an excellent agreement. As a follow-up, the setup can be used to measure the partial local density of optical states (PLDOS) of more complex structures like the periodic dimer array supporting bound states in the continuum, discussed in Chapter 4. Furthermore, the source and detector configuration can be changed to measure the PLDOS of the perpendicular electric field component to retrieve the LDOS given in Eq. 3.1.

Local Excitation and Detection

The local excitation and detection in the near-field and in the time-domain introduced in this thesis allow for the investigation of the excitation, propagation, and confinement of the electric field in complex photonic structures, and the determination of the cross density of states (CDOS). The CDOS is a measure of the intrinsic spatial coherence of the

structures, given by [177]

$$\rho(\mathbf{r}_0,\mathbf{r}_1,\omega)=\frac{2\omega n^2}{\pi c_0^2}\mathrm{Tr}[\,\mathrm{Im}[\overleftrightarrow{\mathbf{G}}(\mathbf{r}_0,\mathbf{r}_1,\omega)]], \tag{7.1}$$

where n is the refractive index, c_0 is the speed of light and $\overleftrightarrow{\mathbf{G}}(\mathbf{r}_0,\mathbf{r}_1,\omega)$ is the dyadic Green function, giving the field at $\mathbf{r}_1$ of a source at $\mathbf{r}_0$. The CDOS is an important quantity in the design and optimization of photonic systems. By measuring both the CDOS and the (P)LDOS the understanding of these systems can be notably extended. They complement each other since the (P)LDOS measures the number of optical states at a given location, defining the decay rate of a source at this location, while the CDOS measures the number of states connecting two points, defining the extended spatial coherence of point sources by coupling with the emission to the surrounding medium.

By locally measuring the complex electric field amplitude from a point dipole we can also detect the Förster resonance energy transfer (FRET) and the radiative energy transfer between two positions. The square of the Förster transfer amplitude $w_F(\mathbf{r}_0,\mathbf{r}_1,\omega)$ is determined by [106]

$$w_F(\mathbf{r}_0,\mathbf{r}_1,\omega)=\frac{2\pi}{\hbar^2}\left(\frac{\omega^2}{\epsilon_0 c_0^2}\right)^2|\boldsymbol{\mu}_a^*\cdot\overleftrightarrow{\mathbf{G}}_s(\mathbf{r}_0,\mathbf{r}_1,\omega)\cdot\boldsymbol{\mu}_d|^2, \tag{7.2}$$

where $\boldsymbol{\mu}_a^*$ and $\boldsymbol{\mu}_d$ are the dipole moments of the donor and acceptor and $\overleftrightarrow{\mathbf{G}}_s(\mathbf{r}_0,\mathbf{r}_1,\omega)$ is the static Green function, which corresponds to the static dipole-dipole interaction. By determining the magnitude of the Green function we can retrieve the position-dependent FRET rate and the capacity of the system to transfer energy between nearby dipoles.

With the setup that we have developed, the interaction of a single-point dipole on the surface with its surrounding can be investigated in detail in all three spatial dimensions. Interesting systems to investigate are complex photonic and plasmonic systems, such as arrays of coupled resonators, non-reciprocal systems, or topological states where the electric field can be measured while propagating at the edges.

Near-Field Material Characterization

Further developments of the time-resolved terahertz microscope into an easy-to-use tool would allow for its commercialization for material characterization at THz frequencies with micron resolution. This tool could be used in medical applications where the unique properties of THz radiation could help in medical diagnosis, as well as for quality control in the semiconductor industry. Furthermore, the ability to detect changes in the conductivity on micron length-scales with a femtosecond temporal resolution enables the non-invasive investigation of two-dimensional nanodevices.

Combining Material Properties with Photonic Structures

A combination of the two near-field setups used throughout this thesis, i.e., the double near-field THz microscope and the time-resolved near-field THz microscope, could be developed into a local excitation and detection setup with an optical pump based on total internal reflection. This new setup merges the ability to measure the local influence of resonant structures with the response of materials active in the THz frequency range. Coupling between light and matter can alter the properties of these materials, leading to new material properties. For example, an active material can be positioned at a certain height from a planar interface to investigate how the altered LDOS influences the interaction with THz radiation. Furthermore, a resonant structure can be designed to couple with the breathing phonon mode in a WS_2 2D microcrystal. Changes in this phonon mode due to the coupling with a resonant structure could improve the electrical properties of the microcrystal. Such changes can subsequently be detected by the new measurement tool.

REFERENCES

[1] A. Kwan, J. Dudley, and E. Lantz, *Who really discovered Snell's law?*, Physics World **15**, 64 (2002).

[2] K. B. Wolf and G. Krotzsch, *Geometry and dynamics in refracting systems*, European Journal of Physics **16**, 14 (1995).

[3] N. EL-BIZRI, *A Philosophical Perspective on Alhazen's Optics*, Arabic Sciences and Philosophy **15**, 189–218 (2005).

[4] I. Newton and G. Hemming, *Opticks: or, A treatise of the reflections, refractions, inflexions and colours of light : also two treatises of the species and magnitude of curvilinear figures*, Printed for Sam. Smith, and Benj. Walford, 1704.

[5] C. Huygens, *Traié de la lumiére*, Chez Pierre vander Aa, marchand libraire, A Leide, 1690.

[6] T. Young, *The Bakerian Lecture: On the Theory of Light and Colours*, Philosophical Transactions of the Royal Society of London Series I **92**, 12 (1802).

[7] H. Crew, C. Huygens, T. Young, A. J. Fresnel, and F. Arago, *The wave theory of light; memoirs of Huygens, Young and Fresnel*, Cincinnati American Book Company, 1900.

[8] D. Sengupta and T. Sarkar, *Maxwell, Hertz, the Maxwellians, and the early history of electromagnetic waves*, IEEE Antennas and Propagation Magazine **45**, 13 (2003).

[9] J. C. Maxwell, *A Dynamical Theory of the Electromagnetic Field*, Philosophical Transactions of the Royal Society of London **155**, 459 (1865).

[10] J. D. Jackson, *Classical electrodynamics*, John Wiley & Sons, 2007.

[11] H. Hertz, *Ueber einen Einfluss des ultravioletten Lichtes auf die electrische Entladung*, Annalen der Physik **267**, 983 (1887).

[12] J. Fraunhofer, *Bestimmung des Brechungs- und des Farbenzerstreungs-Vermögens verschiedener Glasarten, in Bezug auf die Vervollkommnung achromatischer Fernröhre*, Annalen der Physik **56**, 264 (1817).

[13] Y.-S. Lee, *Principles of terahertz science and technology*, volume 170, Springer Science & Business Media, 2009.

[14] M. Brucherseifer, M. Nagel, P. Haring Bolivar, H. Kurz, A. Bosserhoff, and R. Büttner, *Label-free probing of the binding state of DNA by time-domain terahertz sensing*, Applied Physics Letters **77**, 4049 (2000).

[15] Z. D. Taylor et al., *THz medical imaging: in vivo hydration sensing*, IEEE transactions on terahertz science and technology **1**, 201 (2011).

[16] K. Ajito and Y. Ueno, *THz chemical imaging for biological applications*, IEEE Transactions on Terahertz Science and Technology **1**, 293 (2011).

[17] J. F. Federici, B. Schulkin, F. Huang, D. Gary, R. Barat, F. Oliveira, and D. Zimdars, *THz imaging and sensing for security applications—explosives, weapons and drugs*, Semiconductor Science and Technology **20**, S266 (2005).

[18] T. Kürner and S. Priebe, *Towards THz communications-status in research, standardization and regulation*, Journal of Infrared, Millimeter, and Terahertz Waves **35**, 53 (2014).

[19] C. Sirtori, *Applied physics: Bridge for the terahertz gap*, Nature **417**, 132 (2002).

[20] G. P. Williams, *Filling the THz gap—high power sources and applications*, Reports on Progress in Physics **69**, 301 (2005).

[21] M. Tonouchi, *Cutting-edge terahertz technology*, Nature photonics **1**, 97 (2007).

[22] M. C. Beard, G. M. Turner, and C. A. Schmuttenmaer, *Transient photoconductivity in GaAs as measured by time-resolved terahertz spectroscopy*, Nano Letters **2**, 983 (2000).

[23] D. G. Cooke, A. N. MacDonald, A. Hryciw, J. Wang, Q. Li, A. Meldrum, and F. A. Hegmann, *Transient terahertz conductivity in photoexcited silicon nanocrystal films*, Physical Review B - Condensed Matter and Materials Physics **73**, 1 (2006).

[24] P. R. Whelan, K. Iwaszczuk, R. Wang, S. Hofmann, P. Bøggild, and P. U. Jepsen, *Robust mapping of electrical properties of graphene from terahertz time-domain spectroscopy with timing jitter correction*, Optics Express **25**, 2725 (2017).

[25] H. J. Joyce, J. L. Boland, C. L. Davies, S. A. Baig, and M. B. Johnston, *A review of the electrical properties of semiconductor nanowires: Insights gained from terahertz conductivity spectroscopy*, Semiconductor Science and Technology **31** (2016).

[26] C. He, L. Zhu, Q. Zhao, Y. Huang, Z. Yao, W. Du, Y. He, S. Zhang, X. Xu, C. He, L. Zhu, Q. Zhao, Y. Huang, Z. Yao, W. Du, Y. He, S. Zhang, X. S. Xu Joint, and X. Xu, *FULL PAPER 1800290 (1 of 8) Competition between Free Carriers and Excitons Mediated by Defects Observed in Layered WSe 2 Crystal with Time-Resolved Terahertz Spectroscopy*, (2018).

[27] H. Liu, X. He, J. Ren, J. Jiang, Y. Yao, and G. Lu, *Terahertz Modulation and Ultrafast Characteristic of Two-Dimensional Lead Halide Perovskites*, Nanomaterials **12** (2022).

[28] P. Drude, *Zur Elektronentheorie der Metalle,* Annalen der Physik **306**, 566 (1900).

[29] R. Ulbricht, E. Hendry, J. Shan, T. F. Heinz, and M. Bonn, *Carrier dynamics in semiconductors studied with time-resolved terahertz spectroscopy*, Reviews of Modern Physics (2011).

[30] T. L. Cocker, D. Baillie, M. Buruma, L. V. Titova, R. D. Sydora, F. Marsiglio, and F. A. Hegmann, *Microscopic origin of the Drude-Smith model*, Physical Review B **96** (2017).

[31] F. Kadlec, C. Kadlec, and P. Kužel, *Contrast in terahertz conductivity of phase-change materials*, Solid State Communications **152**, 852 (2012).

[32] C. J. Docherty, P. Parkinson, H. J. Joyce, M. H. Chiu, C. H. Chen, M. Y. Lee, L. J. Li, L. M. Herz, and M. B. Johnston, *Ultrafast transient terahertz conductivity of monolayer MoS2and WSe2 grown by chemical vapor deposition*, ACS Nano (2014).

[33] K. F. Mak, C. Lee, J. Hone, J. Shan, and T. F. Heinz, *Atomically thin MoS2: A new direct-gap semiconductor*, Physical Review Letters **105**, 2 (2010).

[34] W. Choi, N. Choudhary, G. H. Han, J. Park, D. Akinwande, and Y. H. Lee, *Recent development of two-dimensional transition metal dichalcogenides and their applications*, Materials Today **20**, 116 (2017).

[35] J. R. Schaibley, H. Yu, G. Clark, P. Rivera, J. S. Ross, K. L. Seyler, W. Yao, and X. Xu, *Valleytronics in 2D materials*, Nature Reviews Materials **1** (2016).

[36] M. Onga, Y. Zhang, T. Ideue, and Y. Iwasa, *Exciton Hall effect in monolayer MoS 2*, Nature Materials **16**, 1193 (2017).

[37] R. Cheng, D. Li, H. Zhou, C. Wang, A. Yin, S. Jiang, Y. Liu, Y. Chen, Y. Huang, and X. Duan, *Electroluminescence and photocurrent generation from atomically sharp WSe2/MoS2 heterojunction p-n diodes*, Nano Letters **14**, 5590 (2014).

[38] M. Bernardi, M. Palummo, and J. C. Grossman, *Extraordinary sunlight absorption and one nanometer thick photovoltaics using two-dimensional monolayer materials*, Nano Letters **13**, 3664 (2013).

[39] E. G. Marin, D. Marian, M. Perucchini, G. Fiori, and G. Iannaccone, *Lateral Heterostructure Field-Effect Transistors Based on Two-Dimensional Material Stacks with Varying Thickness and Energy Filtering Source*, ACS Nano **14**, 1982 (2020).

[40] D.-S. Tsai, K.-K. Liu, D.-H. Lien, M.-L. Tsai, C.-F. Kang, C.-A. Lin, L.-J. Li, and J.-H. He, *Few-Layer MoS_2 with High Broadband Photogain and Fast Optical Switching for Use in Harsh Environments*, ACS Nano **7**, 3905 (2013), PMID: 23590667.

[41] D. Kufer and G. Konstantatos, *Highly Sensitive, Encapsulated MoS_2 Photodetector with Gate Controllable Gain and Speed*, Nano Letters **15**, 7307 (2015), PMID: 26501356.

[42] S. Eizagirre Barker, S. Wang, R. H. Godiksen, G. W. Castellanos, M. Berghuis, T. V. Raziman, A. G. Curto, and J. Gómez Rivas, *Preserving the Emission Lifetime and Efficiency of a Monolayer Semiconductor upon Transfer*, Advanced Optical Materials **7** (2019).

[43] P. Biagioni, J.-S. Huang, and B. Hecht, *Nanoantennas for visible and infrared radiation*, Reports on Progress in Physics **75**, 024402 (2012).

[44] P. Zijlstra, M. Orrit, and A. F. Koenderink, *Metal nanoparticles for microscopy and spectroscopy*, in *Nanoparticles*, pages 53–98, Springer, 2014.

[45] R. W. Wood, *XLII. On a remarkable case of uneven distribution of light in a diffraction grating spectrum*, The London, Edinburgh, and Dublin Philosophical Magazine and Journal of Science **4**, 396 (1902).

[46] L. Rayleigh, *On the dynamical theory of gratings*, Proceedings of the Royal Society of London. Series A, Containing Papers of a Mathematical and Physical Character **79**, 399 (1907).

[47] L. Rayleigh, *III. Note on the remarkable case of diffraction spectra described by Prof. Wood*, The London, Edinburgh, and Dublin Philosophical Magazine and Journal of Science **14**, 60 (1907).

[48] A. A. Darweesh, S. J. Bauman, D. T. Debu, and J. B. Herzog, *The Role of Rayleigh-Wood Anomalies and Surface Plasmons in Optical Enhancement for Nano-Gratings*, Nanomaterials **8** (2018).

[49] G. Pirruccio, *Coherent absorption in weakly absorbing layers*, PhD thesis (Eindhoven University of Technology, 2014).

[50] M. C. Schaafsma, *Thz resonances in semiconductor structures*, PhD thesis (Eindhoven University of Technology, 2015).

[51] E. M. Hicks, S. Zou, G. C. Schatz, K. G. Spears, R. P. Van Duyne, L. Gunnarsson, T. Rindzevicius, B. Kasemo, and M. Käll, *Controlling plasmon line shapes through diffractive coupling in linear arrays of cylindrical nanoparticles fabricated by electron beam lithography*, Nano letters **5**, 1065 (2005).

[52] M. C. Schaafsma, A. Bhattacharya, and J. G. Rivas, *Diffraction Enhanced Transparency and Slow THz Light in Periodic Arrays of Detuned and Displaced Dipoles*, ACS Photonics (2016).

[53] J. von Neuman and E. Wigner, *Uber merkwürdige diskrete Eigenwerte. Uber das Verhalten von Eigenwerten bei adiabatischen Prozessen*, Physikalische Zeitschrift **30**, 467 (1929).

[54] C. W. Hsu, B. Zhen, A. D. Stone, J. D. Joannopoulos, and M. Soljacic, *Bound states in the continuum*, 2016.

[55] K. Koshelev, S. Lepeshov, M. Liu, A. Bogdanov, and Y. Kivshar, *Asymmetric Metasurfaces with High- Q Resonances Governed by Bound States in the Continuum*, Physical Review Letters **121**, 193903 (2018).

[56] D. R. Abujetas, N. van Hoof, S. ter Huurne, J. Gómez Rivas, and J. A. Sánchez-Gil, *Spectral and temporal evidence of robust photonic bound states in the continuum on terahertz metasurfaces*, Optica **6**, 996 (2019).

[57] N. J. van Hoof, D. R. Abujetas, S. E. ter Huurne, F. Verdelli, G. C. Timmermans, J. A. Sánchez-Gil, and J. G. Rivas, *Unveiling the Symmetry Protection of Bound States in the Continuum with Terahertz Near-Field Imaging*, ACS Photonics (2021).

[58] W. L. Barnes, S. A. Horsley, and W. L. Vos, *Classical antennas, quantum emitters, and densities of optical states*, Journal of Optics (United Kingdom) **22**, 73501 (2020).

[59] L. Novotny and B. Hecht, *Principles of Nano-Optics*, Cambridge University Press, 2 edition, 2012.

[60] E. Abbe, *Beiträge zur Theorie des Mikroskops und der mikroskopischen Wahrnehmung: II. Die dioptrischen Bedingungen der Leistung des Mikroskops*, Archiv für mikroskopische Anatomie **9**, 418 (1873).

[61] E. Synge, *XXXVIII. A suggested method for extending microscopic resolution into the ultra-microscopic region*, The London, Edinburgh, and Dublin Philosophical Magazine and Journal of Science **6**, 356 (1928).

[62] E. Ash and G. Nicholls, *Super-resolution aperture scanning microscope*, Nature **237**, 510 (1972).

[63] W. D. Pohl, *Optical near-field scanning microscope*, 1986, US Patent 4,604,520.

[64] O. Mitrofanov, I. Brener, R. Harel, J. Wynn, L. Pfeiffer, K. West, and J. Federici, *Terahertz near-field microscopy based on a collection mode detector*, Applied Physics Letters **77**, 3496 (2000).

[65] N. N. Zinov'ev, A. V. Andrianov, A. Gallant, J. Chamberlain, and V. Trukhin, *Contrast and resolution enhancement in a confocal terahertz video system.*, JETP letters **88** (2008).

[66] A. J. L. Adam, *Review of near-field terahertz measurement methods and their applications*, Journal of Infrared, Millimeter, and Terahertz Waves **32**, 976 (2011).

[67] A. J. Macfaden, J. L. Reno, I. Brener, and O. Mitrofanov, *3 μ m aperture probes for near-field terahertz transmission microscopy*, Applied Physics Letters **104**, 011110 (2014).

[68] Q. Chen and X.-C. Zhang, *Semiconductor dynamic aperture for near-field terahertz wave imaging*, IEEE Journal of selected topics in quantum electronics **7**, 608 (2001).

[69] N. Van der Valk and P. Planken, *Electro-optic detection of subwavelength terahertz spot sizes in the near field of a metal tip*, Applied Physics Letters **81**, 1558 (2002).

[70] H.-T. Chen, R. Kersting, and G. C. Cho, *Terahertz imaging with nanometer resolution*, Applied Physics Letters **83**, 3009 (2003).

[71] A. J. Huber, F. Keilmann, J. Wittborn, J. Aizpurua, and R. Hillenbrand, *Terahertz near-field nanoscopy of mobile carriers in single semiconductor nanodevices*, Nano letters **8**, 3766 (2008).

[72] T. L. Cocker, V. Jelic, M. Gupta, S. J. Molesky, J. A. Burgess, G. D. L. Reyes, L. V. Titova, Y. Y. Tsui, M. R. Freeman, and F. A. Hegmann, *An ultrafast terahertz scanning tunnelling microscope*, Nature Photonics **7**, 620 (2013).

[73] R. Lecaque, S. Grésillon, N. Barbey, R. Peretti, J.-C. Rivoal, and C. Boccara, *THz near-field optical imaging by a local source*, Optics communications **262**, 125 (2006).

[74] A. Gürtler, C. Winnewisser, H. Helm, and P. U. Jepsen, *Terahertz pulse propagation in the near field and the far field*, JOSA A **17**, 74 (2000).

[75] M. Wächter, M. Nagel, and H. Kurz, *Tapered photoconductive terahertz field probe tip with subwavelength spatial resolution*, Applied Physics Letters **95**, 041112 (2009).

[76] A. Bhattacharya and J. Gómez Rivas, *Full vectorial mapping of the complex electric near-fields of THz resonators*, APL Photonics **1** (2016).

[77] V. Apostolopoulos and M. Barnes, *THz emitters based on the photo-Dember effect*, Journal of Physics D: Applied Physics **47**, 374002 (2014).

[78] M. Ashida, *Ultra-broadband terahertz wave detection using photoconductive antenna*, Japanese Journal of Applied Physics **47**, 8221 (2008).

[79] F. D'Angelo, Z. Mics, M. Bonn, and D. Turchinovich, *Ultra-broadband THz time-domain spectroscopy of common polymers using THz air photonics*, Optics express **22**, 12475 (2014).

[80] T.-I. Jeon and D. Grischkowsky, *Characterization of optically dense, doped semiconductors by reflection THz time domain spectroscopy*, Applied Physics Letters **72**, 3032 (1998).

[81] M. Walther, P. Plochocka, B. Fischer, H. Helm, and P. Uhd Jepsen, *Collective vibrational modes in biological molecules investigated by terahertz time-domain spectroscopy*, Biopolymers **67**, 310 (2002).

[82] M. Scheller, *Data extraction from terahertz time domain spectroscopy measurements*, 2014.

[83] P. a. George, J. Strait, J. Dawlaty, S. Shivaraman, M. Chandrashekhar, F. Rana, and M. G. Spencer, *Spectroscopy of the Carrier Relaxation Epitaxial Graphene*, Nano letters **8**, 17 (2008).

[84] M. Breusing, S. Kuehn, T. Winzer, E. Malić, F. Milde, N. Severin, J. P. Rabe, C. Ropers, A. Knorr, and T. Elsaesser, *Ultrafast nonequilibrium carrier dynamics in a single graphene layer*, Physical Review B - Condensed Matter and Materials Physics **83**, 1 (2011).

[85] D. Brida, A. Tomadin, C. Manzoni, Y. J. Kim, A. Lombardo, S. Milana, R. R. Nair, K. S. Novoselov, A. C. Ferrari, G. Cerullo, and M. Polini, *Ultrafast collinear scattering and carrier multiplication in graphene*, Nature Communications **4** (2013).

[86] S. Kar, Y. Su, R. R. Nair, and A. K. Sood, *Probing Photoexcited Carriers in a Few-Layer MoS2Laminate by Time-Resolved Optical Pump-Terahertz Probe Spectroscopy*, ACS Nano (2015).

[87] P. D. Cunningham, K. M. McCreary, A. T. Hanbicki, M. Currie, B. T. Jonker, and L. M. Hayden, *Charge Trapping and Exciton Dynamics in Large-Area CVD Grown MoS2*, Journal of Physical Chemistry C **120**, 5819 (2016).

[88] S. Xu, J. Yang, H. Jiang, F. Su, and Z. Zeng, *Transient photoconductivity and free carrier dynamics in a monolayer WS2 probed by time resolved Terahertz spectroscopy*, Nanotechnology **30** (2019).

[89] A. Burgos-Caminal, E. Socie, M. E. Bouduban, and J. E. Moser, *Exciton and Carrier Dynamics in Two-Dimensional Perovskites*, Journal of Physical Chemistry Letters **11**, 7692 (2020).

[90] L. Viti, D. G. Purdie, A. Lombardo, A. C. Ferrari, and M. S. Vitiello, *HBN-Encapsulated, Graphene-based, Room-temperature Terahertz Receivers, with High Speed and Low Noise*, Nano Letters **20**, 3169 (2020).

[91] M. C. Beard, G. M. Turner, and C. A. Schmuttenmaer, *Terahertz spectroscopy*, Journal of Physical Chemistry B (2002).

[92] M. Tinkham, *Energy gap interpretation of experiments on infrared transmission through superconducting films*, Physical Review **104**, 845 (1956).

[93] S. Kar, D. R. Mohapatra, E. Freysz, and A. K. Sood, *Tuning photoinduced terahertz conductivity in monolayer graphene: Optical-pump terahertz-probe spectroscopy*, Physical Review B **90**, 165420 (2014).

[94] J. Neu, K. P. Regan, J. R. Swierk, and C. A. Schmuttenmaer, *Applicability of the thin-film approximation in terahertz photoconductivity measurements*, Applied Physics Letters **113**, 233901 (2018).

[95] K. Iwaszczuk, D. G. Cooke, M. Fujiwara, H. Hashimoto, P. Uhd Jepsen, D. G. Cooke, A. N. Macdonald, A. Hryciw, J. Wang, Q. Li, A. Meldrum, and F. A. Hegmann, *Simultaneous reference and differential waveform acquisition in time-resolved terahertz spectroscopy*, Optics Express **17**, 21969 (2009).

[96] N. J. J. van Hoof, S. E. T. ter Huurne, J. G. Rivas, and A. Halpin, *Time-resolved terahertz time-domain near-field microscopy*, Optics Express **26**, 32118 (2018).

[97] P. A. M. Dirac, *The quantum theory of the emission and absorption of radiation*, Proceedings of the Royal Society of London. Series A, Containing Papers of a Mathematical and Physical Character **114**, 243 (1927).

[98] E. Fermi, *Nuclear physics: a course given by Enrico Fermi at the University of Chicago*, University of Chicago Press, 1950.

[99] J.-M. Zhang and Y. Liu, *Fermi's golden rule: its derivation and breakdown by an ideal model*, European Journal of Physics **37**, 065406 (2016).

[100] E. M. Purcell, *Spontaneous emission probabilities at radio frequencies*, Phys. Rev. **69**, 681 (1946).

[101] A. E. Krasnok, A. P. Slobozhanyuk, C. R. Simovski, S. A. Tretyakov, A. N. Poddubny, A. E. Miroshnichenko, Y. S. Kivshar, and P. A. Belov, *An antenna model for the Purcell effect*, Scientific reports **5**, 1 (2015).

[102] P. Andrew and W. L. Barnes, *Förster Energy Transfer in an Optical Microcavity*, Science **290**, 785 (2000).

[103] C. Deeb, Z. Guo, A. Yang, L. Huang, and T. W. Odom, *Correlating Nanoscopic Energy Transfer and Far-Field Emission to Unravel Lasing Dynamics in Plasmonic Nanocavity Arrays*, Nano Letters **18**, 1454 (2018), PMID: 29369639.

[104] I. Silveiro, A. Manjavacas, S. Thongrattanasiri, and F. G. De Abajo, *Plasmonic energy transfer in periodically doped graphene*, New Journal of Physics **15**, 033042 (2013).

[105] C. Blum, N. Zijlstra, A. Lagendijk, M. Wubs, A. P. Mosk, V. Subramaniam, and W. L. Vos, *Nanophotonic Control of the Förster Resonance Energy Transfer Efficiency*, Phys. Rev. Lett. **109**, 203601 (2012).

[106] M. Wubs and W. L. Vos, *Förster resonance energy transfer rate in any dielectric nanophotonic medium with weak dispersion*, New journal of physics **18**, 053037 (2016).

[107] G. Alber, J. Z. Bernád, M. Stobińska, L. L. Sánchez-Soto, and G. Leuchs, *QED with a parabolic mirror*, Phys. Rev. A **88**, 023825 (2013).

[108] G. Lozano, D. J. Louwers, S. R. Rodríguez, S. Murai, O. T. Jansen, M. A. Verschuuren, and J. Gómez Rivas, *Plasmonics for solid-state lighting: Enhanced excitation and directional emission of highly efficient light sources*, Light: Science and Applications **2** (2013).

[109] W. L. Barnes, G. Björk, J. M. Gérard, P. Jonsson, J. A. Wasey, P. T. Worthing, and V. Zwiller, *Solid-state single photon sources: Light collection strategies*, European Physical Journal D **18**, 197 (2002).

[110] I. C. Hoi, A. F. Kockum, L. Tornberg, A. Pourkabirian, G. Johansson, P. Delsing, and C. M. Wilson, *Probing the quantum vacuum with an artificial atom in front of a mirror*, Nature Physics **11**, 1045 (2015).

[111] M. A. Othman, F. Yazdi, A. Figotin, and F. Capolino, *Giant gain enhancement in photonic crystals with a degenerate band edge*, Physical Review B **93**, 024301 (2016).

[112] J. F. Galisteo-López and G. Lozano, *Nanophotonics for current and future white light-emitting devices*, Journal of Applied Physics **130**, 200901 (2021).

[113] R. Saive, *Light trapping in thin silicon solar cells: A review on fundamentals and technologies*, Progress in Photovoltaics: Research and Applications **29**, 1125 (2021).

[114] L. Langguth, R. Fleury, A. Alù, and A. F. Koenderink, *Drexhage's Experiment for Sound*, Phys. Rev. Lett. **116**, 224301 (2016).

[115] T. Ohtsuki, H. Yuki, M. Muto, J. Kasagi, and K. Ohno, *Enhanced Electron-Capture Decay Rate of* ^{7}Be *Encapsulated in* C_{60} *Cages*, Phys. Rev. Lett. **93**, 112501 (2004).

[116] M. T. Reid and S. G. Johnson, *Efficient Computation of Power, Force, and Torque in BEM Scattering Calculations*, IEEE Transactions on Antennas and Propagation **63**, 3588 (2015).

[117] `http://github.com/homerreid/scuff-EM`.

[118] K. H. Drexhage, *Influence of a dielectric interface on fluorescence decay time*, Journal of Luminescence **1-2**, 693 (1970).

[119] M. Naftaly and R. Miles, *Terahertz time-domain spectroscopy of silicate glasses and the relationship to material properties*, Journal of Applied Physics **102**, 043517 (2007).

[120] V. Giannini, A. I. Fernández-Domínguez, Y. Sonnefraud, T. Roschuk, R. Fernández-García, and S. A. Maier, *Controlling light localization and light-matter interactions with nanoplasmonics*, Small **6**, 2498 (2010).

[121] J. G. Rivas, C. Janke, P. H. Bolivar, and H. Kurz, *Transmission of THz radiation through InSb gratings of subwavelength apertures*, Opt. Express **13**, 847 (2005).

[122] A. Bhattacharya, G. Georgiou, S. Sawallich, C. Matheisen, M. Nagel, and J. Gómez Rivas, *Large near-to-far field spectral shifts for terahertz resonances*, Phys. Rev. B **93**, 035438 (2016).

[123] S. A. Maier and H. A. Atwater, *Plasmonics: Localization and guiding of electromagnetic energy in metal/dielectric structures*, Journal of Applied Physics **98** (2005).

[124] D. N. Basov, M. M. Fogler, and F. J. García De Abajo, *Polaritons in van der Waals materials*, Science **354** (2016).

[125] T. I. Jeon and D. Grischkowsky, *THz Zenneck surface wave (THz surface plasmon) propagation on a metal sheet*, Applied Physics Letters **88**, 1 (2006).

[126] J. B. Pendry, L. Martín-Moreno, and F. J. Garcia-Vidal, *Mimicking surface plasmons with structured surfaces*, Science **305**, 847 (2004).

[127] C. R. Williams, S. R. Andrews, S. A. Maier, A. I. Fernández-Domínguez, L. Martín-Moreno, and F. J. García-Vidal, *Highly confined guiding of terahertz surface plasmon polaritons on structured metal surfaces*, Nature Photonics **2**, 175 (2008).

[128] W. L. Barnes, A. Dereux, and T. W. Ebbesen, *Surface plasmon subwavelength optics*, Nature **424**, 824 (2003).

[129] P. Lalanne, C. Sauvan, and J. P. Hugonin, *Photon confinement in photonic crystal nanocavities*, Laser and Photonics Reviews **2**, 514 (2008).

[130] P. Bharadwaj, B. Deutsch, and L. Novotny, *Optical Antennas*, Advances in Optics and Photonics **1**, 438 (2009).

[131] N. J. Halas, S. Lal, W. S. Chang, S. Link, and P. Nordlander, *Plasmons in strongly coupled metallic nanostructures*, Chemical Reviews **111**, 3913 (2011).

[132] P. Mühlschlegel, H.-J. Eisler, O. J. F. Martin, B. Hecht, and D. Pohl, *Resonant optical antennas*, Science **308**, 1607 (2005).

[133] D. A. Iranzo, S. Nanot, E. J. Dias, I. Epstein, C. Peng, D. K. Efetov, M. B. Lundeberg, R. Parret, J. Osmond, J. Y. Hong, J. Kong, D. R. Englund, N. M. Peres, and F. H. Koppens, *Probing the ultimate plasmon confinement limits with a van der Waals heterostructure*, Science **360**, 291 (2018).

[134] P. Zijlstra, P. M. Paulo, and M. Orrit, *Optical detection of single non-absorbing molecules using the surface plasmon resonance of a gold nanorod*, Nature Nanotechnology **7**, 379 (2012).

[135] R. Chikkaraddy, B. De Nijs, F. Benz, S. J. Barrow, O. A. Scherman, E. Rosta, A. Demetriadou, P. Fox, O. Hess, and J. J. Baumberg, *Single-molecule strong coupling at room temperature in plasmonic nanocavities*, Nature **535**, 127 (2016).

[136] V. G. Kravets, A. V. Kabashin, W. L. Barnes, and A. N. Grigorenko, *Plasmonic Surface Lattice Resonances: A Review of Properties and Applications*, Chemical Reviews **118**, 5912 (2018).

[137] W. Wang, M. Ramezani, A. I. Väkeväinen, P. Törmä, J. G. Rivas, and T. W. Odom, *The rich photonic world of plasmonic nanoparticle arrays*, Materials Today **21**, 303 (2018).

[138] A. Manjavacas, L. Zundel, and S. Sanders, *Analysis of the Limits of the Near-Field Produced by Nanoparticle Arrays*, ACS Nano **13**, 10682 (2019).

[139] T. C. W. Tan, E. Plum, and R. Singh, *Surface lattice resonances in THz metamaterials*, Photonics **6** (2019).

[140] A. D. Utyushev, V. I. Zakomirnyi, and I. L. Rasskazov, *Collective lattice resonances: Plasmonics and beyond*, Reviews in Physics **6**, 100051 (2021).

[141] D. C. Marinica, A. G. Borisov, and S. V. Shabanov, *Bound states in the continuum in photonics*, Physical Review Letters (2008).

[142] K. L. Koshelev, S. K. Sychev, Z. F. Sadrieva, A. A. Bogdanov, and I. V. Iorsh, *Strong coupling between excitons in transition metal dichalcogenides and optical bound states in the continuum*, Physical Review B **98**, 161113 (2018).

[143] A. Tittl, A. Leitis, M. Liu, F. Yesilkoy, D. Y. Choi, D. N. Neshev, Y. S. Kivshar, and H. Altug, *Imaging-based molecular barcoding with pixelated dielectric metasurfaces*, Science **360**, 1105 (2018).

[144] A. Kodigala, T. Lepetit, Q. Gu, B. Bahari, Y. Fainman, and B. Kanté, *Lasing action from photonic bound states in continuum*, Nature **541**, 196 (2017).

[145] S. T. Ha, Y. H. Fu, N. K. Emani, Z. Pan, R. M. Bakker, R. Paniagua-Domínguez, and A. I. Kuznetsov, *Directional lasing in resonant semiconductor nanoantenna arrays*, Nature Nanotechnology **13**, 1042 (2018).

[146] J. M. Foley, S. M. Young, and J. D. Phillips, *Symmetry-protected mode coupling near normal incidence for narrow-band transmission filtering in a dielectric grating*, Physical Review B - Condensed Matter and Materials Physics **89**, 1 (2014).

[147] H. M. Doeleman, F. Monticone, W. Den Hollander, A. Alù, and A. F. Koenderink, *Experimental observation of a polarization vortex at an optical bound state in the continuum*, Nature Photonics **12**, 397 (2018).

[148] Z. Dong, Z. Mahfoud, R. Paniagua-Domínguez, H. Wang, A. I. Fernández-Domínguez, S. Gorelik, S. T. Ha, F. Tjiptoharsono, A. I. Kuznetsov, M. Bosman, and J. K. W. Yang, *Photonic Bound-States-in-the-Continuum Observed with an Electron Nanoprobe*, (2021).

[149] D. R. Abujetas, J. A. Sánchez-gil, and J. J. Sáenz, *Generalized Brewster effect in high-refractive-index nanorod-based metasurfaces*, Optics Express **26**, 31523 (2018).

[150] D. R. Abujetas, J. Olmos-Trigo, J. J. Sáenz, and J. A. Sánchez-Gil, *Coupled electric and magnetic dipole formulation for planar arrays of particles: Resonances and bound states in the continuum for all-dielectric metasurfaces*, Physical Review B **102**, 125411 (2020).

[151] D. R. Abujetas and J. A. Sánchez-Gil, *Near-field excitation of bound states in the continuum in all-dielectric metasurfaces through a coupled electric/magnetic dipole model*, Nanomaterials **11** (2021).

[152] T. C. Tan, E. Plum, and R. Singh, *Lattice-Enhanced Fano Resonances from Bound States in the Continuum Metasurfaces*, Advanced Optical Materials **8**, 1901572 (2020).

[153] M. Bala Murali Krishna, J. Madéo, J. P. Urquizo, X. Zhu, S. Vinod, C. S. Tiwary, P. M. Ajayan, and K. M. Dani, *Terahertz photoconductivity and photocarrier dynamics in few-layer hBN/WS2 van der Waals heterostructure laminates*, Semiconductor Science and Technology **33** (2018).

[154] P. U. Jepsen, D. G. Cooke, and M. Koch, *Terahertz spectroscopy and imaging - Modern techniques and applications*, Laser and Photonics Reviews (2011).

[155] Y. Li, X. Li, T. Yu, G. Yang, H. Chen, C. Zhang, Q. Feng, J. Ma, W. Liu, H. Xu, Y. Liu, and X. Liu, *Accurate identification of layer number for few-layer WS_2 and WSe_2 via spectroscopic study*, Nanotechnology **29**, 124001 (2018).

[156] R. H. Godiksen, S. Wang, T. V. Raziman, J. G. Rivas, and A. G. Curto, *Contrast in spin-valley polarization due to competing indirect transitions in few-layer WS_2 and WSe_2*, page 1 (2020).

[157] H. Wang, C. Zhang, and F. Rana, *Surface Recombination Limited Lifetimes of Photoexcited Carriers in Few-Layer Transition Metal Dichalcogenide MoS2*, Nano Letters (2015).

[158] Y. Liu, H. Liu, J. Wang, and D. Liu, *Defect-Type-Dependent Carrier Lifetimes in Monolayer WS2Films*, Journal of Physical Chemistry C **126**, 4929 (2022).

[159] H. Wang, C. Zhang, and F. Rana, *Ultrafast dynamics of defect-assisted electron-hole recombination in monolayer MoS2*, Nano Letters **15**, 339 (2015).

[160] S. Jo, N. Ubrig, H. Berger, A. B. Kuzmenko, and A. F. Morpurgo, *Mono- and Bilayer WS_2 Light-Emitting Transistors*, Nano Letters **14**, 2019 (2014), PMID: 24669957.

[161] S. Eizagirre Barker, S. Wang, R. H. Godiksen, G. W. Castellanos, M. Berghuis, T. Raziman, A. G. Curto, and J. Gómez Rivas, *Preserving the emission lifetime and efficiency of a monolayer semiconductor upon transfer*, Advanced Optical Materials **7**, 1900351 (2019).

[162] G. Schweicher, G. D'Avino, M. T. Ruggiero, D. J. Harkin, K. Broch, D. Venkateshvaran, G. Liu, A. Richard, C. Ruzié, J. Armstrong, A. R. Kennedy, K. Shankland, K. Takimiya, Y. H. Geerts, J. A. Zeitler, S. Fratini, and H. Sirringhaus, *Chasing the "Killer" Phonon Mode for the Rational Design of Low-Disorder, High-Mobility Molecular Semiconductors*, Advanced Materials **31** (2019).

[163] H. M. Dong, Z. H. Tao, L. L. Li, F. Huang, W. Xu, and F. M. Peeters, *Substrate dependent terahertz response of monolayer WS2*, Applied Physics Letters **116** (2020).

[164] C. He, L. Zhu, Q. Zhao, Y. Huang, Z. Yao, W. Du, Y. He, S. Zhang, and X. Xu, *Competition between Free Carriers and Excitons Mediated by Defects Observed in Layered WSe2Crystal with Time-Resolved Terahertz Spectroscopy*, Advanced Optical Materials **1800290**, 2 (2018).

[165] D. Zhao, H. Hu, R. Haselsberger, R. A. Marcus, M. E. Michel-Beyerle, Y. M. Lam, J. X. Zhu, C. La-O-Vorakiat, M. C. Beard, and E. E. Chia, *Monitoring electron-phonon interactions in lead halide perovskites using time-resolved thz spectroscopy*, ACS Nano **13**, 8826 (2019).

[166] C. Zhang, C. Gong, Y. Nie, K.-A. Min, C. Liang, Y. J. Oh, H. Zhang, W. Wang, S. Hong, L. Colombo, R. M. Wallace, and K. Cho, *Systematic study of electronic structure and band alignment of monolayer transition metal dichalcogenides in Van der Waals heterostructures*, 2D Materials **4**, 015026 (2016).

[167] J. Yang, J. U. Lee, and H. Cheong, *Excitation energy dependence of Raman spectra of few-layer WS2*, FlatChem **3**, 64 (2017).

[168] G. Kresse and J. Hafner, *Ab initio molecular dynamics for liquid metals*, Phys. Rev. B **47**, 558 (1993).

[169] G. Kresse and J. Furthmüller, *Efficiency of ab-initio total energy calculations for metals and semiconductors using a plane-wave basis set*, Comp. Mat. Science **6**, 15 (1996).

[170] G. Kresse and J. Furthmüller, *Efficient iterative schemes for ab initio total-energy calculations using a plane-wave basis set*, Phys. Rev. B **54**, 11169 (1996).

[171] A. Togo and I. Tanaka, *First principles phonon calculations in materials science*, Scr. Mater. **108**, 1 (2015).

[172] Y. Zhao, X. Luo, H. Li, J. Zhang, P. T. Araujo, C. K. Gan, J. Wu, H. Zhang, S. Y. Quek, M. S. Dresselhaus, and Q. Xiong, *Interlayer Breathing and Shear Modes in Few-Trilayer MoS_2 and WSe_2*, Nano Letters **13**, 1007 (2013).

[173] J. Ribeiro-Soares, R. M. Almeida, E. B. Barros, P. T. Araujo, M. S. Dresselhaus, L. G. Cançado, and A. Jorio, *Group theory analysis of phonons in two-dimensional transition metal dichalcogenides*, Phys. Rev. B. **90**, 115438 (2014).

[174] L. Liang, J. Zhang, B. G. Sumpter, Q.-H. Tan, P.-H. Tan, and V. Meunier, *Low-frequency shear and layer-breathing modes in Raman scattering of two-dimensional materials*, ACS nano **11**, 11777 (2017).

[175] T. M and D. J. Late, *Temperature dependent phonon shifts in single-layer WS2*, ACS Applied Materials and Interfaces **6**, 1158 (2014).

[176] M. Rini, R. Tobey, N. Dean, J. Itatani, Y. Tomioka, Y. Tokura, R. W. Schoenlein, and A. Cavalleri, *Control of the electronic phase of a manganite by mode-selective vibrational excitation*, Nature **449**, 72 (2007).

[177] A. Cazé, R. Pierrat, and R. Carminati, *Spatial coherence in complex photonic and plasmonic systems*, Physical Review Letters **110** (2013).

SAMENVATTING

Terahertz spectroscopie gemeten in het tijdsdomein (THz-TDS) is een snel evoluerende techniek die de afgelopen jaren veel aandacht heeft gekregen vanwege het grote potentieel voor materiaalkarakterisering en het bestuderen van de interactie tussen elektromagnetische straling en materie. THz-TDS is een niet-invasieve en contactloze methode die kan worden gebruikt om de eigenschappen van ladingsdragers in metalen en halfgeleiders te bepalen, zoals hun mobiliteit en levensduur. Bovendien kan THz-TDS worden gebruikt om de tijdsafhankelijke respons van resonante structuren, zoals metallische resonatoren, te bestuderen wanneer ze een interactie met THz straling aangaan. Deze methode werkt door THz pulsen te genereren en de respons van het materiaal dat onderzocht wordt te registreren met behulp van technieken met femtoseconde tijdsresolutie. Het opgenomen signaal wordt vervolgens geanalyseerd om de spectrale en tijdsafhankelijke respons van het materiaal te bepalen, wat inzicht geeft in de dynamische eigenschappen van het materiaal en de interactie tussen THz straling en materie.

Ondanks de vele voordelen van THz spectroscopie wordt de praktische toepassing ervan beperkt door de inherente beperkte resolutie, die wordt opgelegd door de diffractielimiet. Deze limiet heeft het tot nu toe niet toegelaten om onderzoek te doen naar kleine structuren en eigenschappen op de nanoschaal. Om deze beperking aan te pakken, zijn er tijdens dit onderzoek twee THz nabije veld microscopen ontwikkeld, waarvan de ruimtelijke resolutie wordt bepaald door de afmetingen van de fotogeleidende antennes. De eerste microscoop maakt gebruik van micro-gestructureerde fotogeleidende antennes als lokale bron en detector, waardoor de lokale excitatie en detectie in het tijdsdomein mogelijk is. De tweede microscoop combineert een optische excitatie met een micro-gestructureerde antenne voor lokale detectie om de dragerdynamica te bepalen. Door nabije veld technieken te gebruiken, kunnen deze microscopen lengteschalen kleiner dan de diffractielimiet onderzoeken, waardoor resonante structuren en dunne films met een resolutie van slechts enkele micrometers kunnen worden onderzocht.

Het eerste hoofdstuk schetst de belangrijkste ideeën voor mijn onderzoek. Hoofdstuk 2 presenteert de experimentele opstellingen en methoden die in het onderzoek worden gebruikt, inclusief de cruciale nieuwe opstellingen. Hoofdstuk 3 onderzoekt de impact van veranderingen in de fotonische omgeving op de lokale dichtheid van optische toes-

tanden nabij een vlak interface en rondom een gouden resonator. Deze veranderingen worden in het tijdsdomein gemeten. Hoofdstuk 4 beschrijft hoe het elektrische veld dicht op het oppervlak van een rooster bestaande uit gouden resonatoren is geconcentreerd, vanwege het gebruik van door symmetrie beschermde gebonden toestanden in het continuüm, die alle stralingsverliezen volledig onderdrukken. Deze resonantie wordt in het tijdsdomein bestudeerd met behulp van de nabije veld excitatie en detectie microscoop. Hoofdstuk 5 meet de levensduur van de ladingdragers van een 2D halfgeleidend microkristal met een resolutie kleiner dan de diffractielimiet in het nabije veld en benadrukt het belang van nauwkeurige metingen op kleine lengteschalen. Het verschil tussen de levensduur van ladingsdragers in de bulk en aan het oppervlak, als gevolg van Auger recombinatie door middel van defecten, benadrukt de noodzaak van niet-invasieve technieken met een resolutie van micrometers. Ten slotte beschrijft hoofdstuk 6 de geïnduceerde hoogfrequente geleidbaarheid van een 2D halfgeleider op de microschaal en laat het effect zien van een roostertrilling op de frequentieafhankelijkheid van de geïnduceerde geleidbaarheid. Door de beperkingen die zijn opgelegd door de diffractielimiet te overwinnen, hebben deze THz nabije veld microscopen de mogelijkheden van THz spectroscopie uitgebreid en nieuwe en veelbelovende onderzoekspaden gecreëerd.

CONTRIBUTIONS OF COLLABORATORS

The work presented in this dissertation encompasses the original work of the author. However, research is a collaborative effort and seldom carried out individually. In this chapter, the contributions of collaborators to the work in this dissertation are clarified.

Chapter 2: The setups have been built in close collaboration with dr. Niels van Hoof.

Chapters 3 and 4: The samples were fabricated by Francesco Verdelli. The boundary-element method calculations using SCUFF have been performed by dr. Diego R. Abujetas and dr. Jose A. Sánchez-Gil.

Chapter 4: The transmittance spectra for the various degrees of detuning of the gold rod arrays were performed by dr. Niels van Hoof.

Chapters 5 and 6: The microcrystal was exfoliated by Sara A. Elrafei and dr. Rasmus H. Godiksen. The photoluminescence and atomic force microscopy measurements to determine the microcrystal layer thickness have been performed by dr. Rasmus H. Godiksen and Mohamed S. Abdelkhalik, respectively.

Chapter 6: The density function theory calculations of the interlayer phonons have been performed by dr. Adonai Rodrigues Da Cruz and prof.dr. Michael E. Flatté.

List of Publications

This thesis is based on the following publications:

1. *Direct Measurement of the Local Density of Optical States in the Time-Domain*, S. ter Huurne, D. Peeters, D. R. Abujetas, J. A. Sánchez-Gil, and J. Gómez Rivas **Manuscript submitted**.

2. *Direct Observation of Lateral Field Confinement in Symmetry-Protected THz Bound States in the Continuum*, S. ter Huurne, D. R. Abujetas, N. van Hoof, J. A. Sánchez-Gil, and J. Gómez Rivas **Advanced Optical Materials** 8, 2202403 (2023).

3. *Thickness Dependent Auger Scattering in a Single WS2 Microcrystal Probed with Time-Resolved Terahertz Near-Field Microscopy*, S. ter Huurne, N. van Hoof, and J. Gómez Rivas **Optics Letters** 48, 708-711 (2023).

4. *High-Frequency Sheet Conductance of Nanolayered WS2 Crystals for Two-Dimensional Nanodevices*, S. ter Huurne, A. Rodrigues Da Cruz, N. van Hoof, R. Godiksen, S. Elrafei, A. G. Curto, M. Flatté, and J. Gómez Rivas **ACS Applied Nano Materials** 5, 15557-15562 (2022).

Other publications by the author:

1. *Electric Tuning and Switching of the Resonant Response of Nanoparticle Arrays with Liquid Crystals*, E. van Heijst, S. ter Huurne, J. Sol, G. Castellanos, M. Ramezani, S. Murai, M. Debije, and J. Gómez Rivas **Journal of Applied Physics** 131, 083101 (2022).

2. *Fröhlich Interaction Dominated by a Single Phonon Mode in CsPbBr3*, C. Iaru, A. Brodu, N. van Hoof, S. ter Huurne, J. Buhot, F. Montanerella, S. Buhbut, P. Christianen, D. Vanmaekelbergh, C. de Mello Donega, J. Gómez Rivas, P. Koenraad, and A. Silov **Nature Communications** 12, 5844 (2021).

3. *Unveiling the Symmetry Protection of Bound States in the Continuum with Terahertz Near-Field Imaging*, N. van Hoof, D. Abujetas, S. ter Huurne, F. Verdelli, G. Timmermans, J. Sánchez-Gil, and J. Gómez Rivas **ACS Photonics** 8, 3010-3016 (2021).

4. *Evolutionary Optimization of Light-Matter Coupling in Open Plasmonic Cavities*, P. Bai, S. ter Huurne, E. van Heijst, S. Murai, and J. Gómez Rivas **The Journal of Chemical Physics** 154, 134110 (2021)

5. *Spectral and Temporal Evidence of Robust Photonic Bound States in the Continuum on Terahertz Metasurfaces*, D. Abujetas, N. van Hoof, S. ter Huurne, J. Gómez Rivas, and J. Sánches-Gil **Optica** 6, 996-1001 (2019).

6. *Diffraction Enhanced Transparency in a Hybrid Gold-Graphene THz Metasurface*, N. van Hoof, S. ter Huurne, R. Vervuurt, A. Bol, A. Halpin, and J. Gómez Rivas **APL Photonics** 4, 036104 (2019).

7. *Time-Resolved Terahertz Time-Domain Near-Field Microscopy*, N. van Hoof, S. ter Huurne, J. Gómez Rivas, and A. Halpin **Optics Express** 26, 32118-32129 (2018).

Patents by the author:

1. *Method and System for Performing Terahertz Near-Field Measurements*, N. van Hoof, S. ter Huurne, A. Halpin, J. Gómez Rivas, A. Bhattacharya, and G. Georgiou **US Patent App** 17/255,664 (2021)

CONFERENCE CONTRIBUTIONS

Keynote presentations:

1. *Bound States in the Continuum Excited and Detected in the Near Field*, IRMMW-THz 2021, Chengdu, China (September 2021, online)
2. *Time-Resolved THz Time-Domain Near-Field Microscopy On Exfoliated Single Flake of WS2*, IRMMW-THz 2020, Buffalo, USA (November 2020, online)
3. *THz Resonances with Infinite Lifetime in Array of Gold Resonators*, IRMMW-THz 2019, Paris, France (September 2019)

Oral presentations:

1. *Electromagnetic Field Confinement by Bound States in the Continuum*, IRMMW-THz 2022, Delft, Netherlands (September 2022)
2. *Electromagnetic Field Confinement by Bound States in the Continuum*, 12th THz Young Scientist Meeting, Delft, Netherlands (September 2022)
3. *Bound States in the Continuum at THz Frequencies*, CLEO /Europe-EQEC 2019, Munich, Germany (June 2019)
4. *Diffraction Enhanced Transparency in a Hybrid Gold-Graphene THz Metasurface*, IRMMW-THz 2018, Nagoya, Japan (September 2018)
5. *Diffraction Enhanced Transparency in a Hybrid Gold-Graphene THz Metasurface*, NFO15, Troyes, France (August 2018)

Poster presentations:

1. *Broadband Terahertz Near-Field Microscopy*, Physics@Veldhoven, Veldhoven, The Netherlands (January 2021)

2. *Time-Resolved Terahertz Near-Field Spectroscopy on Epitaxially Grown Semiconductor Layers*, Physics@Veldhoven, Veldhoven, The Netherlands (January 2020)

3. *Near-Field Excitation and Detection of THz Metasurfaces*, Physics@Veldhoven, Veldhoven, The Netherlands (January 2019)

ACKNOWLEDGEMENTS

These past years I have had the pleasure to meet and work with a lot of intelligent, enthusiastic, and supportive people. I would like to dedicate these pages to those who contributed to my PhD and were important during this time. Thanks to their contribution and support it was possible to write and finish my thesis.

First of all, I would like to thank my supervisor, prof. Jaime Gómez Rivas. Jaime, we have been working together since my master project and I'm grateful for all your support, feedback, encouragement, and mentorship during these years. Your expertise in the interpretation and explanation of data has been invaluable in guiding my research. You are an excellent group leader and stimulated strong collaboration in our group. I am grateful for having had the opportunity to work with you.

Thank you, dr. Dook van Mechelen for taking on the role as second promotor, and for the time you put in for carefully reading this thesis. I am also grateful to the other members of my committee, prof. Laurens Siebbeles, prof. Hartmut Roskos, prof. Miriam Vitiello, prof. Marion Matters-Kammerer, and dr. Klaas-Jan Tielrooij for being part of my defense and for providing invaluable feedback.

I would like to thank my paranymphs for having my back during the defense. I also would like to thank you both for pleasantly working together in the Surface Photonics group. Matthijs, you are always supportive, both personally and in the lab. You are very patient and kind when you are explaining everything to new people in the group, which I admire greatly. Maira, your enthusiasm, happiness, and the generation of random sounds in the lab are greatly appreciated. You can light up a room with your energy.

Being part of the Surface Photonics group has been a great experience and I am grateful for the strong sense of collaboration in the group. There are many people in the group I would like to thank for their support. Alexei, you taught the basics of working in an ultrafast optical lab to everyone in the group, which was very helpful. Mohammad, your knowledge and the clear explanation of particle arrays and strong coupling have helped me. This gave me a strong foundation to extend on. Niels, you taught me terahertz

time-domain spectroscopy and to work in an optical lab. During my master project and the first half of my PhD, we worked together a lot. I thoroughly enjoyed building and optimizing setups under the guidance of hard bass music and going to conferences together. Your enthusiasm and support have been very helpful and greatly contributed to the results presented in this thesis. Gabi, we spend a lot of time together working in the lab. I enjoyed showing you how to properly build a setup. Besides working we also had a lot of fun together. Francesco, it was great sharing an office with you, I enjoyed all our banter. Thank you for the samples that you fabricated, I appreciate the time and effort you put in. Saad, you have been a great colleague and I wish you all the best finishing your PhD. Erik, it was great to be your supervisor during your master, your knowledge of chemistry improved our lab significantly and your RCWA code is still used in the group. Djero, it was nice to teach you the THz setup in the last months of my PhD. Good luck with the rest of your PhD. I would also thank all other group members; Shaojun, Quynh, Ping, Aleks, Mingpeng, Shihab, Alaa, Masoumeh, Simr, and Jo for working together.

Thank you to the technicians Henny and Rainier, with your skill and support the lab was kept running well. Also thank you to the secretaries Simone and Sri who keep everything in order.

This work has been completed with the help of our collaborators, dr. José A. Sanchez-Gil, dr. Diego R. Abujetas, dr. Rasmus Godiksen, Sara Elrafei, dr. Alberto Curto, dr. Adonai Rodrigues Da Cruz, and prof. Michael Flatté thank you for the fruitful discussions, support, and joined publications.

I would like to thank my friends from university, de Stoute Gijtjes, for the great times we have had at the Borrel, on holidays, at beer festivals, at parties, and just hanging out. Marc, thank you for sharing the same passion for gaming and whiskey drinking. Nothing better than a great gaming and drinking session together. Maarten, thank you for sharing your passion for great food and drinks. I also appreciate how you always actively listen in conversations. Casper, thanks for your impeccable sense of humor and impressive intelligence. It was nice to be able to talk in-depth about my research with a friend. Shannen, thanks for giving me a cultural and creative perspective from time to time. Ruben, thank you for destroying everyone while playing pool during our shared holidays. Sander, thank you for sharing the same sense of humor only a few can appreciate. When we are together making jokes, it never disappoints. Kaylee, thank you for always organizing things to do together both with our friends as well as within PSN.

Bert, we have been friends for over a decade and I'm very happy we kept in contact all this time even though we went to different universities. You feel like family to me. I could always count on you and we shared a lot of great moments. We went on a couple of vacations together with Sanne and Marc, I especially enjoyed the cocktails and conversations in Croatia. We share a special taste in music as well and going to concerts together is always a blast.

I would like to thank my family, Jeroen, Jolanda, Bram, and Tom for always being there for me. You have had a huge impact on who I have become and am very grateful to you for supporting me in the choices I made. I'm looking forward to spending more time with you all in the future.

To my lovely wife, Sanne. You are the best partner I can imagine and I'm very happy that we have been together for more than eleven years. Being married to you is amazing. Your love and kindness have been fundamental during my PhD. You have supported me unconditionally and have made the work presented in this thesis possible. I enjoy being the father of our amazing daughter Amy. I look forward to welcoming our second child this year and spending the future together.

Thank you,
Stan

About the Author

Stan ter Huurne was born in Udenhout on January 12, 1995. He graduated high school in 2012 at the Theresialyceum in Tilburg. In 2015 he received his Bachelor Applied Physics from Eindhoven University of technology and continued to get a Master in Applied Physics in 2017. During his master's he completed a three month internship at the Technical University of Denmark. He finished his master in the Photonics and Semiconductor Nanophysics group with a one year project focused on terahertz spectroscopy. After finishing his master he started a PhD project in the same group of which the results are presented in this thesis. Besides working he likes to spend time with his family and he also enjoys cycling, reading, and listening to audiobooks.